# Possible Causes of Recent Changes in the Arctic Cloud Cover, Surface Temperature, and Temperature Inversions

**by**

**Yinghui Liu**

**A dissertation submitted in partial fulfillment of**

**the requirements for the degree of**

**Doctor of Philosophy**

**(Atmospheric and Oceanic Sciences)**

**at the**

**UNIVERSITY OF WISCONSIN-MADISON**

**2006**

# A dissertation entitled

## Possible Causes of Recent Changes in the Arctic Cloud Cover, Surface Temperature, and Temperature Inversions

submitted to the Graduate School of the
University of Wisconsin-Madison
in partial fulfillment of the requirements for the
degree of Doctor of Philosophy

**by**

**Yinghui Liu**

**Date of Final Oral Examination:** 11/28/2006

Month & Year Degree to be awarded: **December** 2006 **May** **August**

**********

**Approval Signatures of Dissertation Committee**

Steve Ackerman — Robert T. Marchant

Grant W. Petty — John A. Young

David J. Turner — [illegible]

Jeffrey R. Key

**Signature, Dean of Graduate School**

Martin Cadwallader/EH

Committee's Page. This page is not to be hand-written except for the signatures

**Abstract**

Arctic has experienced unprecedented climate change in the past two decades. Better understanding of these changes will contribute to better understanding of the global climate system due to the importance of Arctic climate system in the global climate system. Based on the combinations of conventional, satellite, and reanalysis data, this study quantifies the dramatic changes in the surface, atmosphere, and cloud cover in the Arctic in the past two decades, and investigates their connections to changes in the large-scale circulation. An explanation of cloud cover changes in the Arctic in four seasons is proposed and tested. The influence of trends in cloud cover on the surface temperature trends is quantified.

Arctic surface temperature, total cloud, heat and moisture convergence, and sea ice concentration are changing in ways that are a function of season and geographic regions. For surface temperature, a significant cooling trend over the Arctic Ocean in winter, and a significant warming trend in the Arctic in spring and summer from 1982 to 2000 are found. Surface temperature trends under clear-sky and cloudy conditions have similar patterns as the all-sky trends, and the magnitude of the trends under cloudy conditions is smaller than those under clear-sky conditions, which demonstrate the negative feedback of clouds on the surface temperature trends. Consistent with the surface temperature trend, trends in total cloud cover show a significant negative trend over the Arctic Ocean in winter, and generally a positive trend in the Arctic in spring and summer. These trends cannot be explained completely by changes in the Arctic Oscillation. Clear-sky temperature inversion strength during the cold season (November to March) in the Arctic

from 1980 to 1996 is estimated by a new 2-channel statistical algorithm based on satellite data. Both increasing and decreasing trends are found in the cold season for different regions. Strong coupling exists between changes in surface temperature and changes in inversion strength, but the trends in some areas appear to be a result of advection aloft rather than warming or cooling at the surface.

Changes in cloud cover influence surface temperature changes observed from satellites. The all-sky surface temperature trend can be partitioned into two parts: the first part is related to the combination of the surface temperature trends under clear-sky and cloudy conditions; the second part is caused by the cloud cover change and the surface temperature difference between cloudy and clear-sky conditions. The relative importance of these two parts differs seasonally, with the second part more important in winter, and the first part more important in spring, summer and autumn.

The mechanisms behind the total cloud cover changes vary with region and season. Moisture convergence in winter from 1982 to 1998 shows a significant negative trend over the northern Kara and Barents Seas to the pole (75-90 °N, 45-90 °E). Over this region, correlation coefficients between monthly anomalies in the cloud cover and the moisture convergence are relatively large and statistically significant. As moisture advection is the most important source of clouds over the Arctic Ocean in winter, the decreasing moisture convergence results in less cloud formation, possibly as a result of weakening cyclonic activity. Less cloud over this region leads to less cloud cover over the central Arctic Ocean in that less cloud is advected westward in the cyclone track. In spring and summer, increasing cloud cover is related to increasing moisture convergence

due to increasing cyclonic activity. Increasing surface evaporation due to decreasing sea ice concentration in spring, summer, and autumn may also contribute to increasing cloud cover.

**Acknowledgements**

First and foremost I wish to sincerely thank my research advisor, Dr. Jeffrey R. Key, for giving me the chance to pursue my PhD, and for his guidance, inspiration, patience, and trust throughout every stage of the process. Whenever I meet problems in research and feel frustrated, my advisor always gives me helpful discussion, suggestions and confidence. It would not be possible for me to realize my dream, being a PhD, without my advisor' effort. I feel very fortunate having the chance to work with my advisor in the past 6 years, and I am looking forward to having the regular weekly meeting with my advisor in the future.

My sincere thanks also go to my academic advisor, Dr. Steven A. Ackerman, for his guidance, and encouragement. I thoroughly enjoyed taking my advisor's classes, having discussions on scientific questions, and working together.

I would like to thank Dr. Paul Menzel sincerely for all his help on my research, and consistent warm encouragement.

I would like to thank my great friends, Dr. Xuanji Wang, and Ms. Yafang Zhong, for their helps on my research and emotional support throughout the whole process.

I would like to thank my PhD committee members, Dr. Jeffrey R. Key, Dr. Steven A. Ackerman, Dr. Robert R. Mathieu, Dr. John Young, Dr. Grant Petty, Dr. Ralf Bennartz, and Dr. Dan Vimont, for providing valuable comments and insight on my dissertation. I also need to thank Dr. Eric DeWeaver, Dr. Steve Vavrus, Dr. Jun Li, Dr. Allen Huang, Dr. Andrew Heidinger, Dr. Bryan Baum, Mr. Richard Frey, Mr. Dave Santek, Mr. Mike

Pavolonis, Dr. Dave Turner, Mr. Matthew Lazzara, and Ms. Kathy Strabala for their helpful discussion and comments on my research.

I would like to thank the Department of Atmospheric and Oceanic Sciences (AOS), and the Cooperative Institute for Meteorological Satellite Studies (CIMSS) at the University of Wisconsin-Madison for providing me an excellent research environment. Many thanks go out to all the professors in AOS, and research scientists in CIMSS for teaching me courses and knowledge, and for their helps on my research. I need to thank all the staffs in AOS and CIMSS for their excellent service for graduate students.

I would like to thank all my friends for helping in all kinds of ways, and those are Dr. Zhengyu Liu, Ms. Wenhua Wu, Ms. Zhang Hong, Dr. Jun Huang, Dr. Ke Liu, Ms. Lihua Wang, Mr. Zhenglong Li, Mr. Chianyi Liu, Mr. Longtao Wu, Mr. Wei Zhou, Mr. Wei Huang, Ms. Li Bi, Mr. Feng Lu, Mr. Feng He, Mr. Yun Liu, Mr. Wei Liu, Dr. Haijun Yang, Dr. Zhongdong Yang, Dr. Peng Zhang, Dr. Jinlong Li, Dr. Xin Jin, Dr. Xiaodong Liu, Dr. Shaima Nasiri, Dr. Robert Holz, Ms. Leslie Moy, Mr. Benjamin Johnson, Dr. Christine Chiu, Ms. Monica Harkey, Mr. Howard Berger, Ms. Agnes Huei Ni Lim, Mr. Richard Dworak, Mr. Brent Maddux, Mr. Timothy Wagner, Mr. Jay Hoffman, Mr. Mark Kulie, Mr. Jason Brunner, Mr. Kristopher Bedka, and Mr. Amato Evan.

And finally, none of this would have been possible without the love, support of my parents, whom this thesis is dedicated to.

This study is supported by NSF grants OPP-0240827, 0230317,0105461, and 0240791, NASA grant NAS5-31367, and NOAA SEARCH program.

**Contents**

Abstract ..... i

Acknowledgements ..... iv

List of Figures ..... ix

List of Tables ..... xv

1 Introduction ..... 1

2 Data and Methodology ..... 6

2.1 Data ..... 6

2.1.1 Conventional Observations ..... 6

2.1.2 Satellite Products ..... 7

2.1.3 Reanalysis Product ..... 10

2.1.4 Combination of Satellite Retrieval an Reanalysis Product: Moisture and Heat Convergence ..... 11

2.1.5 Pre-processing of the Data before Analysis ..... 12

2.2 Methodology ..... 13

2.2.1 Trend Analysis ..... 13

2.2.2 Retrieval Algorithm of Clear-sky Inversion Strength and Depth ..... 14

2.2.2.1 Theoretical Basis ..... 17

2.2.2.2 Retrieval Method Using HIRS Data ..... 21

2.2.2.3 Validation ..... 26

3 Arctic Climate Characteristics: Mean State and Trends ..... 39

3.1 Mean State and Trends in the Arctic 1982-2000 ..... 39

3.1.1 Surface Temperature ..... 39
3.1.2 Cloud Cover ..... 41
3.1.3 Sea Ice Concentration ..... 42
3.1.4 Moisture and Heat Convergence ..... 44
3.1.5 Clear-sky Temperature Inversion Strength ..... 45
3.2 Connections to the Arctic Oscillation ..... 47
3.3 Possible Causes of the Clear-sky Inversion Strength Trends ..... 50
4 The Influences of Changes in Cloud Cover on Recent Surface Temperature Trends in the Arctic ..... 72
4.1 Data ..... 74
4.2 Surface Temperature Trends ..... 75
4.2.1 All-sky Surface Temperature Trends ..... 75
4.2.2 Clear-sky and Cloudy-sky Surface Temperature Trends ..... 77
4.3 The Influence of Clouds on All-sky Temperature Trends ..... 78
4.3.1 Partition of All-sky Surface Temperature Trends ..... 78
4.3.2 Two Components of the Total Trends ..... 81
4.3.3 Retrieval Bias on the Total Trends ..... 82
4.4 Discussion and Conclusion ..... 82
5 Possible Causes of Seasonal Cloud Cover Changes in the Arctic, 1982-2000 ..... 90
5.1 Possible Causes of Seasonal Cloud Cover Changes in the Arctic in winter, 1982-2000 ..... 90
5.1.1 Data ..... 91

5.1.2 Trends in Cloud Cover and Moisture Convergence in winter ..... 92

5.1.3 Possible cause of decreasing cloud cover over NBK region ..... 93

5.1.4 Possible cause of decreased cloud cover over the central Arctic Ocean ..... 95

5.1.5 Discussion ..... 97

5.2 Possible Causes of Seasonal Cloud Cover Changes in the Arctic in spring, summer, and autumn, 1982-2000 ..... 99

5.3 Summary ..... 100

6 Conclusions and Future Plans ..... 110

6.1 Summary and Conclusions ..... 110

6.2 Remaining Issues and Future Plans ..... 115

7 References ..... 117

**List of Figures**

Fig. 2.1. Locations of the weather stations used in this study. Stations shown as squares were used for validation.

Fig 2.2. Temperature profile measured at Verhojansk , Russia, 1200 UTC on 3 December 2001. Temperature inversion top and base are indicated.

Fig. 2.3. Weighting functions for the MODIS bands at 6.7 μm, 7.2 μm, 11 μm, 13.3 μm, and 13.6 μm using subarctic winter standard atmosphere profile.

Fig. 2.4. Relationship between simulated brightness temperature difference pairs and the temperature inversion strength over high elevation surfaces (left) and low elevation surfaces (right).

Fig. 2.5. Weighting function for the 6.7 μm, 7.3 μm, 11 μm, 13.3 μm, and 13.6 μm channels based on a subarctic winter standard atmosphere profile.

Fig. 2.6. Relationships between inversion strength from radiosonde data and BT7.3-BT11 for (a) all seasons and (b) for the cold season. Cases with inversion strength less than 0 K are not considered to be inversions.

Fig. 2.7. Average specific humidity (SH) profiles in the (a) cold season, and (b) warm season.

Fig. 2.8. Comparison of monthly mean inversion strength (INVST) from meteorological stations and from HIRS data in cold season months during 1980-1996 at 11 stations. The asterisks represent the results from the 2-channel statistical method; diamonds represent the results from the TOVS retrieved temperature profiles.

Fig. 2.9. Same as Figure 2.8 but for trends.

Fig.3.1. Surface skin temperature mean (unit: K, left) and trend (unit: K/decade, right) in four seasons from 1982 to 2000 from APP-x. A trend with a confidence level larger than 95% based on the F test is indicated with +.

Fig. 3.2. 2-m air temperature trend (unit: K/decade, right) in four seasons from 1982 to 2000 based on ERA40. A trend with a confidence level larger than 95% based on the F test is indicated with +.

Fig. 3.3. Cloud cover mean (left) and trend (right) in four seasons from 1982 to 2000 from APP-x. A trend with a confidence level larger than 95% based on the F test is indicated with +.

Fig. 3.4. Cloud cover trend in four seasons from 1982 to 2000 based on ERA40 reanalysis. A trend with a confidence level larger than 95% based on the F test is indicated with +.

Fig. 3.5. Sea ice concentration mean (left) and trend (right) in four seasons from 1982 to 2000 based on microwave data. A trend with a confidence level larger than 95% based on the F test is indicated with +.

Fig. 3.6. Moisture convergence mean (unit: cm/month, left) and trend (right) in four seasons from 1982 to 2000 from TOVS Path-P. A trend with a confidence level larger than 95% based on the F test is indicated with +.

Fig. 3.7. Heat convergence trend (unit: $W/m^2$/decade) in four seasons from 1982 to 2000 from TOVS Path-P. A trend with a confidence level larger than 95% based on the F test is indicated with +.

Fig. 3.8a. Monthly mean clear-sky inversion strength (K) (top), and monthly trend of clear-sky inversion strength (K/year) (bottom) in November, December, January, February, March, and winter (DJF), 1980-1996, using the 2-channel statistical method. A trend with a confidence level larger than 90% based on the F test is indicated with +.

Fig. 3.8b. Same as Fig. 3.8a, but for TOVS profile inversions. The regions with high surface elevation are not indicated as white in this figure.

Fig. 3.9. The AO related trend (column 1), total trend (column 2), and residual trend (column 3) of surface skin temperature in four seasons from 1982 to 2000.

Fig. 3.10. The AO related trend (column 1), total trend (column 2), and residual trend (column 3) of 2-m air temperature in four seasons from 1982 to 2000 from ERA40.

Fig. 3.11. The AO related trend (column 1), total trend (column 2), and residual trend (column 3) of cloud cover in four season from 1982 to 2000 from APP-x.

Fig. 3.12. The AO related trend (column 1), total trend (column 2), and residual trend (column 3) of total cloud cover in four seasons from 1982 to 2000 from ERA40.

Fig. 3.13. The AO related trend (column 1), total trend (column 2), and residual trend (column 3) of sea ice concentration in four seasons from 1982 to 2000 from microwave data.

Fig. 3.14. The AO related trend (column 1), total trend (column 2), and residual trend (column 3) of moisture convergence in four seasons from 1982 to 2000 from TOVS Path-P.

Fig. 3.15. The AO related trend (column 1), total trend (column 2), and residual trend (column 3) of heat convergence in four seasons from 1982 to 2000 from TOVS Path-P.

Fig. 3.16. Monthly trend of surface skin temperature (K/year) in November, December, January, February, March, and winter (DJF), 1980 to 1996, from the TOVS-derived surface temperature. A trend with a confidence level larger than 90% based on the F test is indicated with +.

Fig. 3.17. Correlation coefficient between the monthly mean surface skin temperature anomalies and the monthly mean 2-channel statistical inversion strength anomalies over the period 1980-1996. A correlation coefficient with a confidence level larger than 95% based on the F test is indicated with +.

Fig. 3.18. Correlation between the monthly AO index anomalies and the monthly mean surface skin temperature anomalies (left), and monthly mean 2-channel statistical inversion strength anomalies (right), 1980- 1996. A correlation coefficient with a confidence level larger than 95% based on the F test is indicated with +.

Fig. 4.1: Seasonal all-sky (Fig 4.1a, top left), clear-sky (Fig 4.1b, top right), cloudy-sky (Fig 4.1c, bottom left) surface temperature trends, and cloud cover trends (Fig 4.1d, bottom right) from 1982 to 2004 based on APP-x dataset. A trend with a confidence level larger than 95% based on the F test is indicated with +.

Fig. 4.2: The comparison between the seasonal trends from the APP-x data set and ERA-40 data set, 1982-2001.

Fig. 4.3: Time series of regional means, seasonal APP-x surface skin temperature anomalies (solid line), and ERA-40 surface air temperature anomalies (dotted line) in winter and spring over selected regions.

Fig. 4.4: The difference between the seasonal mean surface temperature under cloudy and cloud-free conditions based on the APP-x dataset.

Fig. 4.5: The trend A (4a, left) and trend B (4b, right) components of the total all-sky surface temperature trend from 1982 to 2004 based on the APP-x dataset.

Fig 5.1. Decadal trends in (a) cloud clover from the APP-x (%/decade), (b) cloud cover from ERA40, (c) moisture convergence (cm/month) from TOVS Path-P, (d) sea level pressure (hPa) and wind (m/s) from ERA40, in the wintertime in the Arctic from 1982 to 2000. A trend with a confidence level larger than 95% based on the F-test is indicated with +.

Fig. 5.2. Correlation (%) between the APP-x cloud cover monthly anomalies and the TOVS moisture convergence monthly anomalies in the cold season from 1982 to1998. A trend with confidence level larger than 95% based on student-t test is assigned with +.

Figure 5.3. Time series of APP-x cloud cover anomalies (range: [0,1]) and TOVS Path-P moisture convergence anomalies (cm/month) in the cold season from 1982 to 1998 averaged over the NBK region (75-90N; 45-90E).

Fig. 5.4. Correlation between APP-x cloud cover monthly anomalies in each grid cell and those averaged over (75-90; 45-90) in the cold season from 1982 to 2000.

Fig. 5.5. Correlation coefficient between the APP-x cloud cover monthly anomalies and the TOVS Path-P moisture convergence monthly anomalies in winter, spring, summer, and autumn from 1982 t o1998. A trend with confidence level larger than 95% based on student-t test is assigned with +.

Fig. 5.6. Time series of Cyclone Activities Index anomalies in the Arctic in winter, spring, summer and autumn from 1950 to 2000.

Fig. 5.7. Correlation coefficient between the APP-x cloud cover monthly anomalies and the ERA40 surface evaporation monthly anomalies in cold season from 1982 t o1998. A trend with confidence level larger than 95% based on student-t test is assigned with +.

**List of Tables**

Table 2.1. Parameters used in this study.

Table 5.1. Correlation coefficients (CCs) of cloud cover anomalies among 5 regions over Arctic Ocean in winter in 1995. CCs with confidence level higher than 95% are underlined.

# 1 Introduction

Global climate has experienced dramatic changes in the past decades. The global average surface temperature has increased by 0.6±0.20 °C since the late 19th century. The 1990s was very likely the warmest decade in the instrumental records since 1861 (Houghton et al. 2001). Since 1979, observations from both satellite and balloon have shown a warming in the global middle-to-lower troposphere, and a cooling in the stratosphere. Over many regions of the Northern Hemisphere, the total atmospheric water vapor content has increased at a rate of several percents per decade. Since the beginning of the observational record, the water vapor in the lower stratosphere has increased about 10% per decade. The observed global average sea level based on tide gauge data rose by 1.0 to 2.0 mm/year during the 20th century.

Atmospheric circulation has been varying in the past decades, well expressed by the changes in the North Atlantic Oscillation (NAO) and the Arctic Oscillation (AO) (Thompson and Wallace 1998, 2000; Thompson et al. 2000). The NAO, which describes a positive relationship between the strength of the Icelandic Low and the Azores High, has been in a generally positive phase since about 1970. The positive (negative) mode of NAO is associated with northerly (southerly) wind over Greenland and eastern Canada, with negative (positive) temperature anomalies. In addition, west to southwesterly (northwesterly) winds tend to advect warm, moist (cool and dry) air into northern Europe and Scandinavia. The AO, which depicts a strong center of mean sea level pressure anomaly over the central Arctic Ocean and weaker centers of opposing sign over the

Atlantic and Pacific basins, has been generally positive since the early 1970s. The NAO can be considered as a major part of the AO and correlation between these two is very significant. Many variations in the atmospheric parameters (e.g. temperature, sea level pressure) can be partly explained by variations of the atmospheric circulation.

General circulation models (GCM) predict that the effects of anthropogenic greenhouse warming will be amplified in the northern high latitudes due to feedback associated with the high albedo of snow and ice (Manabe et al. 1992). In recent decades, the largest temperature increases have occurred over 40 to 70 °N. By using the data set from Jones (1994), Serreze et al. (2000) shows that the temperature over the period 1966-1995 has increased markedly over the Eurasian and northwest North American land masses, and increases have been smaller or negative over the ocean basins. Satellite records show that annual snow cover in the Northern Hemisphere has decreased by 10% (Groisman et al. 1994), and the extent of sea ice has decreased by 2.9+/-0.4 % per decade through 1996 (Cavalieri et al. 1997). By examining changes in sea level pressure over the Arctic Ocean during 1979-1994, Walsh et al. (1996) found reduction in sea level pressure over the period 1987-1994 compared with the previous eight-year period.

Arctic climate changes can affect the global climate in various ways. A warming surface melts the sea ice and reduces the surface reflectivity, which in turn causes more solar energy absorption at the surface and more warming. This regional warming accelerates warming at the global scale. The second feedback through which Arctic processes can amplify changes in global climate is through alterations in ocean circulation patterns. The possible slowing thermohaline circulation due to the warming

Arctic would have higher concentration of carbon dioxide in the atmosphere, leading to warmer atmosphere. The possible slowing thermohaline circulation would also cause regional cooling through less northward transport of heat by Atlantic Ocean currents. The potential thawing of the permafrost in the Arctic could release tremendous stores of carbon into the atmosphere and in turn cause more intense global warming. Because of the importance of the Arctic climate to the global climate, better understanding of the Arctic climate system leads to better understanding of the global climate system.

Better knowledge of the Arctic climate system needs long-term consistent observations, and improved understanding of all the feedbacks in the Arctic climate system. Observational datasets that span significant temporal and spatial scales are needed to support climate and environmental change investigations. Unfortunately, in-situ observational data in the Arctic are sparse due to the paucity of station data in the Arctic and the presence of a dynamic sea ice cover. The climate system is particularly challenging since it is known that components in the system are inherently chaotic. The non-linear processes include the basic dynamic response of the climate system and the interactions between the different components. The important feedbacks in the Arctic include snow/ice albedo feedback, water vapor feedback, and cloud-radiation feedback. The most important factor in understanding the Arctic climate system is the ability to understand and model cloud and radiation processes and their interrelationship with atmospheric dynamics and the underlying boundary. Polar cloudiness and microphysics are important, but are poorly simulated parameters in climate models (Randall et al. 1998; Vavrus 2004).

Satellites provide an appealing opportunity to monitor Arctic changes and study the complicated feedbacks. Polar-orbiting platforms view the high latitudes frequently with high spatial resolutions, producing high quality retrieval products. These retrieval products have been used to study recent trends in the Arctic surface temperature, sea ice cover, snow cover, cloud, and radiation fields at the surface and at the top of the atmosphere in the past 20 years.

Low-level atmospheric temperature inversions are a dominant feature of the atmospheric temperature field in the Arctic. Temperature inversions influence the magnitude of heat and moisture fluxes through openings in the sea ice, the depth of vertical mixing in the boundary layer, aerosol transport, surface wind velocity, and sea ice movement. Previous knowledge of temperature inversions is all derived directly from the sparse radiosonde data in the Arctic, however no temperature inversion information has been derived from the satellite data. Can satellite data be used to study the temperature inversion of the Arctic and its climatology?

Wang and Key (2003, 2005b) investigated the spatial and temporal characteristics and recent trends of Arctic surface, cloud, and radiation properties from 1982 to 1999 based on the extended AVHRR Polar Pathfinder (APP-x) product. For the all-sky surface temperature, they found a cooling trend in winter over the central and eastern Arctic Ocean, and mainly warming trends in spring, summer and autumn. GCM simulations predict that the increase of surface air temperature in response to a gradual increase of atmospheric carbon dioxide is at a maximum over the Arctic Ocean and its surroundings in the late fall and winter, and at a minimum in summer (Manabe et al. 1992). There is

discrepancy between the observations and model predictions. Wang and Key (2003, 2005b) also found increasing cloud fraction in spring and summer, and attributed these trends to increasing cyclonic activities; they found significant decreasing cloud fraction over the central Arctic region in autumn, and over most of the Arctic in winter. During the same time period, the Arctic cyclone activities in winter have been increasing in terms of cyclone frequency and intensity (Serreze et al. 1997; Key and Chan 1999; McCabe et al. 2001; Zhang et al. 2004). This raises the question of why there is decreasing winter cloud cover over the Arctic Ocean while stronger cyclones transport more moisture into the Arctic to form clouds.

This study attempts to monitor Arctic changes and study feedbacks by utilizing satellite data with high spatial and temporal resolutions over the whole Arctic. For the purpose of monitoring Arctic changes, clear-sky temperature inversion strength and inversion depth in the Arctic are retrieved by a newly developed 2-channel statistical algorithm based the satellite data, and the new algorithm is applied to derive a 17-year time series, 1980-1996, of the clear-sky temperature inversion strength during the cold season (November to March). For the purpose of studying the feedbacks, the relationship between the changes in inversion strength and surface temperature is investigated; a hypothesis to explain the decreasing cloud cover over the Arctic Ocean in winter is proposed and tested; and the influence of changes in cloud cover on recent surface temperature trends in the Arctic is examined.

# 2 Data and Methodology

## 2.1 Data

The Arctic has historically been one of earth's most scientifically under-investigated regions, but recently the importance of cloud-radiative interactions to global climate has been highlighted and research activities in this region have been increased. However, because of the inaccessibility of the Arctic Ocean and harsh conditions in the Arctic, conventional meteorological observations are sparse in the Arctic, and do not cover the Arctic Ocean well. Little observational data exist on Arctic clouds, especially during the dark winter season. Due to the high spatial and temporal coverage of the high latitude regions, satellites provide an appealing opportunity to measure surface and cloud characteristics in the Arctic. Atmospheric reanalysis assimilates observational data from diverse sources into a numerical model to provide multi-field products.

### 2.1.1 Conventional Observations

The radiosonde data in this study is from Historical Arctic Radiosonde Archive (HARA) (Kahl et al. 1992b), which comprises over 1.5 million vertical soundings of temperature, pressure, humidity and wind, representing all available radiosonde ascents from Arctic land stations north of 65°N from the beginning of the record through 1996. Radiosonde data from the series of former Soviet Union drifting ice stations during the period 1954-1990 are also included. All the soundings are processed with quality controls

using the method described by Serreze et al. (1992), after the radiosonde data is adjusted according to method developed by Mahesh et al. (1997). Twice-daily sounding data from 1980 to 1996 from 61 land stations (Figure 2.1) and the drifting ice stations are used.

### 2.1.2 Satellite Products

The Advanced Very High Resolution Radiometer (AVHRR) is carried aboard the National Oceanic and Atmospheric Administration's (NOAA) Polar Orbiting Environmental Satellites (POES) series since 1978 and is a broad-band, 5-channael scanning radiometer, sensing in the visible, near-infrared, and thermal infrared portions of the electromagnetic spectrum. The original AVHRR data from the NOAA7, 9, 11 and 14 satellites were processed to create the AVHRR Polar Pathfinder (APP; Fowler et al. 2000, Meier et al. 1997) data set, which consists of twice-daily composites (approximately 04:00 and 14:00 local solar times for the Northern Hemisphere) for the following parameters: channel reflectance and brightness temperatures, clear-sky surface temperature and albedo, viewing and illumination angles, cloud and surface masks in the format of 5 km spatial resolution Equal Area Scalable Earth-Grid (EASE-Grid). The data set covers the whole Arctic (60 degree poleward).

The APP-x dataset extends the AVHRR Polar Pathfinder product to include cloud optical depth, cloud particle phase and size, cloud-top temperature and pressure, all-sky surface temperature and broadband albedo, and radiative fluxes daily at 04:00 and 14:00 local solar time. Parameters in the APP-x dataset are at horizontal resolution 25-km EASE-Grid, and are available from 1982 to 2004. Retrievals were done with the Cloud

and Surface Parameter Retrieval system (Key 2002; Key et al. 2001; Key and Intrieri 2000), which was specifically designed for polar AVHRR daytime and nighttime data. Cloud detection is done with a variety of spectral and temporal tests optimized for high-latitude conditions (Key and Barry, 1989). The clear-sky surface skin temperature is retrieved using a split-window technique (Key and Haefliger 1992; Key et al. 1997). A regression model was developed to estimate the cloudy-sky surface temperature from nearby clear-sky temperatures, wind speed, and solar zenith angle (day time) (Key and Wong, 1999). In terms of the annual cycle of the total cloud fraction, the APP-x dataset provides the best cloud fraction estimation among the other satellite retrievals regarding the comparisons with surface observations and literature study (Wang and Key 2005a). The APP-x parameters have been validated with data collected during the Surface Heat Balance of the Arctic Ocean (SHEBA) field experiment in the western Arctic (Key et al. 2001; Maslanik et al. 2001; Stroeve et al. 2001; Key and Intrieri 2000; Wang and Key 2003). The comparison between APP-x dataset and SHEBA ship measurements show a 0.2 K bias and a 1.98 K of root-mean-square (RMS) error in the surface skin temperature (Wang and Key 2005a). Surface temperature trends from APP-x were compared with those from 41 Arctic meteorological stations and were found to be in good agreement (Wang and Key 2003). Wang and Key (2003) investigated the consistency of the APP-x products from different NOAA polar orbiting satellites over the period, and they found no observable bias.

The Television and Infrared Observation Satellite (TIROS) Operational Vertical Sounder (TOVS) instrument has flown continuously on NOAA POES since 1979. Two

of the three TOVS radiometers were used to create the TOVS Polar Pathfinder (TOVS Path-P) data set: the high-resolution infrared radiation sounder (HIRS), with one visible and 19 infrared channels, and the microwave sounding unit (MSU), with four channels. To convert these radiances into geophysical variables, the Improved Initialization Inversion ("3I"; Chedin et al. 1985) method was used, and it was modified to improve its performance over snow and ice (Francis 1994).

The products contained in Path-P include standard TOVS retrievals such as air temperatures at 50,70, 100, 300, 400, 500, 600, 700, 850, 900 hPa, layer-average precipitable water in 5 layers 300-400, 400-500, 500-700, 700-850, 850-surface, surface skin temperature, effective cloud fraction, cloud-top pressure and temperature daily at a horizontal resolution of 100 km of the EASE-Grid. This product covers the whole Arctic (60 degree poleward) since 1979. The TOVS Path-P products have been validated extensively with data from Russian NP stations in the ice-covered Arctic Ocean and from the SHEBA field experiment (Schweiger et al. 2002).

HIRS brightness temperatures (BT) at 7.3 μm and 11 μm are used in this study to retrieve the clear-sky inversion strength. The HIRS data used in this study includes NOAA-6 (1979-1982), NOAA-7 (1983-1984), NOAA-9 (1985-1986), NOAA-10 (1987-9/16/1991), NOAA-11 (9/17/1991-1994) and NOAA-12 (1995-1996) data. The spatial resolution of the original HIRS brightness temperature data is 17 km at nadir. Cloud detection tests from the 3I algorithm (Francis (1994), Stubenrauch, 1999) are applied to distinguish clear from cloudy scenes.

The NASA Goddard Space Flight Center (GSFC) sea ice concentration data set (Cavalieri et al. 2005) derived from the Nimbus-7 Scanning Multichannel Microwave Radiometer (SMMR) and the Defense Meteorological Satellite Program's (DMSP) DMSP-F8, -F11 and -F13, Special Sensor Microwave/Imager (SSM/I) has been generated using the NASA Team algorithm. It is designed to provide a consistent time series of sea ice concentrations (the fraction of ocean area covered by sea ice) spanning the coverage of several passive microwave instruments. The data set currently includes daily and monthly averaged sea ice concentrations derived from Nimbus-7 SMMR and DMSP-F8, -F11 and -F13 SSM/I daily brightness temperatures at the SSM/I polar stereographic grid (25 x 25 km), and are converted to a horizontal resolution of 25 km of the EASE-Grid. The data set begins October 1978 and continues through December 2004.

### 2.1.3 Reanalysis Product

A reanalysis is created by the assimilation of observational data into a "frozen" numerical model. The initial guess for the reanalysis is the model's short-range forecast made from previous reanalysis. The output of a reanalysis product include consists of assimilation system's control variables such as wind, temperature, and pressure, and the model-computed fields of cloudiness, precipitation. The computed fields have more uncertainty than the control variables, since they are dependent on the physical parameterizations in the model.

Reanalysis product used in this study is the ERA40 reanalysis (Uppala et al. 2005) from European Centre for Medium-Range Weather Forecasts (ECMWF). Most of the ERA-40 archived output is available monthly, daily, and four times daily at a resolution of 2.5-degree latitude by 2.5-degree longitude from September 1957 to August 2002. The daily and monthly fields in ERA40 include parameters at surface (2-meter temperature, total cloud cover, surface evaporation, sea level pressure, etc.); wind, temperature, humidity etc. at 23 pressure levels from 1000 to 1 hPa.

### 2.1.4 Combination of Satellite Retrieval an Reanalysis Product: Moisture and Heat Convergence

By combining daily satellite precipitable water retrievals from the TOVS Path-P data set with wind and surface pressure fields from the NCEP-NCAR reanalysis, Groves and Francis (2002a, 2002b) created a data set of the Arctic atmospheric moisture budget at a horizontal resolution of 100 km EASE-Grid daily from 1979 to 1998. This data set compares well with rawinsonde-derived moisture transport and reanalysis products, and captures spatial and temporal variability that other data sets cannot owing to the sparse coverage of the conventional observation network in the Arctic Ocean. The daily 19-year data set provides vertically integrated precipitable water flux convergence (moisture convergence hereinafter) from surface to 300 hPa. The moisture convergence is expressed as $(-\nabla \cdot \mathbf{F})/\rho_w$, where $\mathbf{F}$ is the vertically integrated precipitable water mass flux.

Daily fields of sensible heat budget are also calculated from Path-P temperature and NCEP-NCAR reanalysis upper-level winds for 5 tropospheric layers between surface and 300 hPa. And this heat convergence data is available from 1979 to 2001.

### 2.1.5 Pre-processing of the Data before Analysis

Parameters in the APP-x data set are available daily at 04:00 and 14:00 LST from January 1982 to December 2004 at a horizontal resolution of 25-km. Monthly means of cloud cover, cloud phase, cloud optical depth, and surface temperature under cloud-free, cloudy, and all-sky conditions are calculated from the daily data. The monthly means are sub-sampled to 100 km resolution EASE-Grid by average. At least 10 daily values in a month are required in the calculation of the monthly means of the surface temperature under cloud-free and cloudy conditions. Due to the high cloud cover in the Arctic, the daily cloud-free and cloudy data are sub-sampled to a 100 km grid by average to meet this requirement. Seasonal means are calculated based on the monthly means in winter (December, January, and February), spring (March, April, and May), summer (June, July and August), and autumn (September, October, and November).

Parameters in and from the TOVS Path-P dataset are available daily at a horizontal resolution of 100-km. Monthly means of cloud cover, and surface temperature under cloud-free are calculated from the daily data. Seasonal means are calculated based on the monthly means. Monthly means and seasonal means of moisture and heat convergence are calculated in the same way. The moisture convergence is from January 1980 to December 1998, and the heat convergence is from January 1980 to December 2001.

Monthly means of sea ice concentration from January 1980 to December 2004 are derived from the sea ice dataset directly, and seasonal means are calculated based on the monthly means.

Parameters in the ERA40 reanalysis are from September 1957 to August 2002 at a resolution of 2.5-degree latitude by 2.5-degree longitude. Monthly means of 2-m air temperature, total cloud cover, sea level pressure, surface wind, and surface evaporation are derived from the dataset directly, and seasonal means are calculated base on the monthly means.

Monthly anomalies of each parameter are calculated as the difference between the monthly mean and the mean of monthly means in each individual month. Trend of the monthly anomalies of each month is extracted for the elimination of the trend effect in the monthly anomalies.

All the parameters used in this study are listed in Table 2.1.

## 2.2 Methodology

### 2.2.1 Trend Analysis

Monthly and seasonal trends of each parameter are derived based on the monthly and seasonal means. Trend analysis were performed using least square fit regression, where the trend value is the slope of the regression line. For each trend, an F-test value of significance is computed.

The linear Pearson correlation coefficient between two parameters is calculated based on the time series of monthly or seasonal anomalies of these two parameters. For each correlation coefficient, a student t-test confidence level is calculated.

### 2.2.2 Retrieval Algorithm of Clear-sky Inversion Strength and Depth

Low-level atmospheric temperature inversions are nearly ubiquitous at high latitudes during the polar winter, and are the dominant feature of the atmospheric temperature field in the Arctic (Curry et al. 1996). They may result from radiative cooling, warm air advection over a cooler surface layer, subsidence, cloud processes, surface melt, and topography (Vowinkel and Orvig 1970; Maykut and Church 1973; Busch et al. 1982; Curry 1983; Kahl 1990; Serreze et al. 1992). Temperature inversions influence the magnitude of heat and moisture fluxes through openings in the sea ice ("leads"), the depth of vertical mixing in the boundary layer, aerosol transport, photochemical destruction of boundary-layer ozone at Arctic sunrise, surface wind velocity, and lead formation (Andreas 1980; Andreas and Murphy 1986; Bridgman et al. 1989; Barrie et al. 1988; Barry and Miles, 1988). Knowledge of inversion characteristics is therefore needed for process studies and modeling, e.g., for simulating the movement of sea ice (Overland 1985; Hibler and Bryan 1987).

A number of recent studies have investigated the characteristics of polar temperature inversions based on radiosonde data. Kahl (1990, 1992a) examined the climatological characteristics of low-level tropospheric temperature inversions based on radiosonde data from two coastal weather stations. Serreze et al. (1992) investigated the seasonal and

regional variations in characteristics of the Arctic low-level temperature inversion using radiosonde data from Arctic inland and coastal sites and Soviet drifting stations. Bradley et al. (1992) examined the annual cycle of surface-based inversions at nine Arctic weather stations based on radiosonde data. Stone and Kahl (1991) examined Antarctic temperature inversions. All of these studies used radiosonde data to characterize the temporal distributions of inversions. However, temperature inversion information is spatially incomplete, being limited to point measurements at coastal and interior meteorological stations.

Amplified warming in the northern high latitudes is a pervasive feature of general circulation model simulations with enhanced greenhouse forcing. This amplified warming is partly due to the temperature-albedo feedback associated with the retreat of snow and sea ice (IPCC, 2001). In addition, the breakdown of the shallow but steep near-surface temperature inversions in the polar regions is another possible factor contributing to polar amplification (Chapman and Walsh, 1993). Studies of trends in temperature inversion characteristics are therefore needed to improve our understanding of polar amplification, and some work has been done in this area. The decreasing trend in midwinter surface-based inversion depths along a transect from Alaska to the Canadian high Arctic for the period 1966 to 1990 was investigated by Bradley and Keimig (1993), Walden et al. (1996), and Bradley et al. (1996). A long-term increasing trend of low-level temperature inversion strength was found over the Arctic Ocean from 1950 to 1990 based on radiosonde data from Russian drifting stations, and dropsonde data from U.S. Air Force "Ptarmigan" weather reconnaissance aircraft (Kahl and Martinez, 1996).

However, these studies were limited in their spatial extent and did not include the 1990s, a period in which rapid changes have been observed.

Satellite-borne sensors provide an opportunity to monitor the clear-sky temperature inversions in the polar regions. Liu and Key (2003, hereinafter referred to as LK03) developed an empirical algorithm to detect and estimate the characteristics of clear-sky, low-level temperature inversions using data from the Moderate Resolution Imaging Spectroradiometer (MODIS) on the Terra and Aqua satellites (King et al. 2003). However, MODIS does not yet provide a long enough record for climatological analyses. The TIROS-N Operational Vertical Sounder (TOVS) has observed the Earth's surface and atmosphere since 1979 with spectral channels similar to those used in the MODIS algorithm, and therefore provides an opportunity to study changes in temperature inversions over the last two decades. In this paper we adapt the empirical MODIS method to the High Resolution Infrared Radiation Sounder (HIRS), which is part of the TOVS instrument, for the period 1980-1996. Of primary interest are the spatial distribution and trends in inversion strength (INVST), defined as the temperature difference between the top of the inversion and the surface. Results are restricted to clear-sky conditions during the cold season (November through March) in the Arctic.

There are many different definitions of the inversion layer in the literature (Bilello, 1966; Maxwell, 1982; Kahl, 1990; Serreze et al., 1992; Bradley et al., 1992). In this study, for each sounding that contains an inversion, the inversion base is defined by the station elevation and the inversion top is the atmospheric level with the maximum temperature between the surface and the 700 hPa level. Isothermal layers at the base, top,

or embedded within an inversion layer are included as a part of an inversion, as are thin layers with a negative lapse rate, provided that they are not more than 100 m thick. With these criteria, both surface-based inversions (Bradley et al., 1992) and elevated inversions (Serreze et al. 1992) are included in this study, as long as the surface is colder than the maximum temperature below 700 hPa. The inversion strength is defined as the temperature difference between the inversion top and the surface; inversion depth is defined as the altitude difference between the inversion top and the surface. Figure 2.2 shows a typical temperature profile with a temperature inversion, and the inversion strength and depth are indicated. We note that inversion strength can also be defined as a ratio of the temperature and altitude differences across the inversion, but we use the simpler definition to be consistent with the studies cited above.

#### 2.2.2.1 Theoretical Basis

Theoretically, the clear-sky temperature inversion strength and depth can be retrieved from satellite data (Liu and Key 2003). The MODIS on the Terra and Aqua satellites is used as an example to demonstrate this statement.

Upwelling thermal radiation measured by satellite sensors is a function of the atmospheric transmittance at a given wavelength and the atmospheric temperature. The channel weighting function, which is the derivative of transmittance with respect to pressure, describes the degree to which radiation emitted at various vertical levels contributes to the upwelling radiance.

Figure 2.3 gives the relative weighting functions for MODIS channels 27 (6.7 μm), 28 (7.2 μm), 31 (11 μm), 33 (13.3 μm) and 34 (13.6 μm), calculated for the subarctic winter standard atmosphere. Channels 27 and 28 are water vapor channels; 31 is a window channel; 33 and 34 are carbon dioxide channels. The peaks of the weighting functions for the 6.7, 7.2, 11, 13.3, and 13.6 μm channels are approximately 600 hPa, 800 hPa, the surface, 950 hPa, and 900 hPa, respectively. Because the weighting functions are broad and represent an average radiance contribution from a layer, the measured brightness temperature is sensitive to a relatively thick layer. The weighting functions will be somewhat different for different absorber amounts and atmospheric pressure, the latter being a function of surface elevation.

As Figure 2.3 shows, the brightness temperature of the window channel at 11 μm, $BT_{11}$, will be most sensitive to the temperature of the surface. The 7.2 μm water vapor channel brightness temperature, $BT_{7.2}$, is most sensitive to temperatures near 800 hPa. The magnitude of the brightness temperature difference (BTD) between the 7.2 μm and 11 μm channels, $BT_{7.2}$-$BT_{11}$, will therefore be proportional to the strength of temperature difference between the 800 hPa layer and the surface, which is related to the inversion strength. This should also be true for the two 13 μm carbon dioxide channels. The 6.7 μm water vapor channel peaks near 600 hPa, so $BT_{6.7}$-$BT_{11}$ can also provide information about inversion strength. In the Arctic and the low elevation areas of the Antarctic, the temperature inversion top is typically below 700 hPa (Serreze et al., 1992; Bradley et al., 1992), so $BT_{7.2}$-$BT_{11}$ will better represent the inversion strength than will $BT_{6.7}$-$BT_{11}$. $BT_{7.2}$-$BT_{11}$ is also more effective than $BT_{13.3}$-$BT_{11}$ and $BT_{13.6}$-$BT_{11}$ in providing

information on inversion strength because the surface contribution is larger at 13.3 μm and 13.6 μm than at 7.2 μm. On the Antarctic plateau where the surface pressure is typically 600-700 hPa, water vapor amount is low, and inversions are strong and deep, both $BT_{7.2}$-$BT_{11}$ and $BT_{6.7}$-$BT_{11}$ can provide useful information on inversion strength. The brightness temperature difference is not only a function of the temperature inversion strength, but also the inversion depth.

To illuminate the relationship between BTDs and both inversion strength and inversion depth, the radiative transfer model *Streamer* (Key and Schweiger, 1998) is used to simulate MODIS brightness temperatures. The model can simulate the brightness temperature at each MODIS infrared channel for each radiosonde temperature and humidity profile. Simulations and subsequent analyses with observations are done separately for low and high elevation surfaces. On average, inversion properties are different for low- and high-altitude locations because of the climatological ranges in surface temperature, atmospheric water vapor, and, of course, surface pressure. Therefore, weighting functions and the relationship between inversion characteristics and BTDs also differ.

Figure 2.4 shows the simulated relationship between different BTD pairs and the temperature inversion strength for high and low surface elevation conditions. There are strong linear relationships for all channel pairs and both surface elevation categories. Simulated BTD pairs and the temperature inversion depth for high and low elevation surfaces also show linear relationship. For high elevation surfaces the relationships are weak, especially when the BTD is large. For low elevation surfaces the linear

relationships are stronger. For both elevation categories, larger BTDs indicate greater inversion depth.

Based on the simulated relationships, it appears that MODIS data can, in theory, be used to estimate inversion strength and inversion depth. Is this also true for HIRS data? Weighting functions for the 6.7 μm, 7.3 μm, 11 μm, 13.3 μm, and 13.6 μm channels of HIRS data based on a subarctic winter standard atmosphere profile are shown in Figure 2.5. The peaks of the weighting functions for the 7.3 and 11 μm channels are approximately 650 hPa, and the surface, respectively. The brightness temperature of the window channel at 11 μm, $BT_{11}$, is most sensitive to the temperature of the surface. The 7.3 μm water vapor channel brightness temperature, $BT_{7.3}$, has the greatest contribution from the layer around 650 hPa. The magnitude of the brightness temperature difference between the 7.3 μm and 11 μm channels, $BT_{7.3}$-$BT_{11}$, will therefore be related to the temperature difference of the inversion top and the surface, i.e., the inversion strength. $BT_{13.3}$-$BT_{11}$ and $BT_{13.6}$-$BT_{11}$ are also related to inversion strength, where weighting functions for the 13.3 μm and 13.6 μm carbon dioxide channels peak even lower than that of 7.3 μm channel. However, $BT_{7.3}$-$BT_{11}$ is more effective than $BT_{13.3}$-$BT_{11}$ and $BT_{13.6}$-$BT_{11}$ to retrieve inversion strength due to the larger surface contribution at 13.3 and 13.6 μm than that at 7.3 μm (Liu and Key, 2003).

Because inversion depth is more difficult to retrieve than inversion strength (LK03), especially with a relatively low spatial resolution sensor such as HIRS, only inversion strength is considered here.

#### 2.2.2.2 Retrieval Method Using HIRS Data

The inversion strength retrieval algorithm described by LK03 is based on collocated radiosonde and satellite data, and a similar approach is used in this study. Radiosonde data from 61 stations in the Arctic and HIRS brightness temperature data from 1980 though 1996 are used to construct the data set of matched clear-sky pairs of the HIRS pixels closest in time and space to radiosonde observations. HIRS spots must be within 75 km and one hour of the radiosonde observation to be used. The clear-sky determination is based on the cloud detection steps from the 3I algorithm. Figure 2.6 shows the relationship between inversion strength from radiosonde data and $BT_{7.3}$-$BT_{11}$ for the cases in all seasons and for the cold season, defined as November through March. When $BT_{7.3}$ - $BT_{11}$ is larger than –10 K in all seasons (Figure 2.6a), the inversion strength is linearly related to $BT_{7.3}$ - $BT_{11}$. When $BT_{7.3}$ - $BT_{11}$ is less than –10 K, there is no linear relationship. During the cold season (Figure 2.6b), most cases have $BT_{7.3}$ - $BT_{11}$ larger than –10 K, which exhibits a good linear relationship between inversion strength and $BT_{7.3}$ - $BT_{11}$.

The cases with $BT_{7.3}$ - $BT_{11}$ less than –10 K occur primarily in the warmer months, possibly because of the larger variability in water vapor amount and vertical distribution, and weaker inversion strength during that part of the year. Figure 2.7 shows the average specific humidity profiles in the cold and warm seasons. In the cold season, the water vapor content of the atmospheric column is low, so that the peak of the 7.3 μm weighting function is near the inversion top. During the warm season, the larger water vapor content raises the peak of the weighting function such that the channel is less sensitive to

changes in inversion strength. It is for these reasons that we focus here on the inversion strength during the colder months.

Inversion strength in the cold season can be estimated by a linear combination of $BT_{11}$, $BT_{7.3}$ - $BT_{11}$, and $(BT_{7.3} - BT_{11})^2$, with the coefficients determined by linear regression when $BT_{7.3} - BT_{11}$ is larger than –10 K. The equation used to retrieve inversion strength is:

$$\text{INVST} = a_0 + a_1 * BT_{11} + a_2 * (BT_{7.3} - BT_{11}) + a_3 * (BT_{7.3} - BT_{11})(\sec\theta - 1),$$

where the coefficients $a_0$, $a_1$, $a_2$, and $a_3$ are determined through multiple regression with INVST from radiosonde data, and $\theta$ is the sensor view angle. When $BT_{7.3}$-$BT_{11}$ is less than –30 K, the estimated inversion strength is defined to be 0 K. BTs from two channels are used to derive the inversion strength, so we refer to this as the "2-channel" method.

In the cold season there are a few cases with $BT_{7.3}$-$BT_{11}$ between –30 K and –10 K, where the inversion strength is 0 K for some situations and larger than 0 K for others. The estimated inversion strength is therefore defined to linearly increase from 0 K to 2 K when $BT_{7.3}$-$BT_{11}$ increases from –30 K to –10 K. The radiosonde data in all the matched cases are low-elevation meteorological stations, so the retrieval equation is most applicable to low-elevation areas.

In LK03, inversion strength regression equations for both high-elevation surfaces (higher than 2800 m) and low-elevation surfaces (lower than 500 m) were derived. In this

work, only equations for low-elevation surface were derived. If the MODIS equation for a low-elevation surface is used to derive inversion strength over a high-elevation surface, the retrieved inversion strength will have a lower-than-actual value when the retrieved value is less than 17 K, and a higher-than-actual value when the retrieved value is larger than 17 K. If the same relationship applies to the HIRS retrievals, then estimated inversion strength over Greenland (high elevation) will be lower than the actual inversion strength, because the monthly mean retrieved inversion strengths over Greenland are between 10 K and 17 K. The negative bias of the retrieved monthly mean inversion strength over Greenland is between –2.5 K and –1.0 K. The retrieval bias for areas with surface elevations between 500 m and 2800 m is also negative, but smaller than that over Greenland. For these reasons, inversion strength retrievals over high-elevation surfaces are not included in this analysis (white areas in Figure 2.10, 2.11, 2.12 and 2.13).

The 17-year HIRS record comes from six different satellites: NOAA-6, -7, -9, -10, -11, and -12. Inter-satellite biases result from orbital drift, sensor degradation, differences in spectral response functions, changes in calibration procedure, and deficiencies in the calibration procedure for each satellite. Orbital drift results in sampling at somewhat different times of the day at the beginning and end of a satellite's lifetime, which would have the most pronounced impact on retrievals where the diurnal cycle is significant. The diurnal cycle of inversion strength in the Arctic during the cold season is, however, small. More than 90% of the monthly mean inversion strengths from 26 Arctic stations during the cold season at 00 UTC are within 2.0 K of the monthly mean at 12 UTC.

Because the diurnal cycle of the inversion strength is small, we do not expect orbital drift to significantly affect the inversion strength trends.

TOVS inter-satellite calibration is essential for climate change studies. The level 1b data was calibrated using the standard procedure described in the NOAA Polar Orbiter Users Guides (Kidwell, 1998). In addition, empirical corrections were applied to the calibrated brightness temperatures in the TOVS Path-P product generation. These corrections (also known as DELTAs) were applied to NOAA-10, -11 and –12, and the deltas for NOAA-10 were applied to NOAA-6 through -9 (Schweiger et al. 2002; Chen et al. 2002). However, some inter-satellite differences remain after these calibration steps (Chen et al., 2002). To minimize inter-satellite calibration differences, here we determine separate sets of inversion strength regression coefficients for each satellite or pair of satellites from 1980 through 1996: one for NOAA-6 (1980-1982), one for NOAA-7 (1983-1984) and NOAA-9 (1985-1986), one for NOAA-10 (1987-9/16/1991), and one for NOAA-11 (9/17/1991-1994) and NOAA-12 (1995-1996). Four sets of regression coefficients are therefore derived. While there are over 18,000 potential radiosonde-satellite matched pairs for each year over the 61 stations, the actual numbers of matched pairs that can be used to derive each retrieval equation are 223, 597, 404, and 441 respectively, due to cloudiness and space and time distance constraints.

After obtaining the retrieval equation coefficients for each satellite or pair of satellites from 1980 through 1996, the initial HIRS clear-sky BTs are converted to inversion strength based on the inversion strength retrieval equations. The estimated inversion strength is then mapped to the 100 x 100 km Equal-Area Scalable Earth Grid

(EASE-Grid) based on the longitude and latitude of the original TOVS data. For each day, a composite map of clear-sky inversion strength over the region north of 60°N is created. The monthly mean inversion strength for each grid point is calculated as the mean of all the daily composite inversion strengths in a month, which include inversion strength values of zero. The seasonal mean inversion strength is derived as the mean of monthly means in that season. The monthly trend of inversion strength for each grid point is derived using linear least squares regression based on the monthly mean inversion strength for the 17-year period 1980-1996. The statistical significance level is determined with an F-test. It is important to note that the number of daily retrievals in each month is relatively evenly distributed across the first, second, and third 10-day periods from 1980 to 1996. This is important because trends in cloud amount could, in theory, result in non-uniform sampling of clear-sky pixels in different months and years, and artificially introduce trends in clear-sky inversion strength.

As with the radiosonde data, inversion strength can be calculated from satellite-derived temperature profiles. The operational TOVS Polar Pathfinder (Path-P) dataset provides the temperature profiles at 13 pressure levels, with five levels from 700 hPa to the surface: 700, 850, 900, 1000 hPa, and the surface. The inversion strength is derived as the difference between the maximum temperature of these five levels and the surface temperature. If the maximum temperature is at surface, the inversion strength is 0 K. We refer to this estimation of inversion strength as the "profile inversion strength". The derived inversion strength is mapped on the 100 km EASE-Grid for each day. The

monthly means, seasonal means, and trends are calculated in the same manner as for the 2-channel method.

#### 2.2.2.3 Validation

To evaluate the regression equations, cross validation is performed. For each of 100 iterations, 70% of all the radiosonde and satellite data matched pairs for a satellite or satellite pair were randomly selected to determine the regression coefficients. The new equation was then applied to the remaining 30% of the matched pairs to determine a bias and root-mean-square error (RMSE) of the inversion strength retrieval. The mean bias and RMSE were then calculated. The magnitude of the mean biases for each satellite were less than 0.1 K, and the mean RMSE were 2.7 K, 2.8 K, 2.8 K, and 2.7 K respectively, for the different satellite or satellite pairs.

The radiosonde data from drifting ice stations ended at 1990, so these data were not used to derive the coefficients of the retrieval equations. However, these data were used to show that the regression equations derived from station data can be applied over other areas. The radiosonde data from drifting stations were matched with satellite data. The regression equations were then applied to the satellite data to derive the 2-channel inversion strength, and compared to the station-based inversion strength to calculate the bias and RMSE. A total of 223 radiosonde and satellite data matched pairs were collected from the drifting stations from 1980 to 1990. The mean bias and RMSE were 0.25 K and 2.5 K.

Radiosonde data at 11 stations (shown as squares in Figure 2.1) were also used to validate the inversion strength monthly means and trends from the 2-channel method and profile inversion strength method. For this validation exercise the radiosonde data from the 11 stations were not used to derive the regression equation coefficients. Each of these 11 stations has at least 50% of all possible 0 and 12 UTC soundings in each month. The inversion strength monthly means and trends from radiosonde data, as well as the 2-channel retrievals at these 11 stations are compared in Figures 2.8 and 2.9. The monthly mean is the mean of all the individual means for that month over the period 1980 – 1996, and the monthly trend is derived using linear least squares regression based on the monthly means. Considering the different sky conditions, the monthly means of 2-channel inversion strength agree with those from station data very well in the cold season, with a bias around 0.3 K. The monthly means of profile inversion strength are lower than those from station data, with the overall bias around –1.5 K, but with the biases as high as –5.5 K for some stations. This comparison shows that 3I algorithm used in the TOVS Path-P processing works well when temperature inversions are present, but there is a systematic low bias in the inversion strength. This may be a result of the coarse vertical resolution of the retrieved temperature profiles, making it difficult to measure the inversion top precisely. In practice, a bias correction could yield a reasonable estimate of inversion strength from the retrieved temperature profiles. However, the 2-channel method is preferred because it is easier to parameterize, is applicable to non-sounding instruments (e.g., MODIS), and is more accurate overall. Trends from the 2-channel and profile methods agree with the trends from station data reasonably well (Figure 2.9).

In the remainder of the paper, the coefficients of the equations used to calculate the monthly mean and trend of the inversion strength were derived based on all the available radiosonde and satellite data matched pairs.

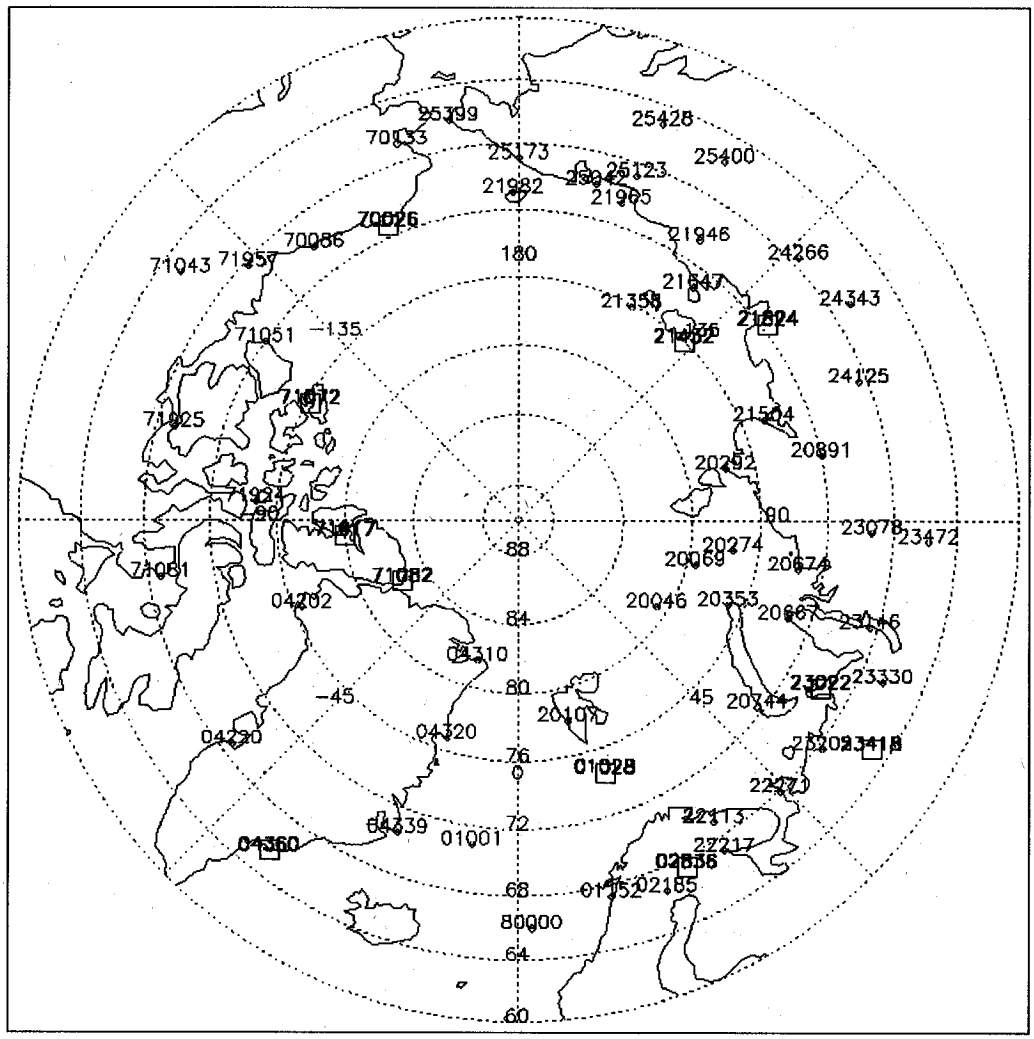


Fig. 2.1. Locations of the weather stations used in this study. Stations shown as squares were used for validation.

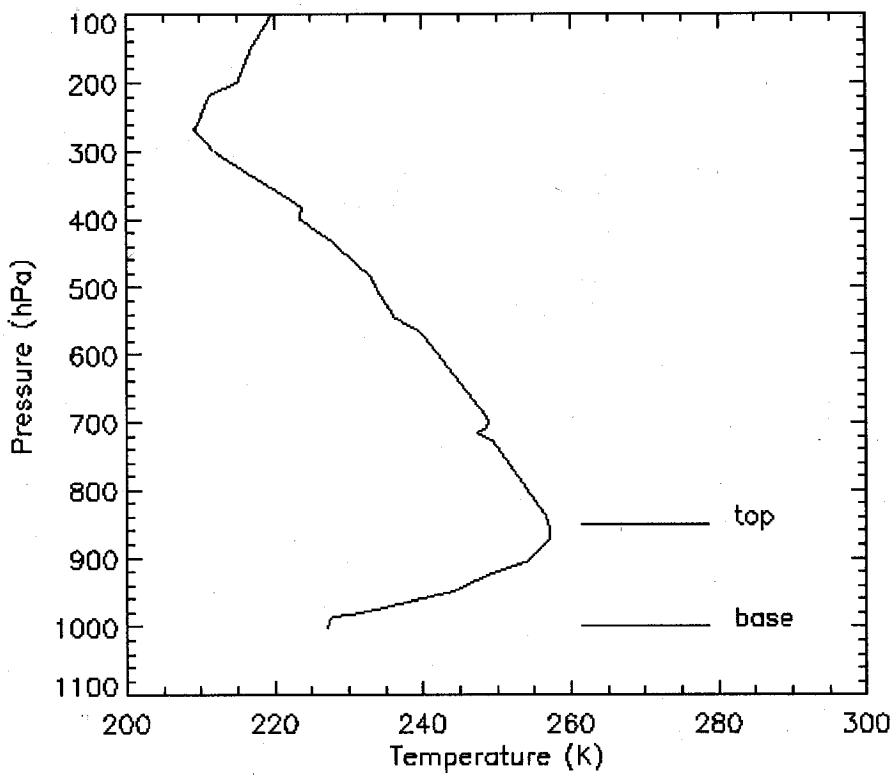


Fig 2.2. Temperature profile measured at Verhojansk , Russia, 1200 UTC on 3 December 2001. Temperature inversion top and base are indicated.

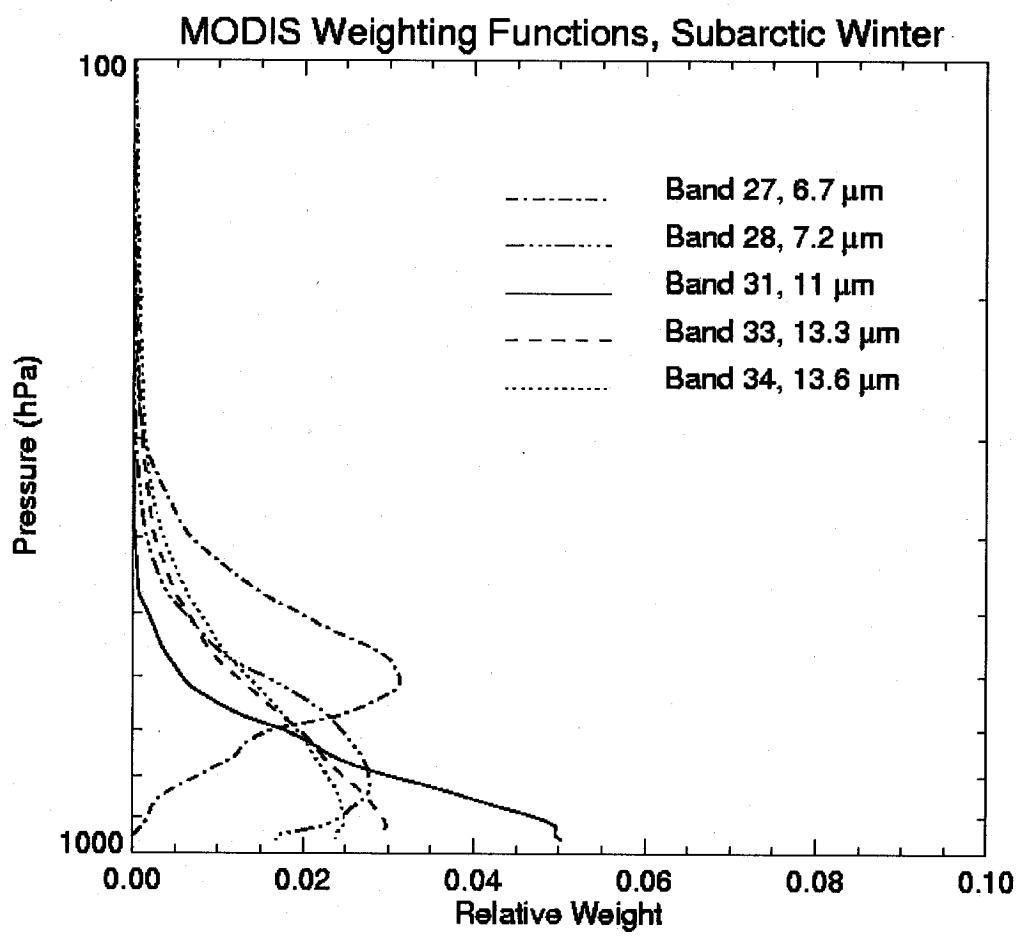


Fig. 2.3. Weighting functions for the MODIS bands at 6.7 μm, 7.2 μm, 11 μm, 13.3 μm, and 13.6 μm using subarctic winter standard atmosphere profile.

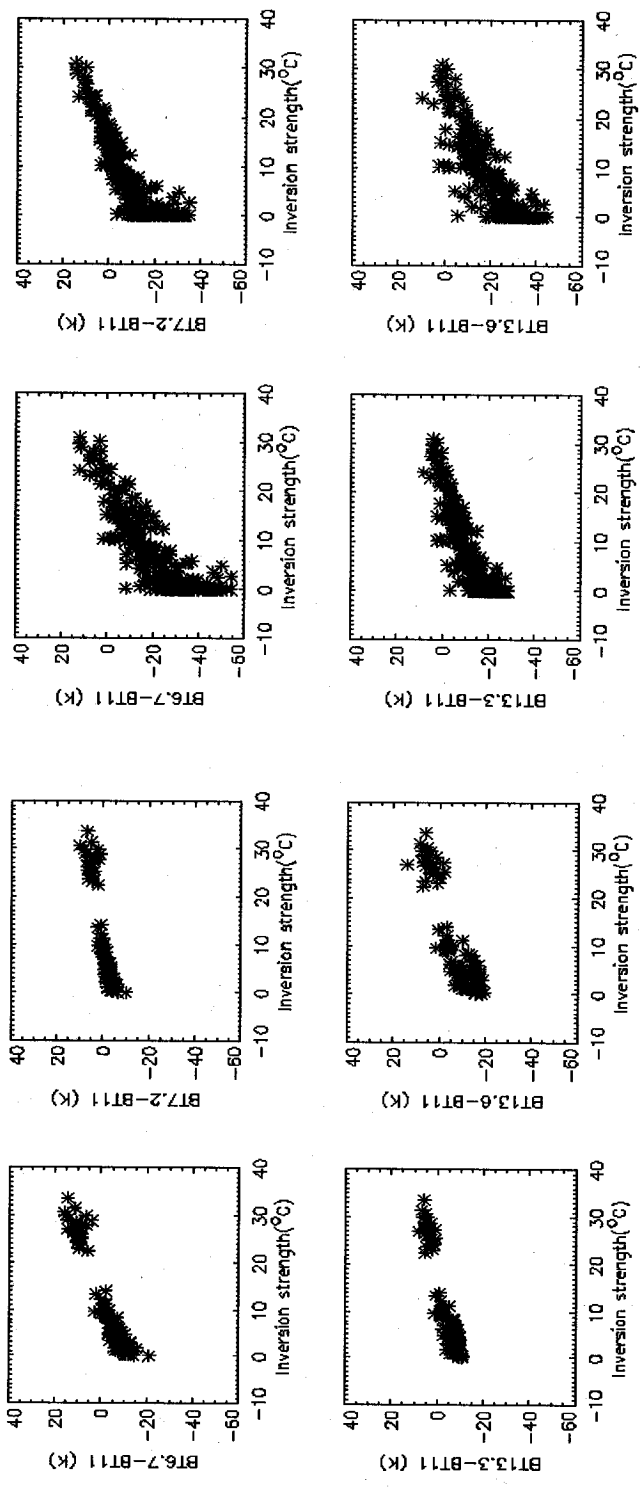


Fig. 2.4. Relationship between simulated brightness temperature difference pairs and the temperature inversion strength over high elevation surfaces (left) and low elevation surfaces (right).

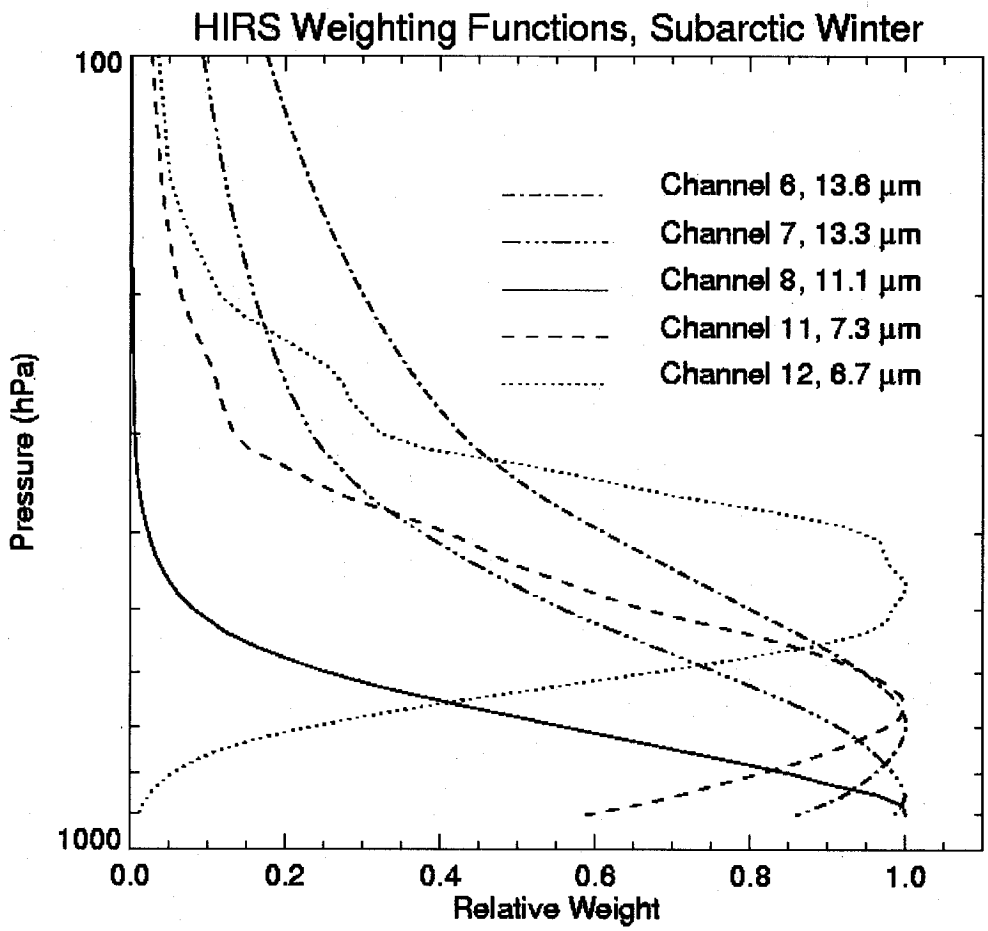


Fig. 2.5. Weighting function for the 6.7 μm, 7.3 μm, 11 μm, 13.3 μm, and 13.6 μm channels based on a subarctic winter standard atmosphere profile.

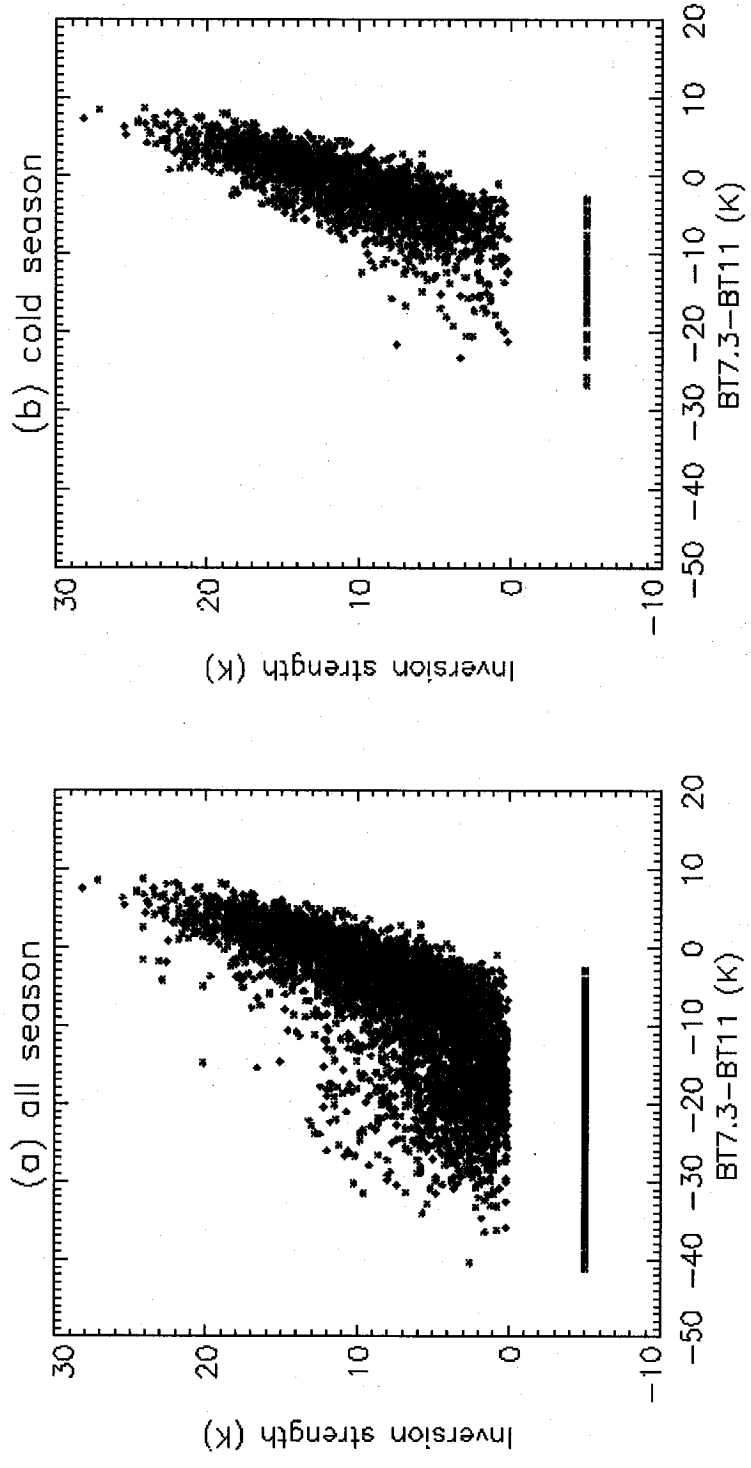


Fig. 2.6. Relationships between inversion strength from radiosonde data and $BT_{7.3}$-$BT_{11}$ for (a) all seasons and (b) for the cold season. Cases with inversion strength less than 0 K are not considered to be inversions.

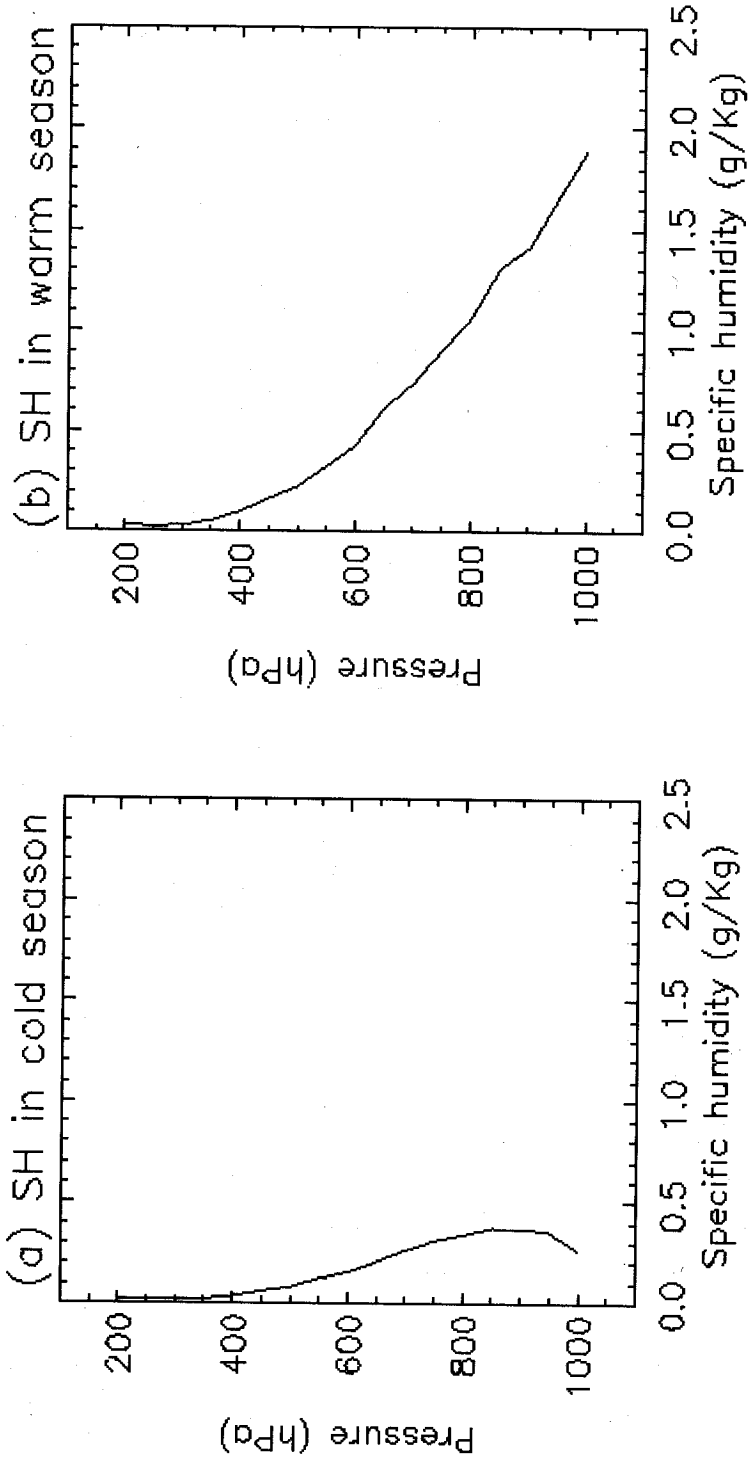


Fig. 2.7. Average specific humidity (SH) profiles in the (a) cold season, and (b) warm season.

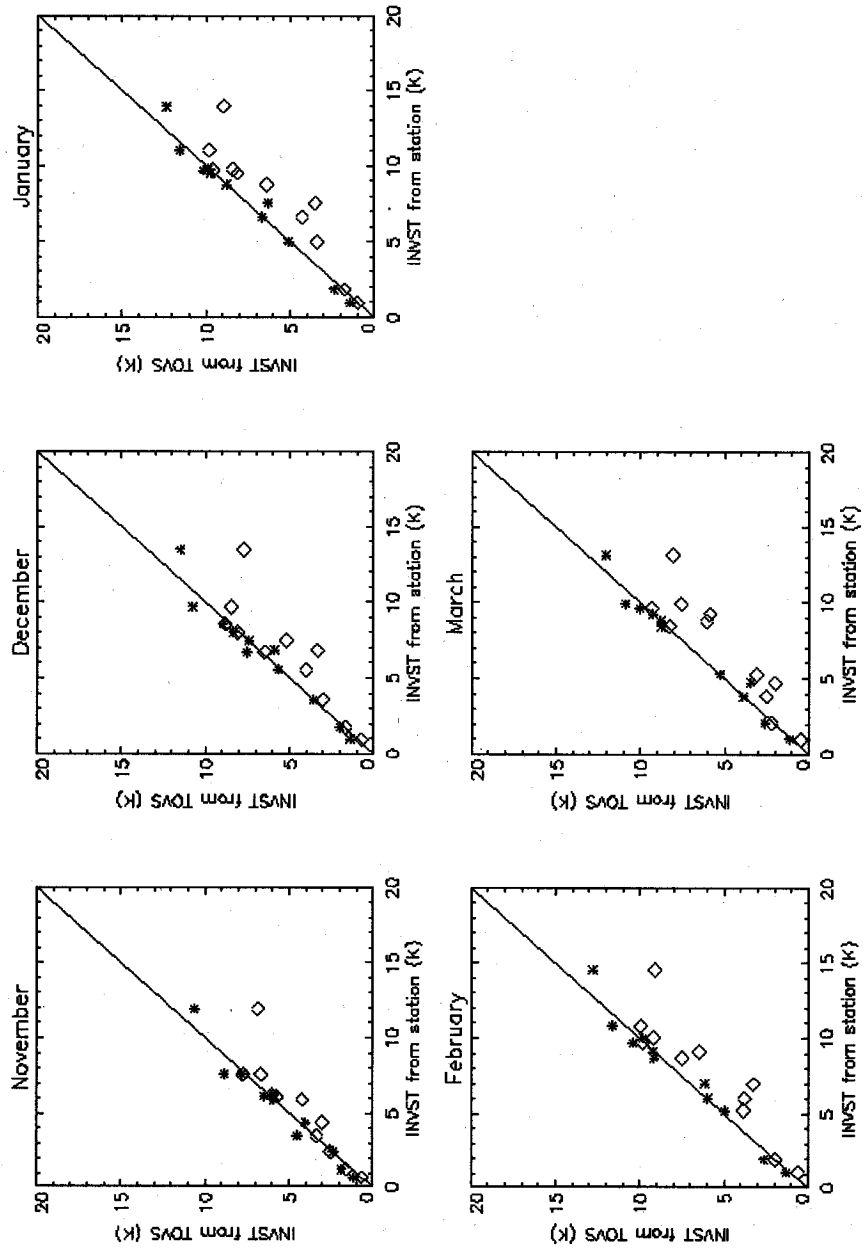


Fig. 2.8. Comparison of monthly mean inversion strength (INVST) from meteorological stations and from HIRS data in cold season months during 1980-1996 at 11 stations. The asterisks represent the results from the 2-channel statistical method; diamonds represent the results from the TOVS retrieved temperature profiles.

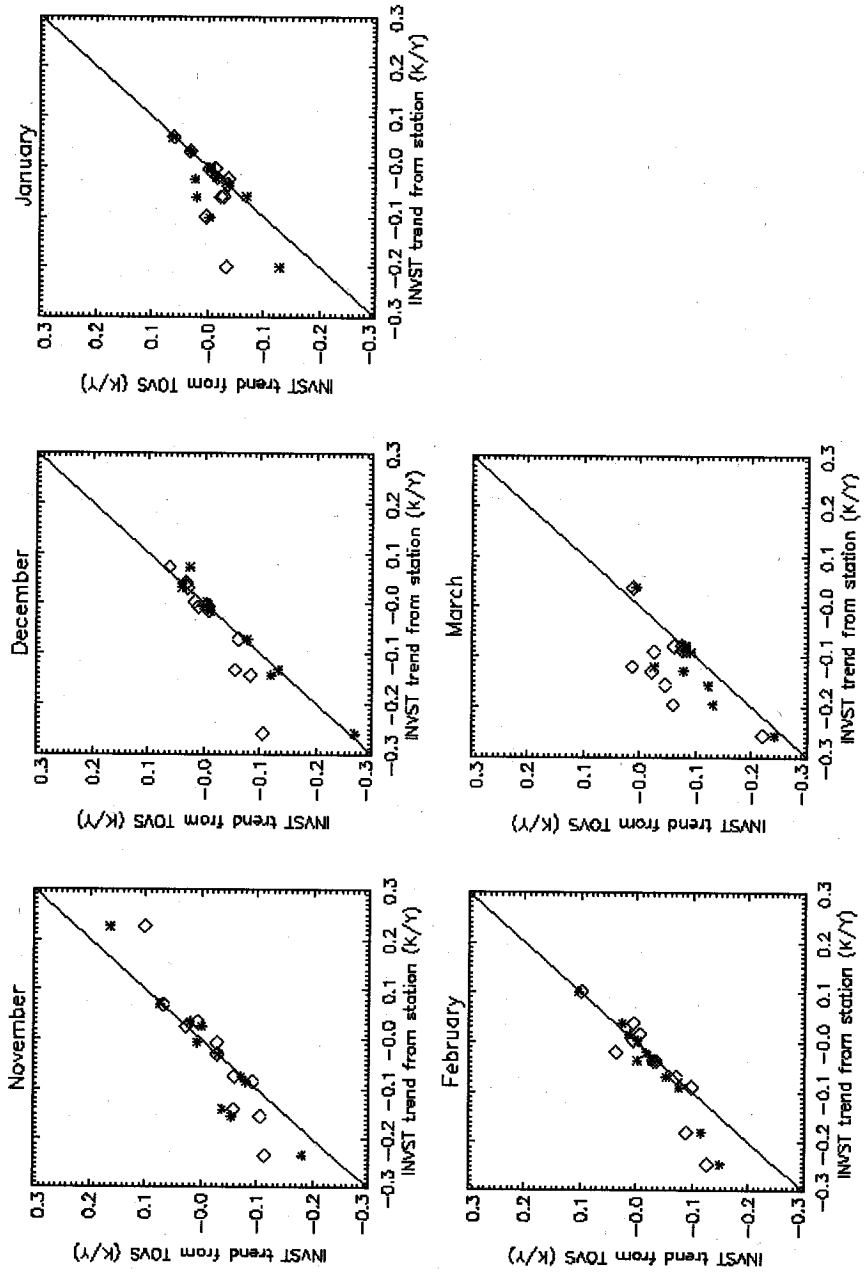


Fig. 2.9. Same as Figure 2.8 but for trends.

Table 2.1. Parameters used in this study.

| Name | Origin Dataset | Time | Format | Conditions |
|---|---|---|---|---|
| Cloud cover | APP-x | 1982-2004 | Monthly Seasonal | |
| Cloud phase | APP-x | 1982-2004 | Monthly Seasonal | |
| Cloud optical depth | APP-x | 1982-2004 | Monthly Seasonal | |
| Surface skin temperature | APP-x | 1982-2004 | Monthly Seasonal | Clear, Cloudy, All-sky |
| Surface skin temperature | TOVS Path-P | 1980-1998 | Monthly Seasonal | Clear, All-sky |
| Sea ice extent, concentration | NASA GSFC Sea ice | 1980-2004 | Monthly Seasonal | |
| Heat convergence | TOVS Path-P NCEP Wind | 1980-2001 | Monthly Seasonal | |
| Moisture convergence | TOVS Path-P NCEP wind | 1980-1998 | Monthly Seasonal | |
| Cloud cover | ERA40 | 1982-2002 | Monthly Seasonal | |
| Surface wind | ERA40 | 1982-2002 | Monthly Seasonal | |
| Sea level pressure | ERA40 | 1982-2002 | Seasonal | |
| Surface 2-m temperature | EAR40 | 1982-2002 | Monthly Seasonal | All-sky |

# 3 Arctic Climate Characteristics: Mean State and Trends

## 3.1 Mean State and Trends in the Arctic 1982-2000

The Arctic is the most sensitive region on earth in regard to climate change, due to various feedback mechanisms, including the important surface albedo and temperature positive feedback. Dramatic changes in surface temperature, cloud amount, heat and moisture convergence, and sea ice concentrations in four seasons of a year from 1982 to 2000 are shown in the following sections. Surface temperature, and cloud amount data are from the APP-x dataset and ERA40 reanalysis; heat and moisture convergence are from TOVS Path-P; and sea ice concentration data are from satellite microwave observations.

### 3.1.1 Surface Temperature

Seasonal means and trends of all-sky surface temperature based on the APP-x dataset at 14:00 LST in four seasons from 1982 to 2000 are calculated on a pixel-by-pixel basis and the results are presented in Figure 3.1.

Over the entire Arctic region, surface temperature is warmest in summer, and coldest in winter. During all four seasons, central Greenland has the lowest surface temperature, which can be attributed to the highest surface altitude and strong surface radiative cooling. In winter, spring, and autumn, the warmest surface temperatures are over the GIN Seas and the Barents Sea because of open ocean water. In winter, lower surface

temperatures appear over land rather than over the ocean due to its stronger surface radiative cooling. Over the Arctic Ocean, the coldest temperatures are in the western Arctic north of Canada. In spring and autumn, the lowest temperatures exist in the western Arctic north of Canada and become warmer towards land. In summer, the surface temperature over land is warmer than over the ocean, where the surface temperatures are isothermal around 0 °C.

In winter and autumn, surface temperature basically increases over the western Arctic and decreases over the eastern Arctic; in spring and summer, positive surface temperature trends can be seen all over the Arctic. In winter, surface temperature increases over northern Canada, with the greatest increase over the Hudson Bay. Surface temperature decreases over the Arctic Ocean, with the maximum negative trend approximately -2.5 K/decade over the central Arctic Ocean. Surface temperature also decreases around the Bering Strait. In spring, significant warming is seen over most of the Arctic, including the central Arctic Ocean, most of northern Canada, and north central Russia, with the maximum positive trend around 2.0 K/decade. In summer, surface temperature is generally increasing, with a smaller magnitude over the Arctic Ocean than over land. Strong positive trends can be seen over northeastern Russia, Alaska and northern Canada with the maximum trend around 1.5 K/decade. Over the central Arctic Ocean and north central Russia, trends are near zero. In autumn, there are strong positive surface temperature trends over the Beaufort and Chukchi Seas, Alaska, and northern Canada, with the maximum trend around 2.0 K/decade. The surface temperature trend over most of the Arctic Ocean is negative, with the magnitude around -0.5 K/decade. In

all four seasons, surface temperature trends over northern Europe are positive. Trends based on the APP-x all-sky surface temperature at 04:00 LST are similar (not shown).

Comparison of the APP-x surface skin temperature trend with 2-m air temperature trends in four seasons from the ERA40 reanalysis in the Arctic indicates very similar patterns, which are shown in Fig 3.2. It should be noted that AVHRR data were not assimilated in the ERA-40 reanalysis. The APP-x trends are calculated based on the APP-x all-sky surface skin temperature at 1400 LST; the ERA-40 trends are calculated based on the monthly mean of all four daily times of 2-m air temperature. Distributions of the positive and negative tends in four seasons from the two datasets are very similar. Difference exists in the absolute magnitude of the trends over the Arctic Ocean in winter.

### 3.1.2 Cloud Cover

Seasonal means and trends of cloud cover based on the APP-x dataset in four seasons from 1982 to 2000 are calculated on a pixel-by-pixel basis and the results are presented in Figure 3.3.

Over the entire Arctic region, cloud fraction is highest (85%) in summer, and lowest in spring (55%). In four seasons, the highest cloud fraction is over the GIN Seas and Barents Sea (80%); the lowest cloud fraction is over central Greenland. In winter, the cloud fraction over the Arctic Ocean (60%) is higher than that over northern Canada and northern Russia (45%). In spring, the lowest cloud cover is over the Arctic Ocean (40%) and part of northern Canada.

In winter, significant decrease in cloud cover is seen over the Arctic Ocean, with the maximum trend around –15%/decade. This decreasing cloud cover is consistent with the decreasing surface temperature trend over the same region. There is no significant trend in cloud cover over land. In spring, trends in cloud cover are positive over most of the Arctic region, with significant positive trends over northern Canada, the Beaufort and Chukchi Seas, and north central Russia, with the maximum trend around 7%/decade. In summer, positive cloud cover trends are seen over the Beaufort and Chukchi Seas, and north central Russia. There are no significant trends over any other region. In autumn, there are no apparent trends over the Arctic. However, positive trends can be seen over the Beaufort and Chukchi Seas, and northern Canada.

Schweiger (2004) investigated changes in cloudiness during winter and spring over the Arctic seas from the TOVS Polar Pathfinder retrievals. He found significant decreases in winter and equally striking increases in spring in cloud fraction, which is consistent with the patterns in the APP-x.

Total cloud cover trends in four seasons from the ERA40 reanalysis in the Arctic are shown in Fig 3.4. Negative trends of cloud cover are seen in four seasons over the Arctic Ocean, which agrees with APP-x results in winter, however disagrees with APP-x results in other seasons. All the positive trends are not significant.

### 3.1.3 Sea Ice Concentration

Sea ice is an important component of the Arctic climate system. It is influenced by both atmospheric and oceanic conditions and in turn it feeds back into these conditions.

Changes in the sea ice can change the surface albedo, the exchanges of the heat and moisture, momentum between the atmosphere and ocean, and the upper ocean stratification in areas where deep water is formed. Sea ice cover in the Arctic decreased by 2.9% per decade from 1979-1996 (Cavalieri et al. 1997), with the maximum reductions (6% /decade) in summer (Maslanik et al. 1996). In winter, the ice extent in the Arctic has remained stable, but large trends of opposing sign are apparent in different regions for the period from 1979-1996 (Parkinson et al., 1999).

Seasonal means and trends of sea ice concentrations based on SMMR and SSM/I in four seasons from 1982-2000 are calculated on a pixel-by-pixel basis and the results are presented in Figure 3.5.

Over the entire Arctic region, sea ice concentration is highest in winter and lowest in summer. In the GIN and Barents Seas, sea ice concentration is lower than 15%. In winter and spring, sea ice concentration over most of the central Arctic Ocean is higher than 90%. In summer and autumn, sea ice concentration increases from coastal areas (less than 15%) to the central Arctic (90% around 80° N).

In winter, sea ice concentration increases over most of the Arctic Ocean, with the maximum trend around 3.0%/decade over the Canada Basin. This increasing sea ice concentration is consistent with the cooling surface temperature, and decreasing cloud cover over most of the Arctic Ocean. Meanwhile, decreasing sea ice concentration trends are seen over the Hudson and Baffin Bays, and around the sea ice edge in the Barents and Kara Seas. In spring, sea ice concentration shows similar trend as those in winter, which is not consistent with the general increasing surface temperature trend over the Arctic in

spring. In summer and autumn, sea ice concentration decreases over most of the Arctic Ocean, with the maximum negative trend exceeding –5.0%/decade over the Beaufort and Chukchi Seas, which is consistent with the increasing surface temperature in summer and autumn over the Arctic. Positive trends of sea ice concentration are seen across the Canada Basin and Kara Sea in autumn.

### 3.1.4 Moisture and Heat Convergence

Atmospheric moisture budget is an important component of the Arctic climate system. Some of the moisture transported to the Arctic condenses to form clouds and precipitates as snow and rain. The snowfall increases the surface albedo of sea ice and changes the surface energy balance. Cloud cover also affects the surface energy budget; in turn it influences the surface temperature. Cloud cover trend in the Arctic might also be affected by the moisture convergence trend.

The seasonal means and trends regarding moisture convergence in four seasons from 1982-1998 in the Arctic are presented in Figure 3.6. In winter, moisture convergence is highest over the Atlantic sector, including the GIN and Barents Seas, exceeding 3cm/month near Iceland and Norway. Moisture convergence is smallest across the Beaufort Sea region and ranges between 0.5 and 1.0 cm/month over most of the central Arctic. In summer, moisture convergence exceeds 2 cm/month over most of the Arctic Ocean, and is more uniformly distributed than in winter, with the minimum over the Beaufort Sea.

In winter, there are positive trends in moisture convergence over the Canada basin and the eastern GIN Sea areas; negative trends are found over portions of the Nansen Basin, the Barents and Kara Seas, and around the Bering Strait. In spring, positive trends of moisture convergence are found over the Beaufort and Chukchi Seas, north central Russia, and part of northern Canada, which corresponds with positive trends in cloud cover across these regions.

Heat convergence is an important component of the atmosphere energy budget. Changes in the heat convergence affect atmospheric temperature, which in turn changes the outgoing longwave radiation at the top of the atmosphere and the atmospheric profile structure. Changes in the atmospheric profile structure will eventually affect the surface energy budget.

Seasonal trends in heat convergence in four seasons from 1982-2000 in the Arctic are presented in Figure 3.7. In winter, there are positive trends of heat convergence over portions of the Chukchi Sea, the Alaska region, and northern Europe, with the maximum trend over 5 W/decade; negative trends are found over regions surrounding the Nansen Basin, north central Russia, and around the Bering Strait, with the maximum negative trend over –5.0 W/decade.

### 3.1.5 Clear-sky Temperature Inversion Strength

Figure 3.8a shows the spatial distribution of monthly mean, clear-sky 2-channel inversion strength in the Arctic for November - March, and for winter (DJF) averaged over the period 1980-1996. The spatial distributions have similar patterns from

November to March, but with different magnitudes. The lowest monthly mean 2-channel inversion strength is over Greenland and Norwegian (GIN) Seas, Barents Sea, and northern Europe, which is attributable to the turbulent mixing over open water and high cloud cover in this region during the winter time (Serreze et al. 1992). The inversion strength increases eastward, followed by a decrease over Alaska. Over land, the strong monthly mean inversion strength can be seen over northern Russia and northern Canada, with the largest values near several Russian river valleys owing to strong radiative cooling under clear conditions. Over the Arctic Ocean, the largest values are over the pack ice north of Greenland and the Canadian Archipelago; the lowest values are in the Kara, Laptev, and Chukchi Seas. Temporally, the monthly mean inversion strength over the ocean is largest in February (~16K) and smallest in November (~12K) over the pack ice north of Canada. Similarly, the strongest inversions over land occur in January and February, and the weakest in November and March.

The monthly trend of the clear-sky inversion strength is shown in Figure 3.8a. The spatial distribution of monthly trends is similar in December, January, and February. The winter average trend shows decreases in inversion strength over the Chukchi Seas, with an average around –0.13 K/year. The inversion strength also decreases over northern Europe with average rate around –0.13 K/year. Inversion strength increases over north central Russia at rate around 0.10 K/year, and increases in northeastern Russia, and also between Sevemaya Zemlya and North Pole at the rate of 0.13 K/year. All the changes are statistically significant at the 90% or higher confidence level based on the F-test. In March, the inversion strength decreases significantly over the Laptev, Chukchi, and

Beaufort Seas at a rate over –0.10 K/year; and decreases in regions surrounding Novaya Zemlya and north central Russia at a rate over –0.10 K/year. The decreasing rate over northern Europe is more than –0.05 K/year. In November, there has been a significant decrease in inversion strength over the Chukchi and Beaufort Seas at a rate over –0.10 K/year.

The monthly means and monthly trends of the TOVS profile temperature inversion strength under clear sky conditions are shown in Figures 3.8b. The spatial patterns are similar to those from the 2-channel retrievals, but the profile inversion strength monthly mean has a smaller magnitude of 2-5K. This may be in part a result of the relatively coarse vertical resolution of the TOVS retrieved temperature profiles in the lower troposphere.

Kahl and Martinez (1996) found significant increases in inversion strength over the Arctic Ocean during winter and autumn from 1950 through 1990. Based on their Figure 6, the inversion strength increase occurred primarily between 1950 and the late 1970s. After 1980, they did not find any significant increase of inversion strength. That result is consistent with the present overall (Figure 4.10a), where much of the Arctic Ocean shows no trend. However, the inversion strength over some areas exhibits a strengthening trend and others show a weakening trend from 1980 through 1996.

## 3.2 Connections to the Arctic Oscillation

The Arctic Oscillation (AO) (Thompson and Wallace 1998) is the first principal component of the empirical orthogonal function of monthly sea level pressure poleward

of 20°N. The AO pattern can be interpreted as the surface signature of modulation in the strength of the polar vortex aloft. The AO exhibits significant intra-seasonal and inter-annual variability, and showed trends toward high index polarity during the 1990s. Thompson et al. (2000) showed that the AO accounts for one third of the 30-year positive temperature trend over northern Eurasia. Rigor et al. (2000) found that changes in AO account for more than half of surface air temperature trends over Alaska, Eurasia, and the eastern Arctic Ocean, but less than half in the western Arctic Ocean.

Following the analysis by Thompson et al. (2000) of SAT trends over the northern land areas, and the analysis by Rigor et al. of SAT trends over the Arctic Ocean, we estimate the contribution of the AO to the trends in surface temperature, cloud cover, sea ice concentration, moisture and heat convergence in four seasons in the Arctic from 1982-2000. The contribution of the AO is calculated by regressing the surface skin temperature on the AO index and multiplying by the trend in the AO, which is called AO-related trend in this study.

The AO related trend, total trend, and residual trend (the difference between the total trend and AO related trend) of surface skin temperature in the Arctic in four seasons from 1982-2000 are shown in Fig. 3.9. In winter, the AO related trend explains around 0.5 K/decade over northern Eurasia, and –0.5 K/decade over Alaska, together contributing more than half of the total trend. In autumn, the AO related trend is around 0.5 K/decade over the central Arctic Ocean, and –1.0 K/decade over north central Russia, which explains over half of the total trend over the Nansen Basin, North Pole, Laptev Sea, and north central Russia. For the ERA40 2-m air temperature trend (Figure 3.10), a similar

significant AO related trend exists over some regions of the Arctic in autumn and winter, and they explain more than half of the total trends over these regions. Trends in the surface temperature cannot be completely explained by changes in the AO. In winter, residual trends show significant warming over northern Canada and cooling over the Arctic Ocean. In autumn, residual trends show significant warming over the Beaufort and Chukchi Seas. In spring and summer, AO related trends are not significant.

The AO related trend, total trend, and residual trend of cloud cover in the Arctic in four seasons from 1982-2000 are shown in Fig. 3.11. In four seasons, there are no significant AO-related trends in cloud cover, which means the cloud cover is not directly related to the larger-scale atmospheric circulation changes, e.g., AO index changes. The same conclusion is found for the ERA40 total cloud cover trend (Figure 3.12).

For the sea ice concentration trend, the AO related trend, total trend, and residual trend in the Arctic in four seasons from 1982-2000 are shown in Fig. 3.13. In autumn, the AO-related sea ice concentration decreasing trend along the sea ice edge on the Atlantic side, mostly over the Nansen Basin, is around –4.0%/decade, which explains more than half of the total decreasing sea ice concentration. For the observed sea ice concentration decrease in the Beaufort and Chukchi Seas in summer and autumn, the AO-related trend in summer shows the opposite trend sign; the AO-related trend in autumn can explain one-third of the total trend over part of the region.

For the moisture convergence trend (Figure 3.14), the AO related trends show non-negligible magnitude in winter, summer, and autumn. However, these trends either have signs opposite to the total trend, or do not explain significant parts of the total trend.

Since the wind field, which is related to large scale atmospheric circulation change, influences the moisture advection, the moisture convergence trend is expected to be related to the AO index. The reason behind the disagreement between what is observed and expected needs further investigation.

For the heat convergence trend, the AO related-trend (column 1), total trend (column 2), and residual trend (the difference between the total trend and the AO-related trend (column 3) in the Arctic in four seasons are shown in Fig. 3.15. The regions for which the AO-related trend explains around half of the total trend include part of the Chukchi Sea in winter, northern Europe in winter, and part of GIN and Barents Seas in autumn.

Trends in each parameter cannot simply and totally be explained by the changes in the AO. Detailed study about the mechanisms behind these changes is required.

## 3.3 Possible Causes of the Clear-sky Inversion Strength Trends

Given the strong coupling of surface temperature and inversion strength by means of radiative cooling, trends in surface temperature should be correlated with trends in inversion strength. Figure 3.16 shows the monthly surface skin temperature trend based on the TOVS Path-P surface skin temperature retrievals in the cold season, averaged over the period 1980 – 1996. In the cold season, areas with decreasing trends in inversion strength are generally those areas that show increasing surface skin temperature trends (e.g., northern Europe in winter). Similarly, areas with increasing inversion strength trends are generally areas with decreasing surface skin temperature trends (e.g., north central Russia in winter).

The correlation coefficient between the monthly mean surface skin temperature anomalies and monthly mean 2-channel inversion strength anomalies for November to March over the period 1980 to 1996 is shown in Figure 3.17. The negative correlation coefficients are less than -0.6 over northern Europe, north central Russia, Alaska and part of northeastern Russia, which means the inversion strength trend over these regions is closely related to the surface skin temperature trend. This is, in fact, the case for most of the Arctic.

Correlation coefficient between the monthly mean surface skin temperature anomalies and monthly mean 2-channel inversion strength anomalies is near zero from the Canadian Archipelago across the central Arctic Ocean and through the East Siberian Sea into Siberia. For most of this area the surface temperature trend is near zero (Figure 3.16), but some portions exhibit statistically significant positive or negative inversion strength trends (Figure 3.8a). It is possible that in these areas the trend in inversion strength trend may be more a function of changes in heat advection into or out of the Arctic than changes in surface temperature. For example, the inversion strengths decrease over the East Siberian Sea, but the surface skin temperature shows little or no trend. The weakening of the inversion in that area may result from cold air advection and a decrease in the temperature of the atmosphere aloft, which effectively decrease the inversion strength.

The relationship between changes in inversion strength, surface temperature, and large-scale circulation are illustrated in Figure 3.18, which shows the correlation between the cold season monthly mean anomalies of surface skin temperature and the Arctic

Oscillation index, and between the inversion strength anomalies and the AO index. The correlation between the surface temperature and AO anomalies is positive in northern Europe and northern Russia but negative over the Canadian Archipelago and Alaska. This is very similar to the results given by Wang and Key (2003). The inversion strength and AO index correlation is negative over northern Europe, north central Russia and the East Siberian Sea, and positive over the Canadian Archipelago. Over the East Siberian Sea the correlation between the AO and surface temperature is near zero or negative, but the correlation coefficient between the AO and inversion strength is significantly negative. As described above, this implies a change in the temperature of the atmosphere aloft as a result of changes in large-scale circulation.

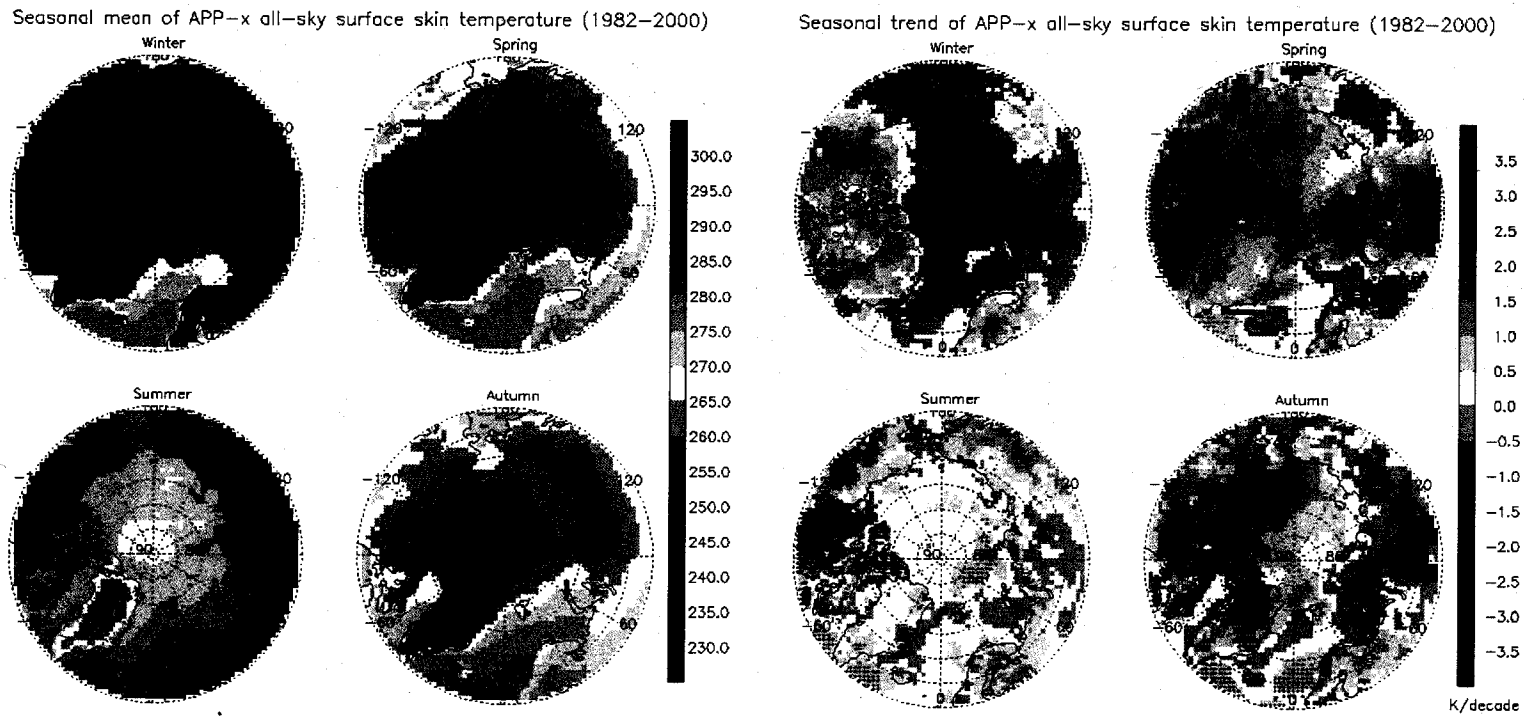


Fig.3.1. Surface skin temperature mean (unit: K, left) and trend (unit: K/decade, right) in four seasons from 1982 to 2000 from APP-x. A trend with a confidence level larger than 95% based on the F test is indicated with +.

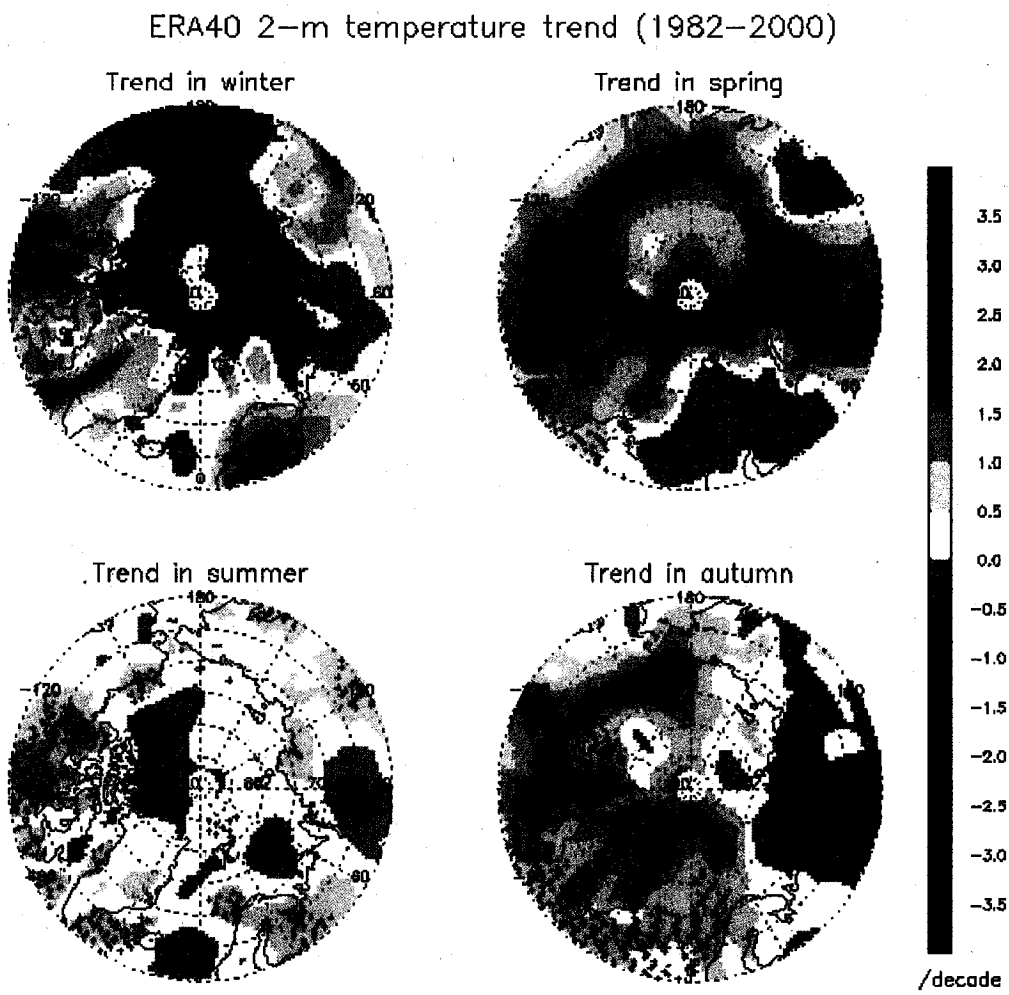


Fig. 3.2. 2-m air temperature trend (unit: K/decade, right) in four seasons from 1982 to 2000 based on ERA40. A trend with a confidence level larger than 95% based on the F test is indicated with +.

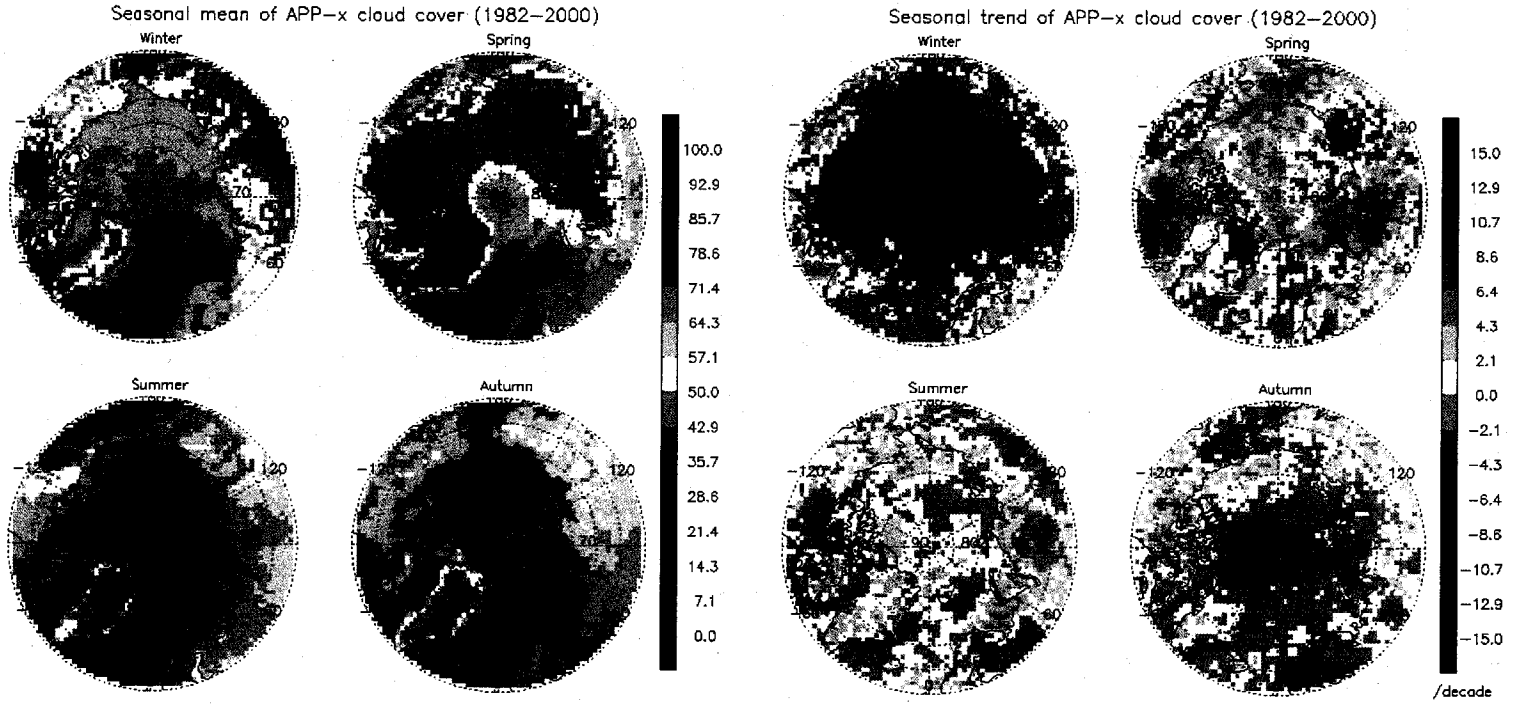


Fig. 3.3. Cloud cover mean (left) and trend (right) in four seasons from 1982 to 2000 from APP-x. A trend with a confidence level larger than 95% based on the F test is indicated with +.

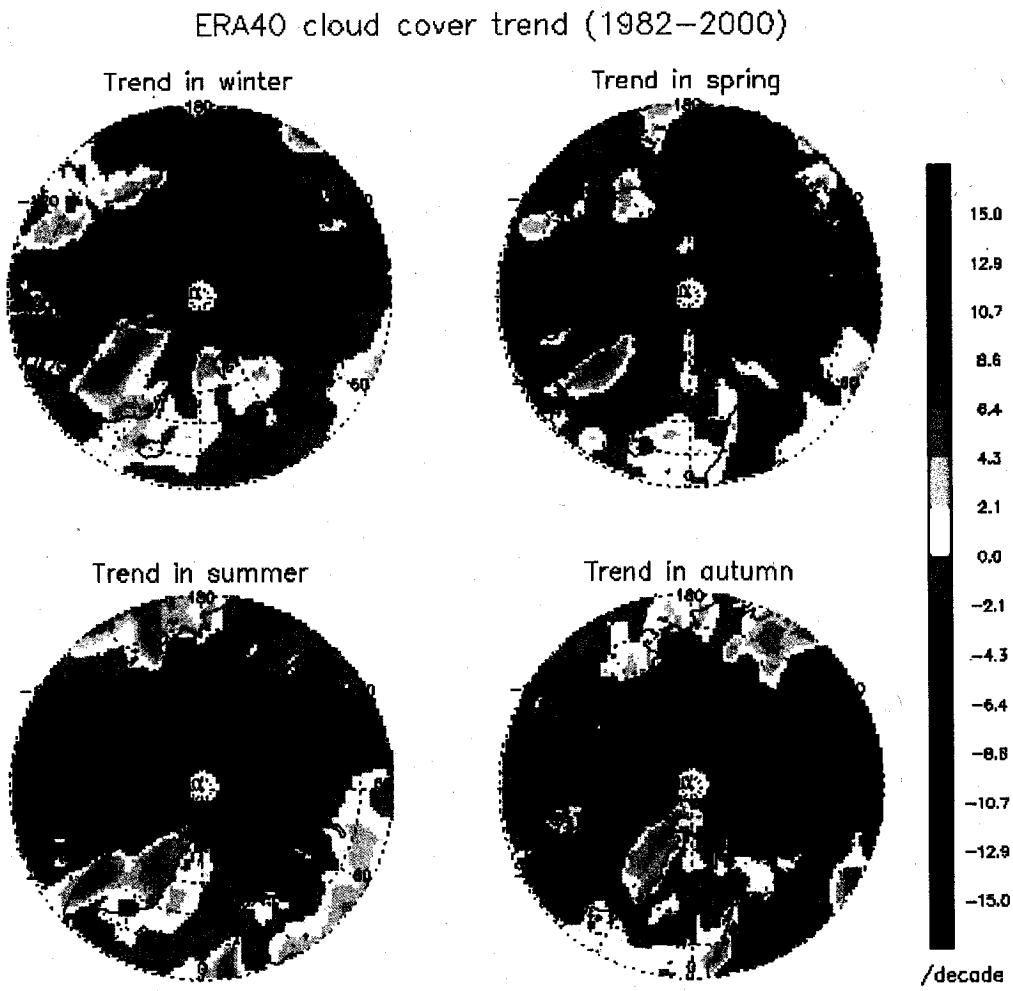


Fig. 3.4. Cloud cover trend in four seasons from 1982 to 2000 based on ERA40 reanalysis. A trend with a confidence level larger than 95% based on the F test is indicated with +.

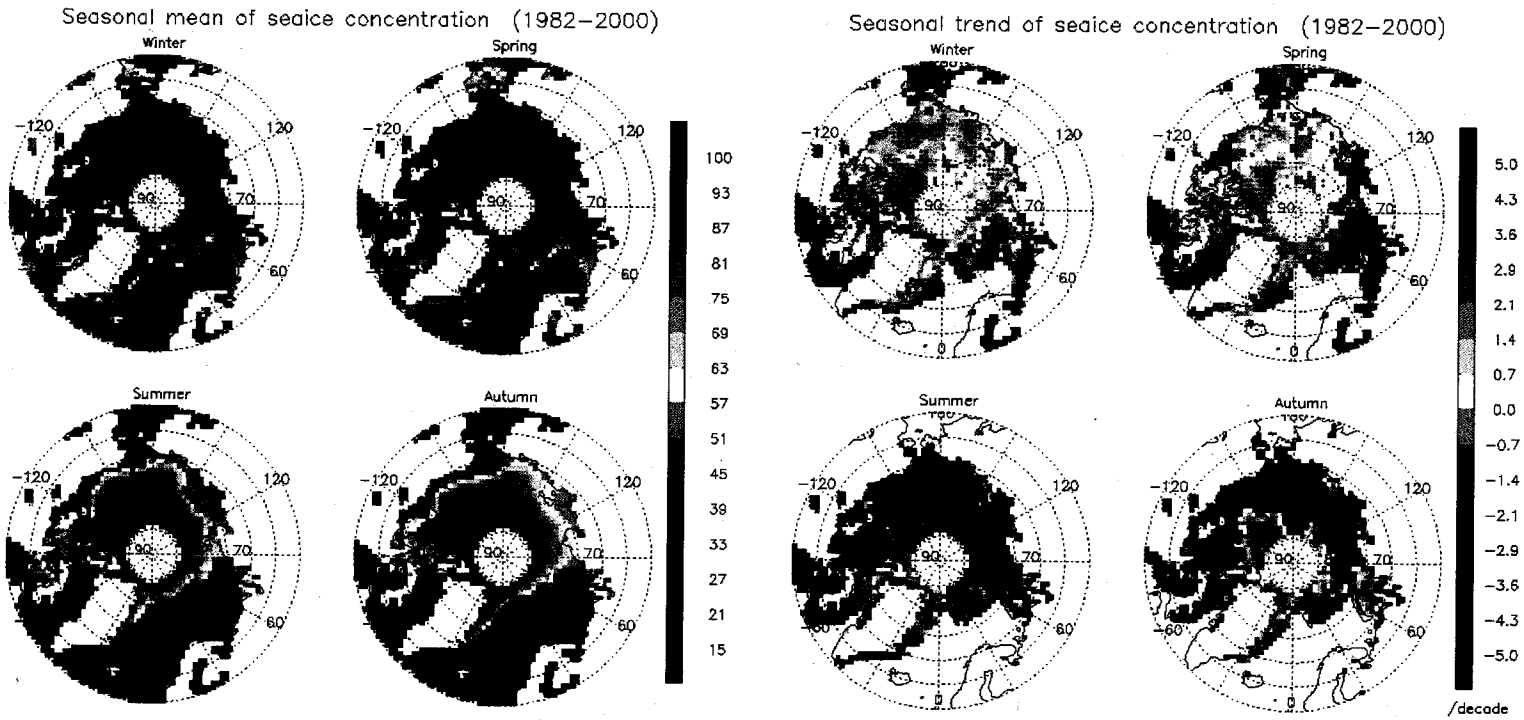


Fig. 3.5. Sea ice concentration mean (left) and trend (right) in four seasons from 1982 to 2000 based on microwave data. A trend with a confidence level larger than 95% based on the F test is indicated with +.

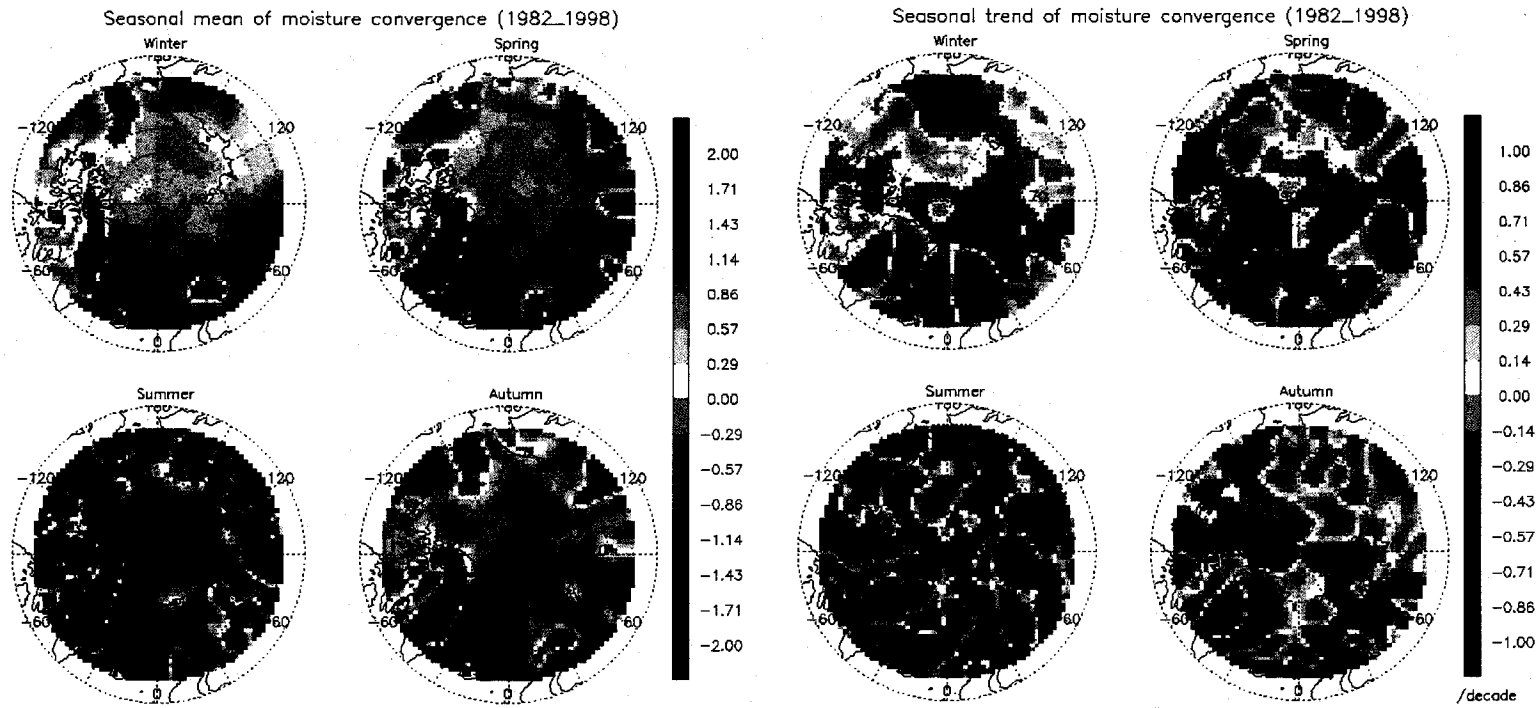


Fig. 3.6. Moisture convergence mean (unit: cm/month, left) and trend (right) in four seasons from 1982 to 2000 from TOVS Path-P. A trend with a confidence level larger than 95% based on the F test is indicated with +.

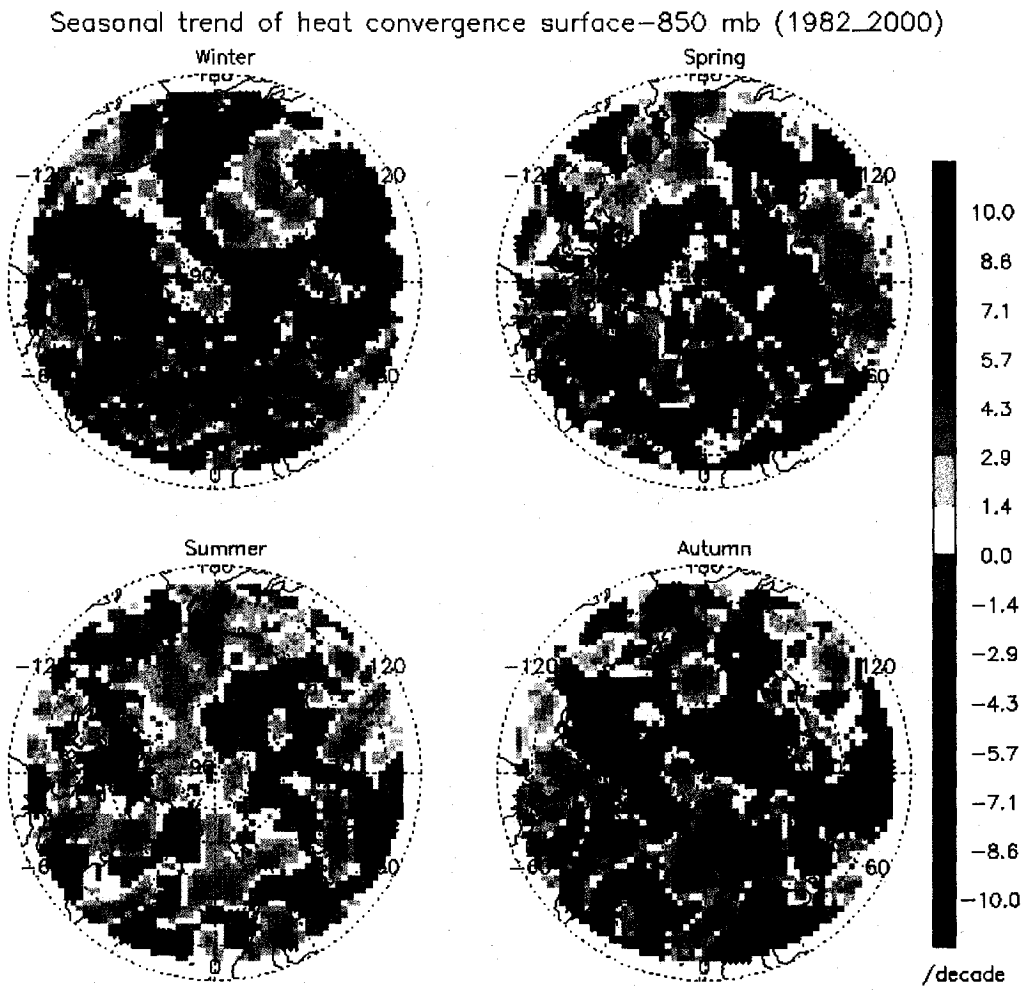


Fig. 3.7. Heat convergence trend (unit: W/m$^2$/decade) in four seasons from 1982 to 2000 from TOVS Path-P. A trend with a confidence level larger than 95% based on the F test is indicated with +.

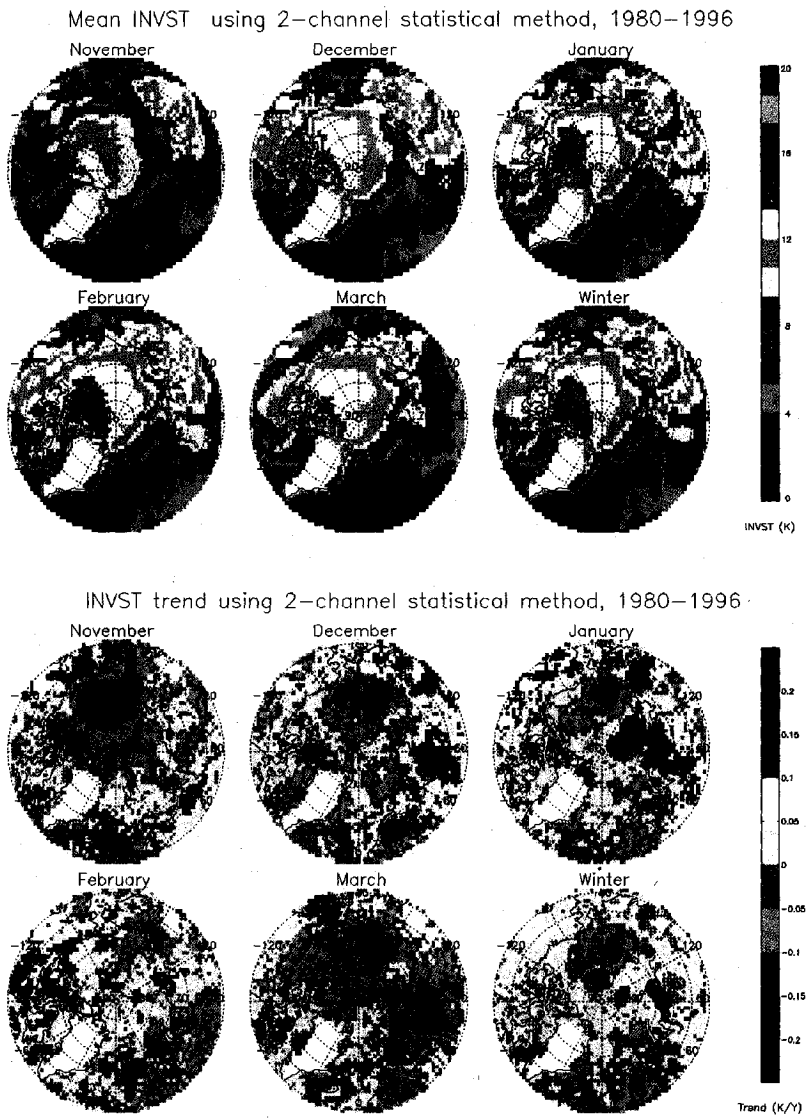


Fig. 3.8a. Monthly mean clear-sky inversion strength (K) (top), and monthly trend of clear-sky inversion strength (K/year) (bottom) in November, December, January, February, March, and winter (DJF), 1980-1996, using the 2-channel statistical method. A trend with a confidence level larger than 90% based on the F test is indicated with +.

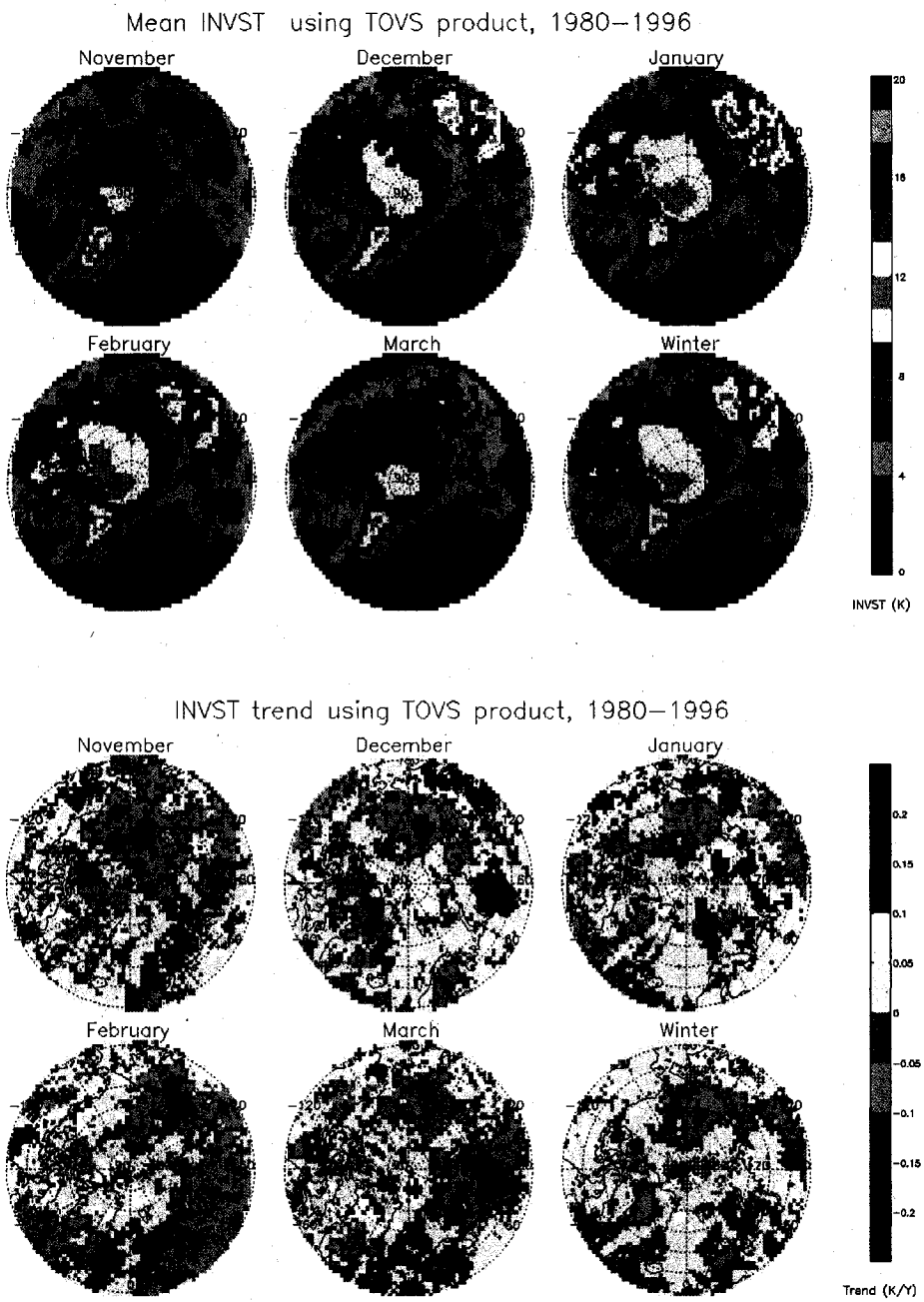


Fig. 3.8b. Same as Fig. 3.8a, but for TOVS profile inversions. The regions with high surface elevation are not indicated as white in this figure.

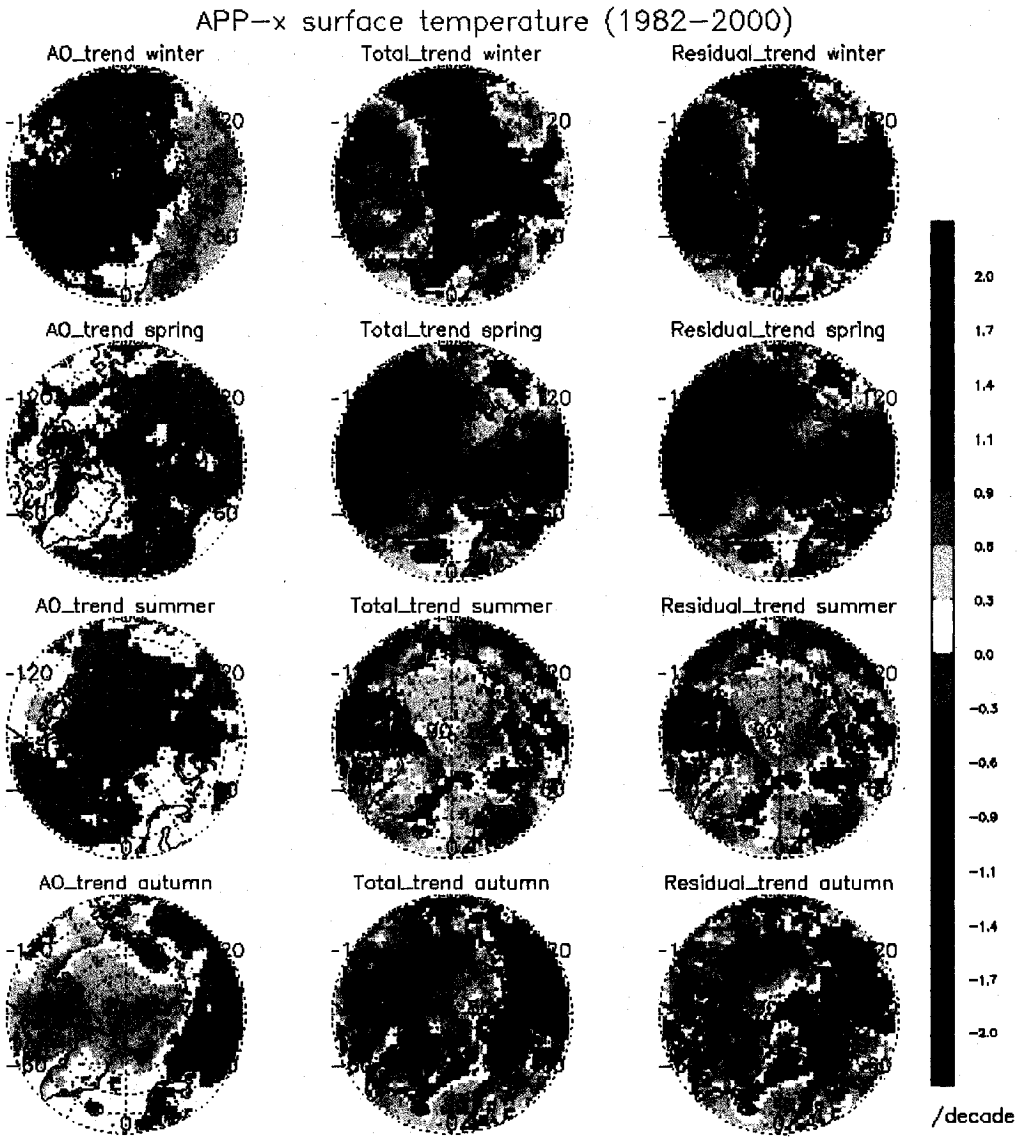


Fig. 3.9. The AO related trend (column 1), total trend (column 2), and residual trend (column 3) of surface skin temperature in four seasons from 1982 to 2000.

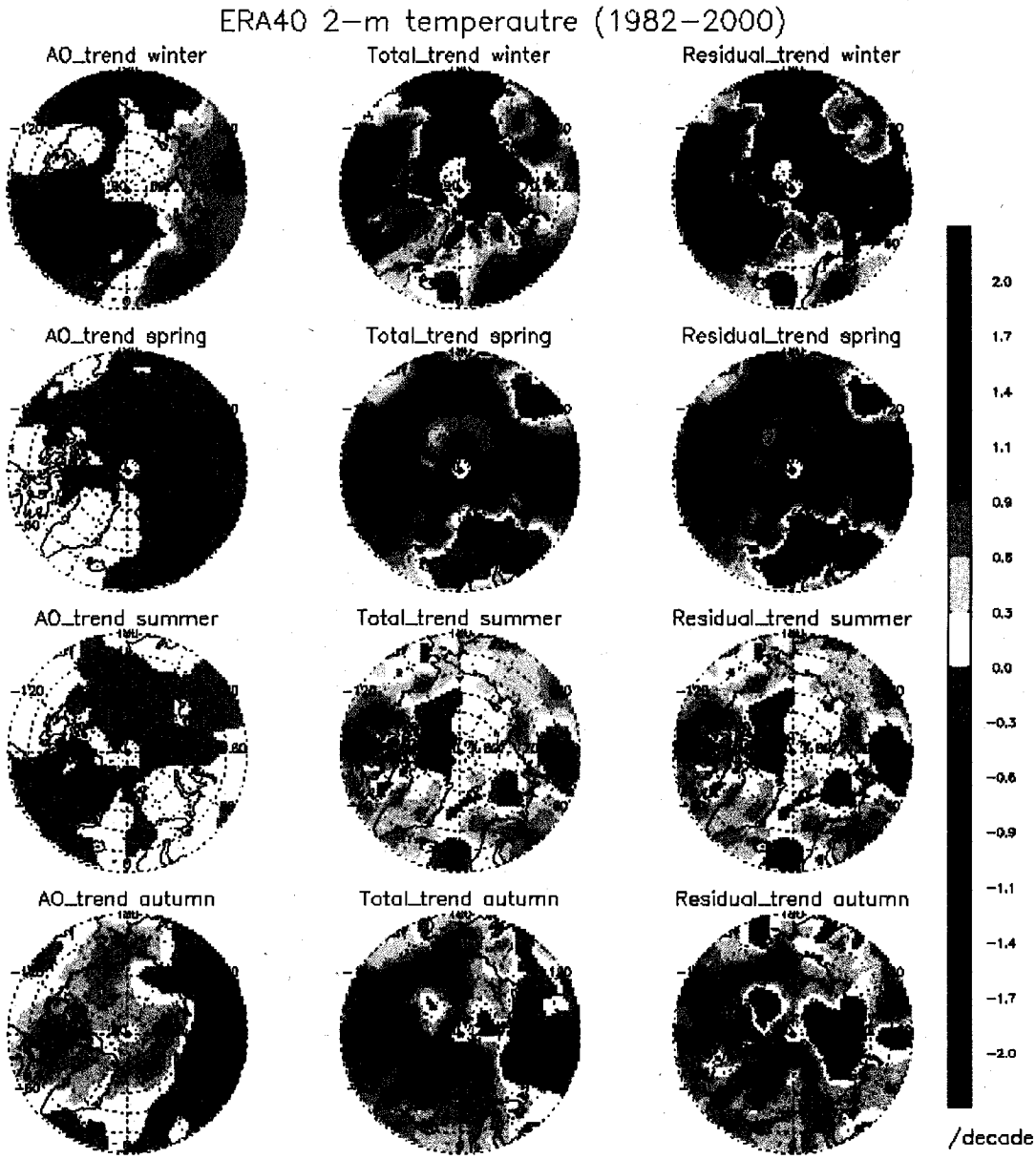


Fig. 3.10. The AO related trend (column 1), total trend (column 2), and residual trend (column 3) of 2-m air temperature in four seasons from 1982 to 2000 from ERA40.

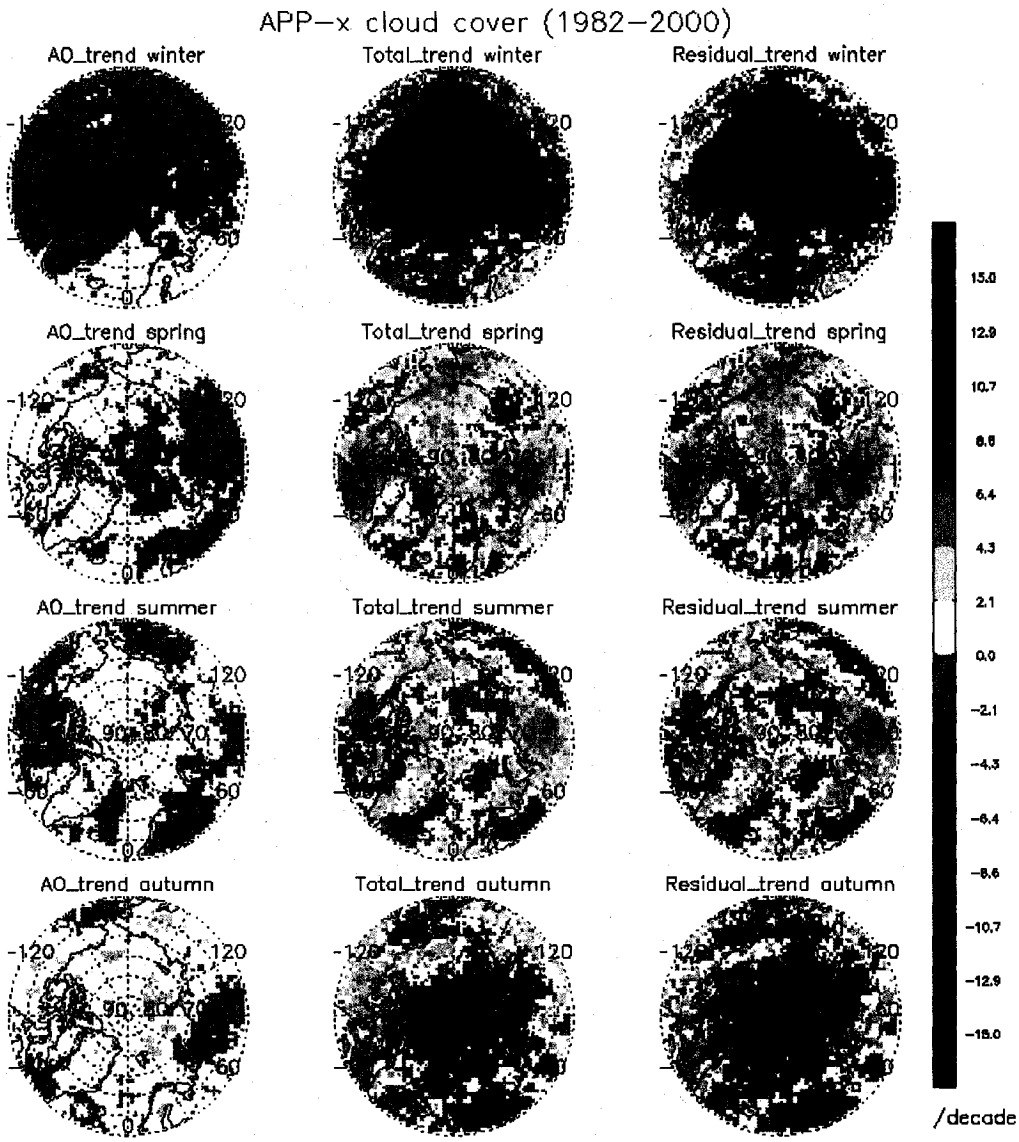


Fig. 3.11. The AO related trend (column 1), total trend (column 2), and residual trend (column 3) of cloud cover in four season from 1982 to 2000 from APP-x.

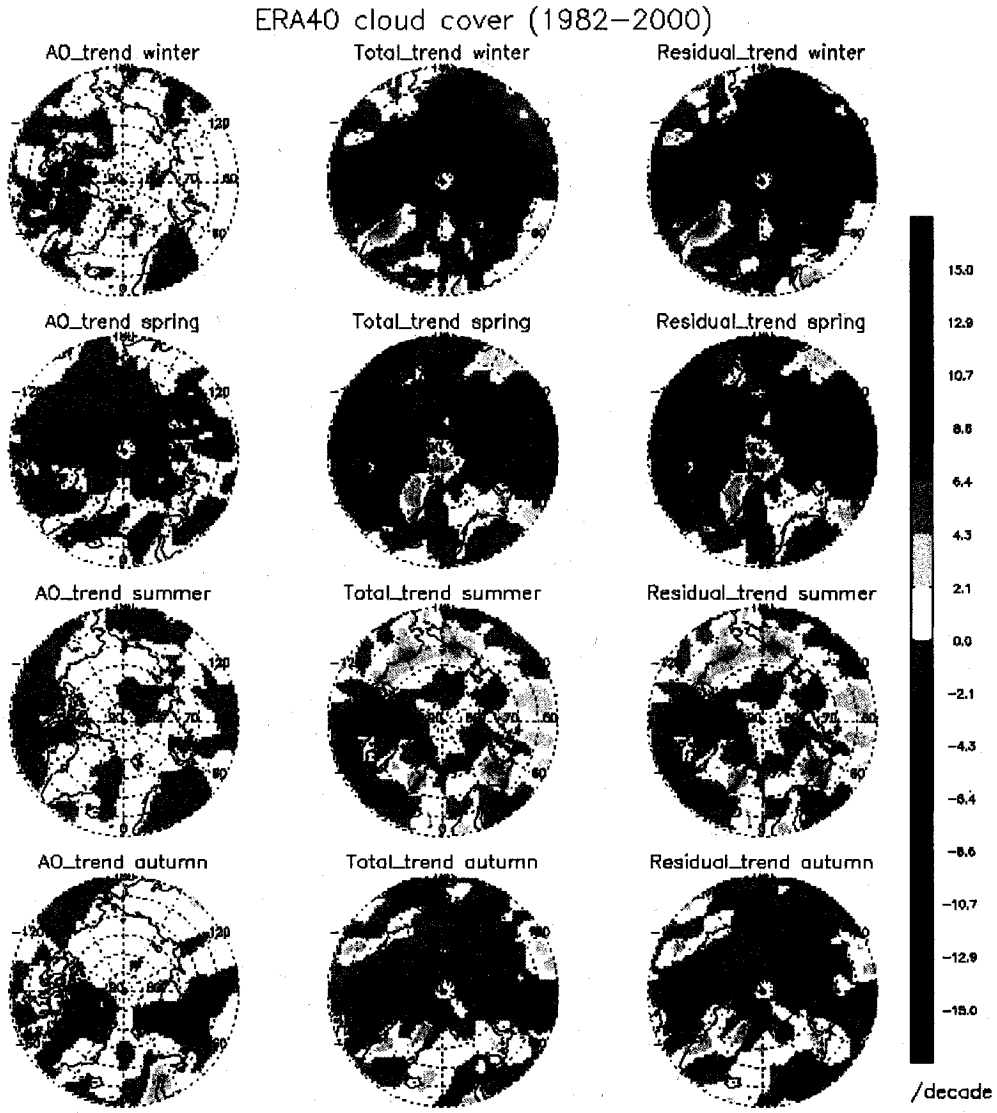


Fig. 3.12. The AO related trend (column 1), total trend (column 2), and residual trend (column 3) of total cloud cover in four seasons from 1982 to 2000 from ERA40.

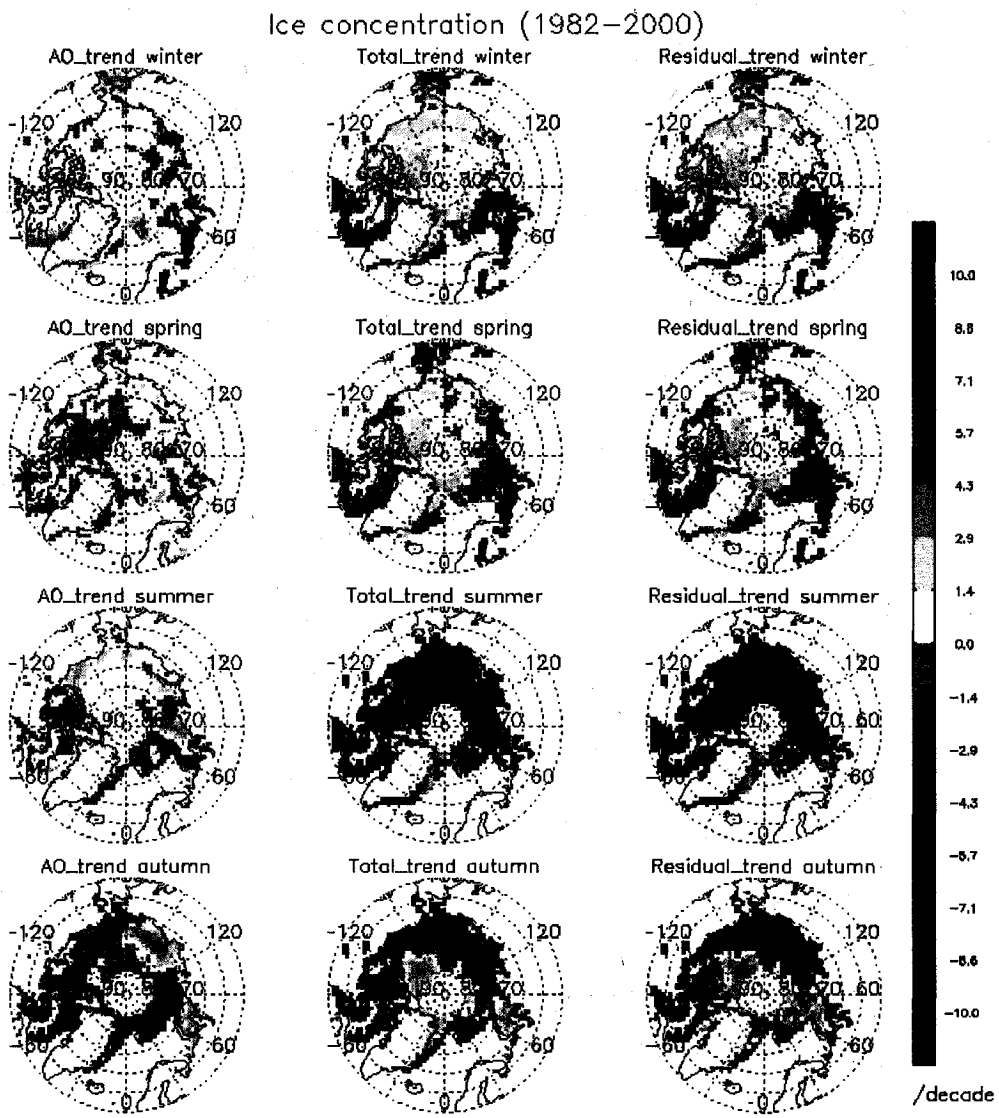


Fig. 3.13. The AO related trend (column 1), total trend (column 2), and residual trend (column 3) of sea ice concentration in four seasons from 1982 to 2000 from microwave data.

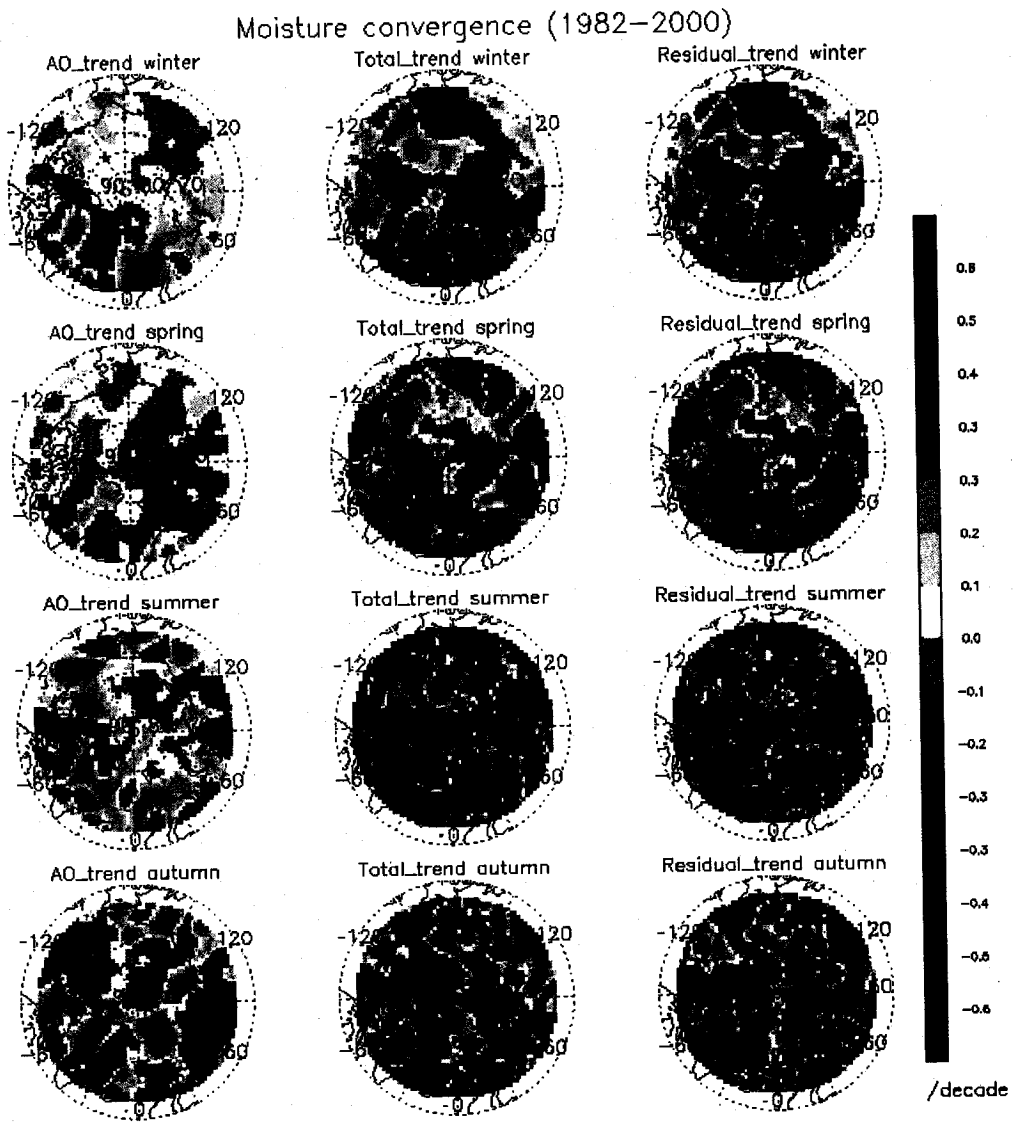


Fig. 3.14. The AO related trend (column 1), total trend (column 2), and residual trend (column 3) of moisture convergence in four seasons from 1982 to 2000 from TOVS Path-P.

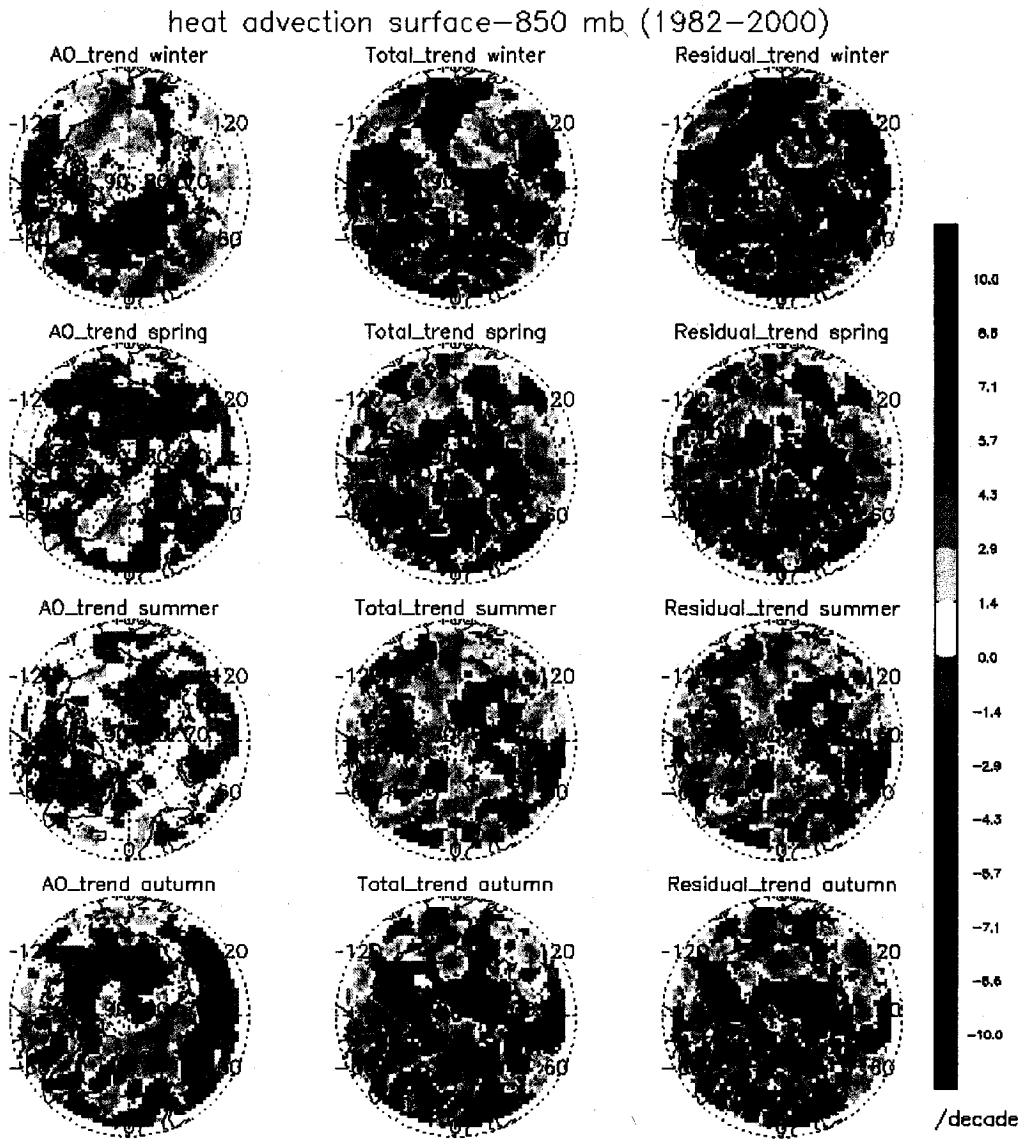


Fig. 3.15. The AO related trend (column 1), total trend (column 2), and residual trend (column 3) of heat convergence in four seasons from 1982 to 2000 from TOVS Path-P.

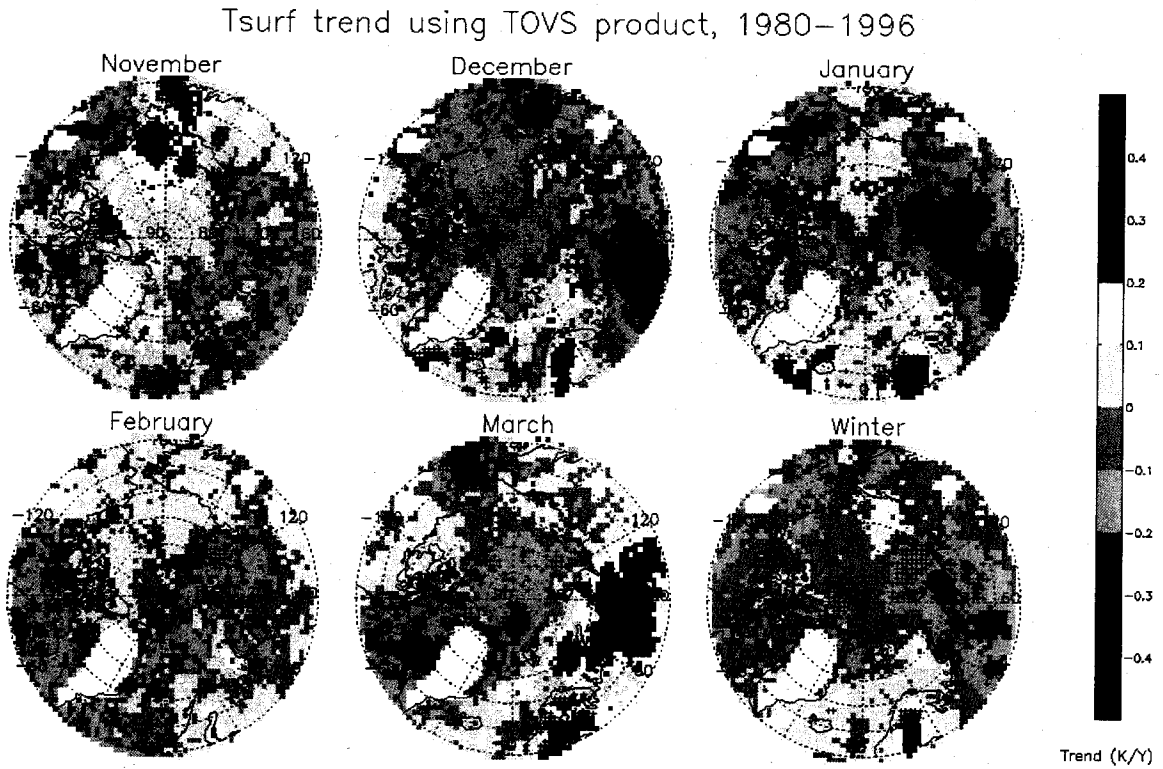


Fig. 3.16. Monthly trend of surface skin temperature (K/year) in November, December, January, February, March, and winter (DJF), 1980 to 1996, from the TOVS-derived surface temperature. A trend with a confidence level larger than 90% based on the F test is indicated with +.

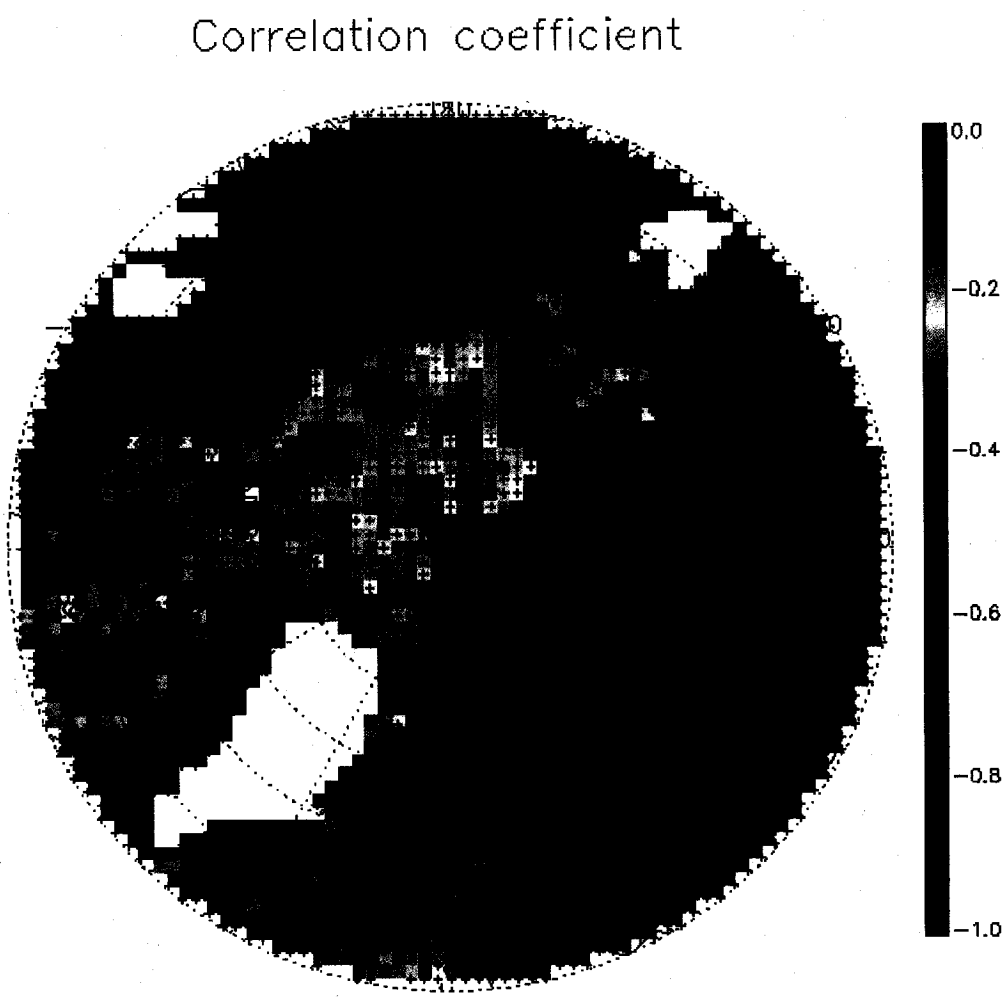


Fig. 3.17. Correlation coefficient between the monthly mean surface skin temperature anomalies and the monthly mean 2-channel statistical inversion strength anomalies over the period 1980-1996. A correlation coefficient with a confidence level larger than 95% based on the F test is indicated with +.

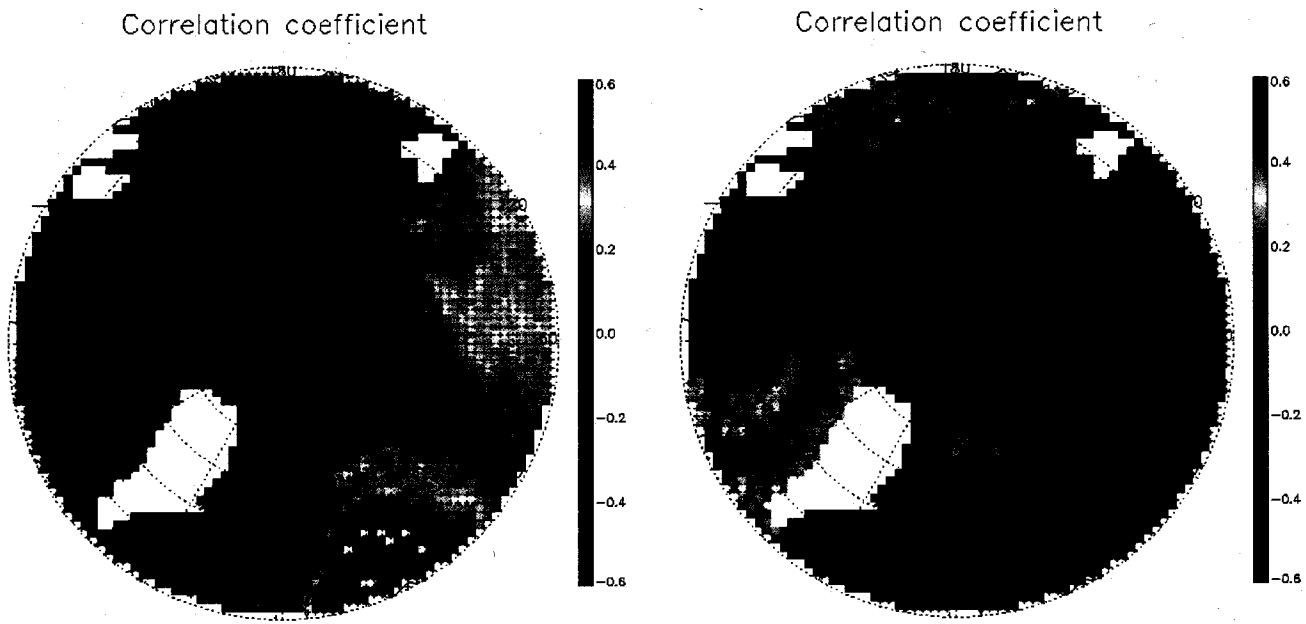


Fig. 3.18. Correlation between the monthly AO index anomalies and the monthly mean surface skin temperature anomalies (left), and monthly mean 2-channel statistical inversion strength anomalies (right), 1980- 1996. A correlation coefficient with a confidence level larger than 95% based on the F test is indicated with +.

# 4 The Influences of Changes in Cloud Cover on Recent Surface Temperature Trends in the Arctic

A variety of recent studies have shown that the Arctic is expected to warm more than any other part of the earth in response to increasing concentrations of greenhouse gases, largely because of polar amplification due to feedback effects associated with the high albedo of snow and ice (cf., Manabe et al. 1992). Arctic surface temperatures are projected to rise at a rate about twice the global mean over the next century (Houghton et al. 2001). Surface temperature is an extremely important climate change variable, because it integrates changes in the surface energy budget and atmospheric circulation (Serreze et al. 2000).

Due to the paucity of conventional observations in the Arctic, especially over the Arctic Ocean, an evaluation of trends in surface temperature is challenging. Perhaps the most comprehensive study analyzed the seasonal mean and trends of surface air temperature based on observations from buoys, manned drifting stations, and land meteorological stations, with interpolation to fill gaps, in the Arctic from 1979 to 1997 (Rigor et al. 2000). The dataset is a part of the International Arctic Buoy Programme/Polar Exchange at the Sea Surface (IABP/POLES). The limitations of their work include the relatively small amount observations over Arctic Ocean and poor quality of the buoy data especially before 1992. Satellite data provides an opportunity to investigate the surface temperature over the entire Arctic region by its high temporal and spatial resolution cover over high latitudes. Chen et al. (2002) derived surface

temperatures from the Television and Infrared Observations Satellite Operational Vertical Sounder Polar Pathfinder (TOVS Path-P) dataset, and compared the decadal temperature trends calculated from TOVS and the POLES data set. They found large discrepancies in the decadal temperature trends over the central Arctic Ocean in spring. Comiso (2003) studied the seasonal trend of surface temperature during cloud-free conditions based on satellite thermal infrared data from the Advanced Very High Resolution Radiometer, a five-channel imager on board NOAA polar orbiting satellites. He found the trends in the cloud-free surface temperature are mainly positive in summer, spring, and autumn; the trends are generally negative in winter, with some cooling observed in large areas in the Bering Sea and parts of Russia. Wang and Key (2003, 2005a, 2005b) investigated the spatial and temporal characteristics and recent trends of Arctic surface, cloud, and radiation properties in the Arctic from 1982 to 1999 based on the extended AVHRR Polar Pathfinder (APP-x) product. For the all-sky (clear and cloudy) surface temperature, they found a cooling trend in winter over the central and eastern Arctic Ocean, and mainly warming trends in spring, summer and autumn. Over the central and eastern Arctic Ocean, there was also a significant decreasing trend in cloud cover in winter.

In order to understand the Arctic climate system we must first understand cloud processes, including their interaction with atmospheric dynamics and their influence on the surface (Curry et al. 1996). Polar cloudiness is expected to change considerably if decreasing sea ice cover creates larger areas of open water, and the varying atmospheric circulation changes the moisture advection into Arctic (Groves and Francis 2002a, 2002b). There are significant surface temperature differences under cloudy and clear

conditions, with the observed difference of 8-10 K during October-February and 5-6 K during March-May and September (Walsh and Chapman, 1998), so it is likely that trends in the all-sky surface temperature are strongly dependent upon trends in cloud cover.

Previous studies either focused on cloud-free surface temperature trends, or on trends under all-sky conditions. In this study, satellite-derived Arctic surface temperature trends under cloudy, clear, and all-sky conditions are presented, and the effect of the cloud cover changes on the surface temperature trend is evaluated.

## 4.1 Data

Data shown in Table 2.1 is used in this study. Furthermore, Monthly means of surface temperature under cloud-free, cloudy conditions are calculated from the daily data. At least 10 daily values in a month are required in the calculation of the monthly means. Due to the high cloud cover in the Arctic, the daily cloud-free and cloudy data are sub-sampled to a 100 km grid by average to meet this requirement. In this paper, only the results at 1400 LST are presented. Conclusions based on 0400 LST and 1400 LST data are similar.

The seasonal mean is calculated based on the monthly mean data. The seasonal trends of each parameter are derived based on the seasonal means. Trend analysis were performed using least square fit regression, where the trend value is the slope of the regression line. For each trend, an F-test value of significance is computed.

## 4.2 Surface Temperature Trends

### 4.2.1 All-sky Surface Temperature Trends

The seasonal trends of all-sky surface temperature based on APP-x dataset from 1982 to 2004 are calculated on a pixel-by-pixel basis and the results are presented in Figure 4.1a. In winter, the surface temperature increases over northern Canada, with the maximum magnitude over Hudson Bay. The surface temperature decreases over the Arctic Ocean and the eastern Arctic. Over the central Arctic Ocean, the decreasing trend is approximately -2.5 K/decade. This cooling trend is consistent with the positive sea ice extent trend over the Arctic Ocean and Bering Sea in the same season (Parkinson et al. 1999). In spring, significant warming is seen over most of Arctic, including the central Arctic Ocean, most of northern Canada and Alaska, and north central Russia. The maximum increasing trend is around 2.0 K/decade over land and over Chukchi and Beaufort Seas. In summer, the surface temperature is generally increasing, with a smaller magnitude than those in spring. The strong increasing trend can be seen over northeastern Russia, Alaska and northern Canada with the maximum trend around 1.5 K/decade. Over the central Arctic Ocean and north central Russia, the trends are near 0. In autumn, there are strong increasing surface temperature trends over Beaufort Sea, Chukchi Sea, Alaska, and northern Canada, with the maximum trend around 2.0 K/decade. This warming trend is closely related to the sea ice cover retreat in the 1990s (McPhee et al. 1998; Comiso 2001). The trend over most of the Arctic Ocean is negative, with the magnitude around -0.5 K/decade. In four seasons, the surface temperature trends over northern Europe are

positive, with the strongest increasing in spring of 2.0 K/decade. The trends based on the APP-x all-sky surface temperature at 04:00 LST are similar (not shown).

The all-sky surface temperature trends from the App-x dataset in four seasons are compared with the surface air temperature trends from ERA-40 reanalysis grid-by-grid, after the APP-x trends are sampled to the ERA-40 grid. It should be noted that AVHRR data were not assimilated in the ERA-40 reanalysis. The APP-x trends are calculated based on the APP-x all-sky surface skin temperature at 1400 LST; the ERA-40 trends are calculated based on the monthly mean of all four daily times of surface air temperature. The trends from 1982 to 2001 are calculated instead of 1982 to 2004, as ERA-40 ends at August 2002. Overall there is good agreement between APP-x surface skin temperature trends and ERA-40 surface air temperature trend in four seasons, as shown in Figure 4.2. The average biases between them in winter, spring, summer, and autumn are –0.40, -0.05, 0.13 and –0.31 K/decade; the RMS difference are 0.80, 0.63, 0.50 and 0.65 K/decade; and the correlation coefficients between these two trends in four seasons are 0.60, 0.56, 0.43 and 0.53 respectively.

Time series of seasonal anomalies of the APP-x surface skin temperature and the ERA-40 surface air temperature over selected regions (Region 1: Arctic basin (Groves and Francis 2002a); Region 2: northern Europe; Region 3: north central Russia; Region 4: northeastern Russia; Region 5: Alaska; Region 6: northern Canada;) are shown in Figure 4.3. Due to a gap in AVHRR data during the 1995 winter, the data is the interpolated between the 1994 and 1996 winters. These two anomalies show good agreement.

### 4.2.2 Clear-sky and Cloudy-sky Surface Temperature Trends

Surface temperature trends from 1982 to 2004 under cloud-free and cloudy conditions in four seasons based on APP-x dataset are calculated in same way as the all-sky trends. They are shown in Figures 4.1b and 4.1c. The cloudy sky surface temperature trends could be a result of changes in cloud properties, atmospheric circulation and heat advection, and/or sea ice cover. The clear-sky surface temperature trends might result from the changes in the atmospheric circulation, heat advection, and/or sea ice cover. The cloud-free and cloudy surface temperature trends exhibit similar patterns as the all-sky trends shown in Figure 4.1a.

However, for the regions where both clear and cloudy trends are positive, including most of North America in winter, the Chukchi and Beaufort Seas in spring, the central Arctic Ocean in summer, and most of North America, the Chukchi and Beaufort Seas in autumn, the magnitude of the warming trends under cloud-free conditions is larger than under cloudy conditions. For the regions where both trends are negative, including the eastern Arctic Ocean and north central Russia in winter, and part of northeastern Russia in spring, the magnitude of both trends are comparable. Under cloudy conditions, the trends are not as dramatic as under cloud-free conditions, which again implies that clouds have a negative feedback on the surface temperature trends, as pointed out by Wang and Key (2003).

## 4.3 The Influence of Clouds on All-sky Temperature Trends

Over the Arctic, especially over Arctic Ocean, clouds radiatively warm the surface at all times of the year except during a portion of the summer (Curry et al. 1993; Schweiger and Key 1994; Walsh and Chapman 1998; Intrieri et al., 2002). As a result, the difference between the cloudy and the cloud-free seasonal mean surface temperature is 8-10 K during October-February, and 5-6 K during March-May and September over sea ice based on in situ observations (Walsh and Chapman, 1998). Therefore, if the surface temperature under cloud-free and cloudy conditions remains constant (but different from each other), and cloud cover changes over the years, the all-sky surface temperature observed from satellite will, of course, change. Can we quantify the influence of cloud cover trends on the all-sky surface temperature trend?

### 4.3.1 Partition of All-sky Surface Temperature Trends

The clear and cloudy surface temperature and cloud cover are assumed to change linearly over a time period of Z years, e.g., from 1982 to 2004. The surface temperature retrieval with satellite data is assumed to have biases $\Delta_{clr}$ for cloud-free and $\Delta_{cld}$ for cloudy conditions; these biases do not change over time. At the beginning of the time period, the cloud-free surface temperature is $T_{clr,1}+\Delta_{clr}$, where $T_{clr,1}$ is the unbiased real cloud-free surface temperature. Similarly, the cloudy surface temperature is $T_{cld,1}+\Delta_{cld}$, where $T_{cld,1}$ is the unbiased real cloudy surface temperature; the cloud cover is $C_1$. All three parameters change linearly with time. At the end of the Z years, the cloud-free

surface temperature is $T_{clr,2}+\Delta_{clr}$; the cloudy surface temperature is $T_{cld,2}+\Delta_{cld}$; and the cloud cover is $C_2$. The trends of the cloud-free surface temperature, cloudy surface temperature, and cloud cover are $S_{clr}$, $S_{cld}$, and $S_c$, respectively. The means of the cloud-free surface temperature, the cloudy surface temperature, and cloud cover over this time period are $T_{clr}$, $T_{cld}$, and C, respectively. The relationships between these variables are:

$$T_{clr,2} + \Delta_{clr} = T_{clr,1} + \Delta_{clr} + S_{clr} Z$$
$$T_{cld,2} + \Delta_{cld} = T_{cld,1} + \Delta_{cld} + S_{cld} Z$$
$$C_2 = C_1 + S_c Z$$
$$T_{clr} = (T_{clr,1} + T_{clr,2})/2 + \Delta_{clr} = T_{clr,real} + \Delta_{clr}$$
$$T_{cld} = (T_{cld,1} + T_{cld,2})/2 + \Delta_{cld} = T_{cld,real} + \Delta_{cld}$$
$$C = (C_1 + C_2)/2$$

where $T_{clr,real}$ and $T_{cld,real}$ are the real (true) mean of the cloud-free and cloudy surface temperature without retrieval biases. In the following sections, the seasonal means of the cloud-free surface temperature, the cloudy surface temperature, and cloud cover are calculated as the mean of all the individual seasonal means, not the average of the seasonal mean in the first and last year. Then the all-sky surface temperature at the beginning and end of the time series, and the trend are:

$$T_{all,1} = (T_{clr,1} + \Delta_{clr})(1 - C_1) + (T_{cld,1} + \Delta_{cld})C_1$$
$$T_{all,2} = (T_{clr,2} + \Delta_{clr})(1 - C_2) + (T_{cld,2} + \Delta_{cld})C_2$$
$$S_{all} = (T_{all,2} - T_{all,1})/Z$$

It can be proven that:

$$S_{all} = [S_{clr}(1-C) + S_{cld}C] + (T_{cld} - T_{clr})S_c \quad (1)$$

$$S_{all} = [S_{clr}(1-C) + S_{cld}C] + (T_{cld,real} - T_{clr,real})S_c + (\Delta_{cld} - \Delta_{clr})S_c \quad (2)$$

In equation (1), the first component of $S_{all}$ in brackets is the combination of the cloud-free surface temperature trend weighted by the cloud-free area fraction and the cloudy surface temperature trend weighted by the cloud cover, which we call trend A for convenience hereinafter. The second term on the right represents the trend caused by cloud cover changes, which we call trend B. The surface temperature retrieval biases also have an effect on the all-sky trend, which is indicated as an expanded form of trend B in equation (2). This is a "false" trend that should be removed from the real trend.

Figure 4.4 shows the seasonal mean of the APP-x surface temperature difference under cloudy and cloud-free conditions. For most regions in the Arctic in winter, spring, autumn, and over Arctic Ocean in summer, the cloudy surface temperature is higher than that under cloud-free conditions because of the cloud radiative warming effect. The difference over Arctic Ocean is around 8 K in winter and in spring, 3 K in summer, and 6 K in autumn, which is consistent with the observed value over Arctic Ocean reported by Walsh and Chapman (1998). Figure 4.1d shows the seasonal trend of APP-x cloud cover from 1982 to 2004. Over most regions in winter and autumn, the cloud cover decreases, especially over the Arctic Ocean in winter. Over most regions in spring, the cloud cover increases. In summer the cloud cover does not change significantly. These differences in surface temperature coupled with cloud cover trends produce the trend B portion of the

total trend. According to equation (1), a negative trend B can be expected in winter and autumn, and a positive trend B can be expected in spring over Arctic Ocean.

### 4.3.2 Two Components of the Total Trends

Figure 4.5 shows trend A (Figure 4.5a) and trend B (Figure 4.5b) based on the APP-x data set from 1982 to 2004. Trend A is calculated as the first term in equation (1) using the data shown in Figure 4.1a and 4.1b and seasonal mean cloud cover. Trend B is calculated as the second term in equation (1) using data shown in Figure 4.4 and Figure 4.1d. In winter, trend A has similar pattern as the all-sky trend, which has an increasing trend in the western Arctic and a cooling trend over the eastern Arctic and most of the Arctic Ocean. Trend B is negative over most Arctic Ocean, with a magnitude from –0.4 K/decade to -1.5 K/decade. This trend arises from the higher surface temperature under cloudy conditions, and the significant cloud cover decrease over the Arctic Ocean in winter. For regions over the Arctic Ocean with cooling total trends, trend B is -0.5 K/decade lower than trend A, which means the trend B contributes more than trend A to the total cooling over the eastern Arctic Ocean. The warming trend over the western Arctic Ocean could be higher if trend B were not decreasing.

In spring, trend A has a similar pattern to the all-sky trend, which shows warming over most regions in the Arctic,. The trend B is positive over the Arctic Ocean, with a magnitude around 0.5 K/decade. This trend originates from the warmer surface temperature under cloudy conditions, and increasing cloud cover over the Arctic Ocean in spring. Trend B is smaller over the Chukchi and Beaufort Seas, and larger around the

North Pole than that of the real trend, and the pattern of trend A dominates the all-sky trend pattern over land in the spring. In summer and autumn, trend B is relatively smaller than in winter and spring, and trend A contributes most to the total trend. However, trend B around North Pole in autumn is as high as –0.7 K/decade.

### 4.3.3 Retrieval Bias on the Total Trends

In addition to cloud cover changes and the difference between cloudy and clear-sky surface temperatures, trend B is also a function of retrieval biases in the satellite-derived surface temperature. The relative importance of this trend in trend B depends on the ratio of the absolute magnitude of the difference between the clear and cloudy sky biases and the absolute magnitude of the real surface temperature difference under cloudy and clear-sky conditions. For the sake of illustration, the cloudy and clear-sky surface temperature differences based on APP-x are 8, 8, 3, and 6 K, respectively, in winter, spring, summer and autumn. If the bias difference is 2 K, the trend caused by bias difference will be 1/4, 1/4, 2/3, and 1/3 of trend B in winter, spring, summer and autumn. This impact of retrieval biases is small, but important. For example, in winter, the trend caused by bias difference over Central Arctic will be –0.3 K/decade.

## 4.4 Discussion and Conclusion

The all-sky surface temperature trends from 1982 to 2004 based on APP-x data set show warming trends over most regions in the Arctic spring and summer. In autumn, there is strong warming over the Beaufort Sea, the Chukchi Sea, Alaska, and northern

Canada, though a cooling trend is evident over northern Russia. In winter, the cooling trend is significant over the eastern Arctic and most Arctic Ocean, with a warming trend over the western Arctic. A comparison of the all-sky surface temperature trends from APP-x and ERA-40 from 1982 to 2001 shows good agreement.

The surface temperature trends under cloud-free and cloudy conditions are spatially similar to the all-sky trends, indicating that the clear and cloudy trends are similar in sign. But the absolute magnitude of the trend under cloud-free conditions is larger than that under cloudy conditions, which reflects the negative feedback of cloud on the surface temperature.

A method was presented to separate the effect of changes in cloud cover from the total surface temperature trend. The surface temperature trend is partitioned into two parts: the first part (trend A) is the linear combination of the surface temperature trends under cloud-free and cloudy conditions; the second part (trend B) is caused by the trend in cloud cover and the surface temperature difference under cloudy and clear-sky conditions. Trend B is significant in winter and spring over Arctic Ocean because of the significant cloud cover changes and cloudy/clear surface temperature differences. In winter, more than half of the decreasing surface temperature trend is from trend B over the central Arctic; i.e., the trend in cloud cover significantly affects the trend in the all-sky surface temperature. In spring, trend A contributes more than trend B to the total trend over land and over the Chukchi and Beaufort Seas. In the autumn and summer, trend A dominates, because cloud cover trends are small and/or the clear/cloudy sky temperature difference is small. The trend caused by a bias in the satellite retrieval of

surface temperature is a part of trend B, and it accounts for 1/4, 1/4, 2/3, and 1/3 of trend B in winter, spring, summer and autumn respectively, given a retrieval bias difference of 2 K between cloudy and clear-sky conditions.

The surface temperature trend will be non-zero if cloud cover changes significantly, even if the clear and cloudy-sky surface temperatures remain constant. Significant total cloud cover changes are found in different regions of the globe, e.g., 1.4% (of sky) per decade increasing total cloud cover in U.S. since the late 1970s (Dai et al. 2006) and -0.88% per decade decreasing total cloud cover in China since the 1950s (Qian et al. 2006). The influence of cloud cover changes on the total surface temperature trend in the U.S. and China can be around -0.1 K/decade and 0.06 K/decade under the assumption that the temperature difference under cloudy and clear conditions is -7 K in the mid-latitudes. In the context of an observed 0.31 K/decade Northern Hemisphere land-surface air temperature trend from 1976 to 2000 (Jones et al., 2001), this non-negligible trend needs to be considered in studying the regional total surface temperature trend, and its causes.

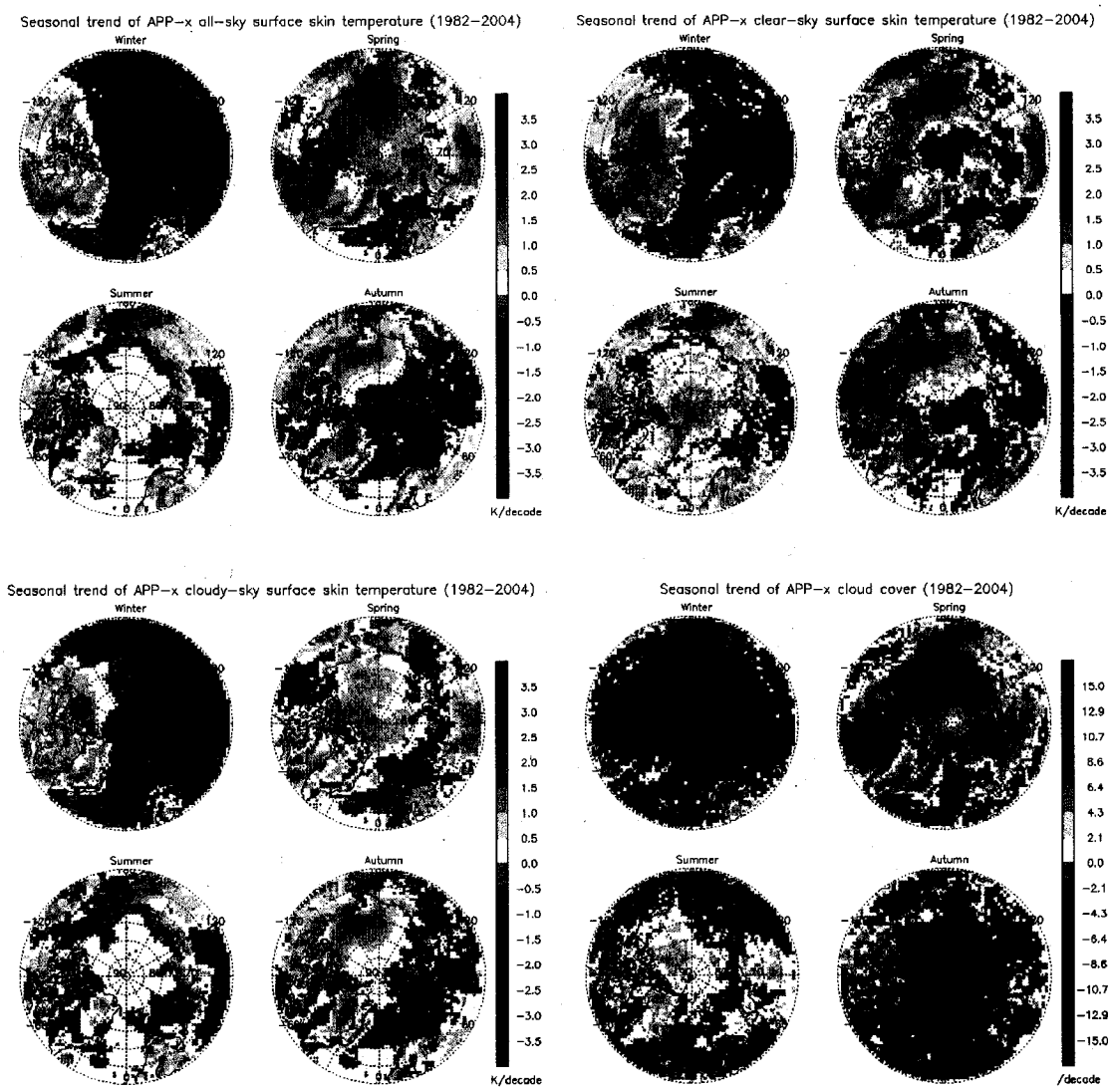


Fig. 4.1: Seasonal all-sky (Fig 4.1a, top left), clear-sky (Fig 4.1b, top right), cloudy-sky (Fig 4.1c, bottom left) surface temperature trends, and cloud cover trends (Fig 4.1d, bottom right) from 1982 to 2004 based on APP-x dataset. A trend with a confidence level larger than 95% based on the F test is indicated with +.

s

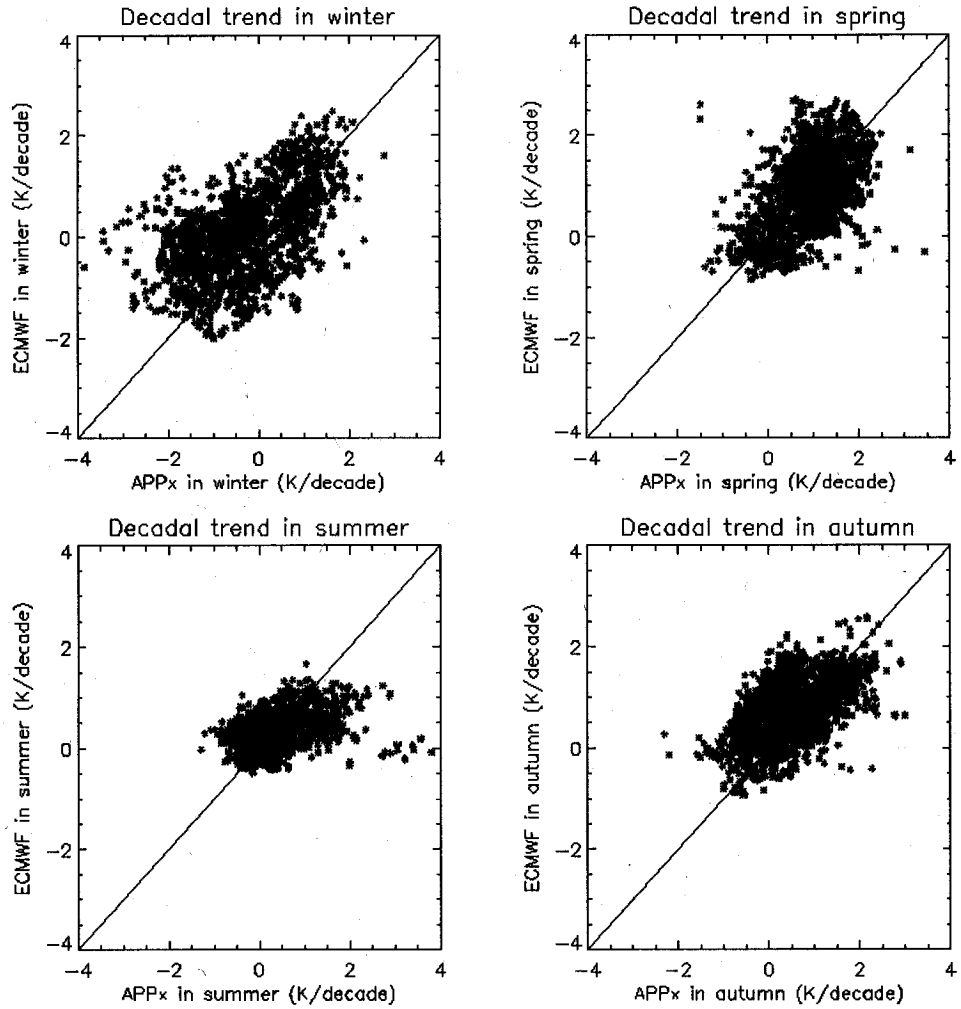


Fig. 4.2: The comparison between the seasonal trends from the APP-x data set and ERA-40 data set, 1982-2001.

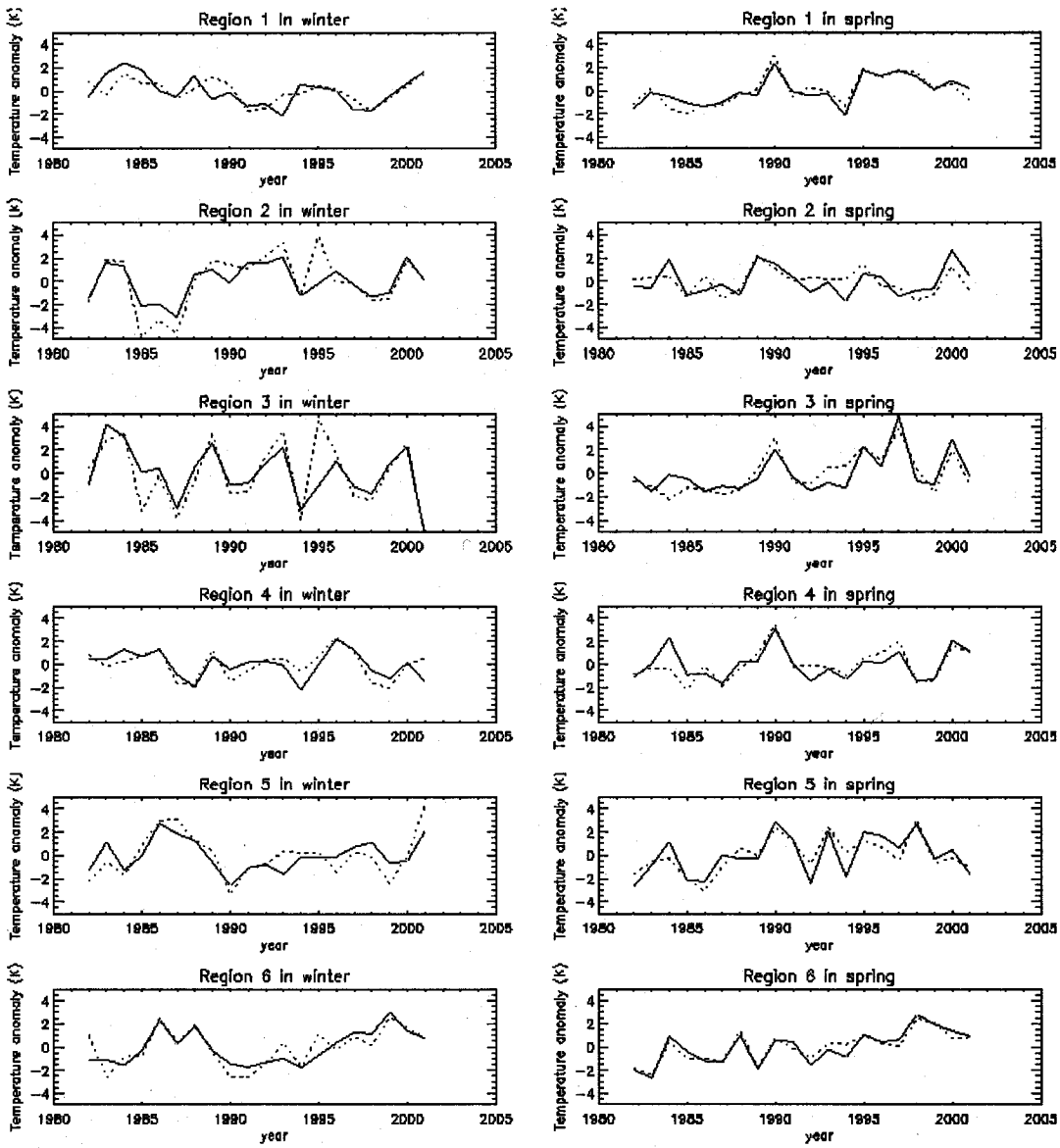


Fig. 4.3: Time series of regional means, seasonal APP-x surface skin temperature anomalies (solid line), and ERA-40 surface air temperature anomalies (dotted line) in winter and spring over selected regions.

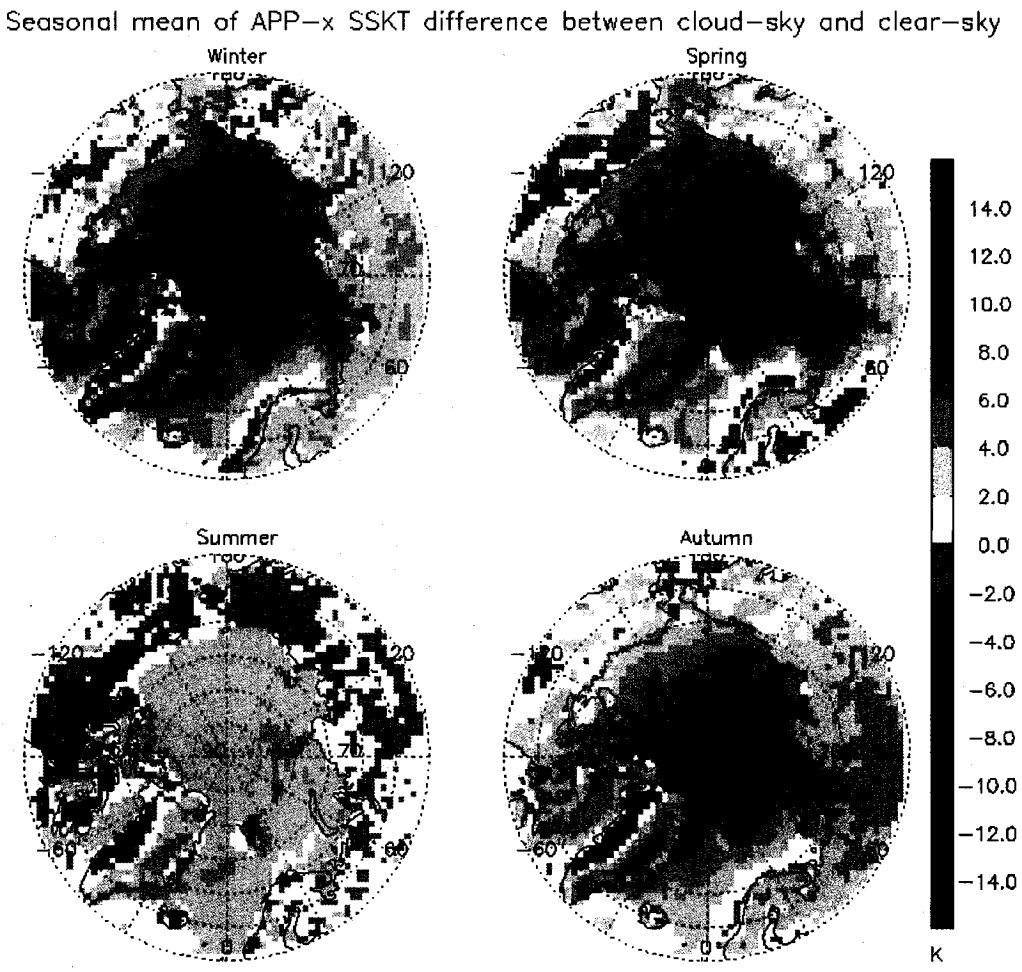


Fig. 4.4: The difference between the seasonal mean surface temperature under cloudy and cloud-free conditions based on the APP-x dataset.

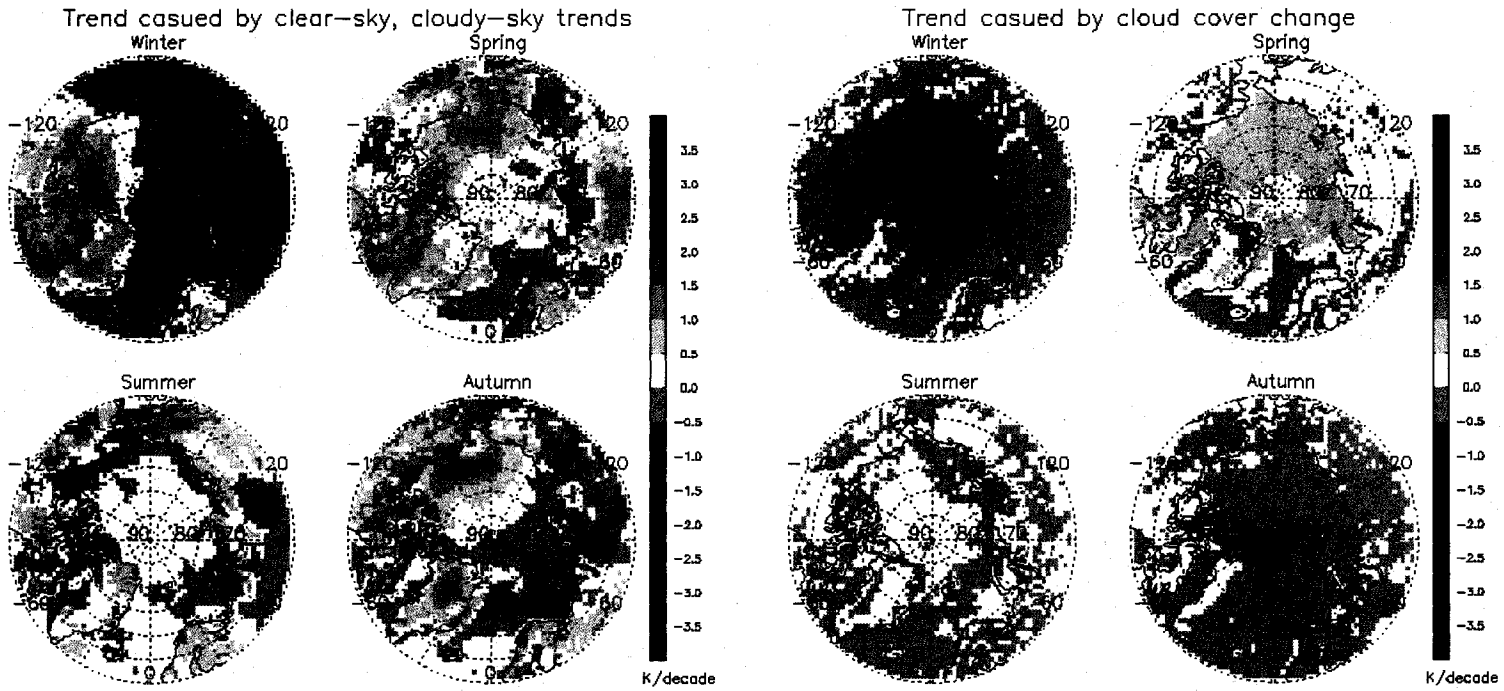


Fig. 4.5: The trend A (4a, left) and trend B (4b, right) components of the total all-sky surface temperature trend from 1982 to 2004 based on the APP-x dataset.

# 5 Possible Causes of Seasonal Cloud Cover Changes in the Arctic, 1982-2000

## 5.1 Possible Causes of Seasonal Cloud Cover Changes in the Arctic in winter, 1982-2000

The effect of clouds on radiation in the Arctic is complex owing to the high reflectivity of snow and ice, the absence of solar radiation for a large portion of the year, low temperatures and water vapor amounts, and ubiquitous temperature inversions (Curry et al. 1996). As an important component of the surface and atmospheric energy budget, radiation affects the surface and atmospheric temperature, and interacts with energy transport from lower latitude. The ability to understand and model clouds, radiation processes, and their relationship with atmospheric dynamics and the underlying boundary is extremely important for understanding the Arctic and global climate systems.

Wang and Key (2003,2005b) presented cloud fraction trends from 1982 to1999 over the area north of 60°N based on the extended Advanced Very High Resolution Radiometer (AVHRR) Pathfinder (APP-x) dataset. They found increasing trends in cloud fraction during spring and summer ( 3%/decade in spring and 1.5 %/decade in summer ), and associated these trends with increasing cyclonic activity. They also found a statistically significant decrease in cloud fraction over the central Arctic in autumn, and over most of the Arctic in winter (-5 %/decade in winter). During the same time period, Arctic cyclone frequency and intensity in winter increased (Serreze et al. 1997; Key and Chan 1999; McCabe et al. 2001; Zhang et al. 2004).

Cloud formation mechanisms in the Arctic are not well understood. Curry et al. (1996) stated that clouds in the marginal ice zone are frequently associated with frontal systems; the formation of mid- and upper-level clouds over the Arctic Ocean are closely associated with frontal systems and cyclone activities; and low-level clouds form when relatively warm, moist air is advected into the polar basin and cools radiatively (Herman and Goody 1976; Curry 1983). Beesley and Moritz (1999) examined three factors that control low cloud amount over the Arctic Ocean, including moisture flux convergence, surface evaporation, and microphysical processes related to atmospheric ice. They further suggested that temperature-dependent ice-phase processes are essential in low cloud formation based on model simulations.

In this study the decreasing cloud cover trend over the Arctic Ocean in winter from 1982 to 2000 is examined, and a possible cause for this trend is proposed. Possible cloud formation mechanisms over the Arctic Ocean in winter are also investigated.

### 5.1.1 Data

Data shown in Table 2.1 is used in this study. Daily cloud cover in the cold season from the APP-x is also used in this study. For the APP-x dataset, only the results at 1400 LST are presented. Conclusions based on 0400 LST and 1400 LST data are similar.

Seasonal means of each parameter in winter (December, January, February) are calculated based on the monthly means, seasonal trend from 1982 to 2000 of each parameter is derived based on the seasonal means. Trend analysis is performed using

least square fit regression, where the trend value is the slope of the regression line. For each trend, an F-test value of significance is computed.

### 5.1.2 Trends in Cloud Cover and Moisture Convergence in winter

Wang and Key (2003, 2005b) reported decreasing cloud amount over the Arctic in winter from 1982 to 1999. In this study, the APP-x data set is extended to including data in 2000; the winter cloud trend including 2000 data is presented in Figure 5.1a. Significant decreasing cloud cover is apparent over most of the Arctic Ocean, with a maximum decadal trend of approximately –12% over most of the eastern portion. Cloud cover over land does not change significantly. Based on cloud cover retrievals in TOVS Path-P, Schweiger (2004) also reported significant decreasing cloud cover over the winter Arctic Ocean from 1982 to 2001. Comiso (2003) found a decreasing cloud cover over sea ice areas (ice concentrations > 80%) based on AVHRR data using a different retrieval algorithm. The winter cloud cover trend from 1982 to 2000 in the ERA-40 reanalysis (Figure 5.1b) shows generally negative trends over the Arctic Ocean. Negative trends in surface skin temperature over the Arctic Ocean in winter (Wang and Key 2005b, Comiso 2003), and 2-m air temperature in winter from ERA-40 are also evident. This corroboration among trends in cloud cover from different satellite sensors and algorithms, as well as the ERA-40 reanalysis, provide further confidence in the decreasing winter cloud cover over the Arctic Ocean observed in the APP-x product.

The seasonal trend of moisture convergence in the Arctic winter from 1982 to 1998 is shown in Figure 5.1c. Over the Arctic Ocean, significant positive trends exist over the

Beaufort Sea, eastern Greenland-Iceland-Norwegian (GIN) Seas, and the western Barents Sea. Significant negative trends are observed over the Bering Strait, the Nansen Basin, and part of the Barents and Kara Seas (75-90°N, and 45-90°E; hereafter the "NBK region").

Groves and Francis (2002b) calculated mean net precipitation, which is the difference between the moisture convergence and the tendency of the vertically integrated precipitable water. They showed the decadal difference during the cold season (November-May) between the period from 1989 to 1998, and from 1980 to 1988 (Figure 14 of their paper). The trend patterns of the moisture convergence are consistent with the decadal difference patterns of the net precipitation.

### 5.1.3 Possible cause of decreasing cloud cover over NBK region

Winds transport moisture from low to high latitudes, where some of the moisture condenses to form clouds. Decreasing Arctic cloud cover in winter may be associated with changes in moisture convergence. To investigate this possibility, monthly mean APP-x cloud cover and moisture convergence in the cold season (November-March) from 1982 to 1998 are first converted to monthly anomalies by subtracting mean monthly values for each individual month, then the anomalies are detrended. Finally correlation coefficients between monthly anomalies in the cloud cover and the moisture convergence are calculated (Figure 5.2). Statistical significance is determined with a student-t test. Relatively higher positive correlations occur over northeastern Russia/Bering Strait and over the NBK region, where negative trends in both moisture convergence and cloud

cover occur. Time series of the monthly anomalies of cloud cover and moisture convergence averaged over the NBK region in the cold season (Figure 5.3) are predominantly in phase, with a correlation coefficient of 0.43 and confidence level of 99.9%. This suggests a corresondence between changes in cloud cover and moisture convergence over this region. Note that cloud cover anomalies decreased substantially in 1988, although no inter-satellite bias is observed. (Do we need this sentence? Or we can comment on this if reviewers ask?)

Negative trends in moisture convergence and cloud cover over the NBK region may result from weaker cyclonic activity in the area. Cyclone frequency and intensity in the Arctic overall increased from 1982 to 2000 (Zhang et al. 2004; McCabe et al. 2000). But, changes may vary over different regions. Serreze et al. (1997) found opposite tendencies in cyclone activity over the Barents and Kara Seas under the positive mode of the North Atlantic Oscillation (NAO) from 1966 to 1993. The NAO index during winter has changed to a predominantly positive mode since about 1970, suggesting a decrease in cyclonic activity over the NBK region during 1982 to 2000. Zhang et al. (2004) showed that Arctic cyclone activity increased during the second half of the twentieth century, but this is associated with decreased cyclone center counts over the NBK region (Figure 13c of their paper).

Weaker cyclone activity over the NBK region may be related to trends in sea level pressure and wind, as shown in Figure 5.1d. Sea level pressure decreased over most of the Arctic Ocean, which is consistent with increasing cyclone activity in the Arctic. The magnitude of this decrease varies spatially, however. Between Scandinavia and Svalbard

trends are over -2 hPa/decade, while around the North Pole are -1.6 hPa/decade. These are larger than that over the NBK region (-1.2 hPa/decade), which results in an anticyclone-like pattern in the wind-field trends over the NBK region. This anticyclonic pattern may be associated with the weakened cyclone activity and decreased moisture convergence, which lead to reduced cloud cover over the NBK region.

### 5.1.4 Possible cause of decreased cloud cover over the central Arctic Ocean

APP-x cloud cover trends in Figure 5.1a show significant decreasing trends over most of the Arctic Ocean from 1982 to 2000. Though the negative cloud cover trend associated with decreased moisture convergence over the NBK region may be attributed to weaker cyclone activity, decreased cloud cover over other regions in the Arctic Ocean is still unexplained. Furthermore, trends in moisture convergence over the Beaufort Sea and Canada Basin are significantly positive while the cyclone activity over the Arctic Ocean does not appear to have declined except in the NBK region.

Serreze and Barry (1988) found that cyclones from the North Atlantic and the Barents Sea coastline merge near 75-90°N, 30-90E, then track eastward to northeastward. This raises the possibility that if less cloud cover over the NBK region is related to the decreased cloud cover over other regions in the Arctic Ocean, cloud cover decline over the NBK region may result in decreased cloud cover elsewhere in the Arctic Ocean regions by advection. To investigate this possibility, an index is created from averaged monthly anomalies in cloud cover over the NBK region for each month. Monthly anomalies of cloud cover at each grid point in the Arctic are then spatially correlated with

that index during the cold season from 1982 to 2000 (Figure 5.4). High positive correlation values exist over most of the Arctic Ocean, with larger values in the eastern versus western Arctic. This pattern suggests that cloud cover anomalies over most of the Arctic Ocean are in phase.

Cloud cover anomalies over other regions in the Arctic Ocean might also be affected by cloud cover anomalies over the NBK region, and reduced cloud cover over other regions in the Arctic Ocean might originate from the decreased cloud cover over the NBK region. To examine this possibility, the Arctic Ocean is divided into five areas, each 45 degrees of longitude (from 45°E to 270°E), sequentially eastward around the Arctic. These are designated regions 1 to 5 (1 NBK region, 2 Laptev Sea, 3 East Siberian Sea, 4 Chukchi/Beaufort Seas, 5 Canada Basin). These five areas exhibit significant decreased cloud cover. From November to the following March, daily APP-x cloud cover over each of these five regions is averaged; daily anomalies are calculated by subtracting 30-day means; and correlation coefficients between the daily anomalies over the NBK region and over other four regions are calculated, with the NBK region leading other regions by 0 to 7 days. Correlation coefficients and their significance for November 1995 to March 1996, for example, are presented in Table 5.1. Correlation coefficients within the NBK region itself decrease with time; values between the NBK region and the Laptev Sea are highest within 2 days with confidence > 95%, after which it decreases. Values between the NBK region, the East Siberian Sea, and the Chukchi/Beaufort Seas are small within a 2-day lag, then become larger and statistically significant later, with maxima at 3- and 4-day lags. Correlations between the NBK regions and the Canada Basin are largest at 5- and 6-

day lags. The cloud cover anomalies over the NBK region appear to be advected to the Laptev Sea, the East Siberian Sea, the Chukchi/Beaufort Seas and the Canada Basin successively. In Figure 5.1.d, the wind trend shows a clear increased flow from NBK eastward to the other four areas, which supports the notion that the cloud anomalies in NBK are advected to the other areas. Correlation coefficients for the Canada Basin leading the Chukchi/Beaufort Seas and then NBK, however, do not exhibit this pattern.

### 5.1.5 Discussion

Over the NBK region, the observed decrease in cloud cover appears to be associated with reduced moisture convergence owing to weaker cyclone activity. Decreased cloud cover over other regions in the Arctic Ocean seems to follow a reduction in cloud cover over the NBK region. It is possible that this relationship also exists in the Pacific side of the Arctic. Associated with less moisture convergence over northeastern Russia and the Bering Strait, cloud cover over that region (65-75°N, 150-200°E) [which?] decreases, and less cloud is advected into the central Arctic Ocean. Correlation coefficients between monthly anomalies in the cloud cover and the moisture convergence is 0.28 over the region bounded by 65-75°N, 150-200°E, which is smaller than that over the NBK region. Cloud cover anomalies over the East Siberian Sea appear to affect cloud cover over the Chukchi/Beaufort Seas and the Canada Basin, similar to the way the NBK region affects other four regions Serreze and Barry (1988) found that cyclones from the North Atlantic and the Barents Sea rarely penetrate into the western Arctic. So, reduced cloud cover over

region the region within 65-75°N, 150-200°E might have a stronger influence on the Chukchi/Beaufort Seas and the Canada Basin.

Other than moisture convergence, changes in surface evaporation could also influence cloud amount. Herman and Goody (1976) argued, however, that surface evaporation is small or negative during winter months and strong surface-based inversions suppress upward mixing. Seasonal mean surface evaporation in winter over the NBK region from ERA-40 is much smaller than the moisture convergence, and there is no significant trend of winter surface evaporation over the Arctic Ocean from 1982 to 2000, thus this appears to be an unlikely explanation for observed cloud change in this region.

Beesley and Moritz (1999) suggest that the temperature dependence of ice-phase microphysical processes is an essential factor in explaining the annual cycle of low cloud amount in the Arctic. If more ice particles exist in the cloud, cloud cover would decrease owing to the quicker dissipation of the cloud, which comes from the quicker falling out of the ice particles. Trends in cloud phase derived from the APP-x product, which senses mainly cloud-top particles, suggest the percentage of ice cloud has increased over most of the central Arctic Ocean. While these trends are statistically significant only over the Nansen Basin, they are consistent with the decreased cloud cover, as suggested by Beesley and Moritz (1999). If less cloud is advected into the central Arctic Ocean, then more ice cloud even decrease the cloud cover more by quicker falling out of the ice particles

## 5.2 Possible Causes of Seasonal Cloud Cover Changes in the Arctic in spring, summer, and autumn, 1982-2000

Cloud cover in spring and summer generally increases in the Arctic from 1982 to 2000. In autumn, cloud cover increases over the Beaufort and Chukchi Seas, the northern Canada, and the northeastern Russia; decreases over the Arctic Ocean. Trends in the cloud cover in spring, summer, and autumn are related to the trends in the cyclone activities and surface evaporation.

Correlation coefficients between monthly anomalies in the APP-x cloud cover and TOVS Path-P moisture convergence in four seasons from 1982 to 1998 are calculated and shown in Figure 5.5. A student-t statistical confidence level is calculated for each correlation coefficient and shown in Figure 5.5. In spring, significant high positive correlation coefficients show up over part of the north central Russia, part of the northeastern Russia, and the Hudson and Baffin Bays; in summer, significant high positive correlation coefficients show up over part of the north central Russia, and the Chukchi Sea; in autumn, significant high positive correlation coefficients show up over regions between the northeastern Russia and the north central Russia. All these significant positive correlations are accompanied with significant positive trends in moisture convergence. These increasing moisture convergence might be closely related to the increasing cyclone activities in these three seasons in the past two decades, which is studied and demonstrated (Zhang et al. 2004; Serreze et al. 1997). The increasing cyclone activities in spring, summer, and autumn form more cloud in these seasons, which is demonstrated by the trends in the moisture convergence. The anomalies in Cyclone

Activity Index (CAI) (Zhang et al. 2004), which represents a combination of information about cyclone intensity, trajectory count, and duration, in the Arctic from 1950 to 2000 are shown in four seasons (Figure 5.6). In each season, there is significant increase in the CAI. From 1982 to 2000, the CAI shows negative anomalies in the 1980s, and positive anomalies in the 1990s, which indicates strengthened cyclone activity during this period in the Arctic. It needs to be pointed out that since 1990, the CAI drops significantly.

Trends in moisture convergence due to changing cyclone activities cannot explain the increasing cloud cover over Beaufort and Chukchi Seas in autumn, where there are not significant trends in moisture convergence or significant correlations between cloud anomalies and moisture convergence anomalies. As another important source of cloud formation in warm seasons, the surface evaporation might affect the cloud cover over the Beaufort and Chukchi Seas in autumn. Correlation coefficients between monthly anomalies in the APP-x cloud cover and ERA40 surface evaporation from 1982 to 2000 (Figure 5.7) show significant positive correlation coefficients over the Beaufort and Chukchi Seas. Over the same region, sea ice concentration decreases at the rate over –5.0%/decade from 1982 to 2000, which leads to more open water, an in turn more surface evaporation. Increasing cloud over this region might come from the increasing surface evaporation, which is converted to cloud by convection.

## 5.3 Summary

Decreased winter cloud cover over the Arctic Ocean from 1982 to 2000 is apparent both in the APP-x data set, TOVS retrievals, and in the ERA-40 reanalysis. This trend

cannot be attributed only to changing cyclonic activity in the Arctic, as the cyclone frequency overall has increased. Surface evaporation is small or negative over the Arctic Ocean in winter, thus it also cannot explain the observations.

Cloud cover anomalies over the Nansen Basin-Barents Sea-Kara Sea (NBK) region (75-90°N, 45-90°E) are closely related to moisture convergence anomalies. Over the NBK region, cyclone frequencies decreased during the same time period, which may be responsible for the decreased moisture convergence and cloud cover over this region. Cloud cover anomalies over the NBK region are closely related to cloud cover anomalies over the central Arctic Ocean, and anomalies over this region lead those over the regions to the east (regions numbers 2, 3, 4, 5 in Table 1). Decreased cloud over the NBK region appears to result in less cloud advected into the central Arctic Ocean, contributing to lower cloud amounts. Cloud phase also appears to have changed, such that ice cloud fractions increased over the central Arctic Ocean, which would decrease cloud cover owing to the quicker fall out of the ice particles. Less cloud cover is also observed in the E. Siberian Sea region, and could lead to the decreasing cloud cover over the Chukchi/Beaufort Seas and the Canada Basin.

In spring, summer, and autumn, the general increasing cloud cover can be attributed to the stronger cyclone activities. Over some regions, the increasing surface evaporation can be another factor affecting the cloud cover.

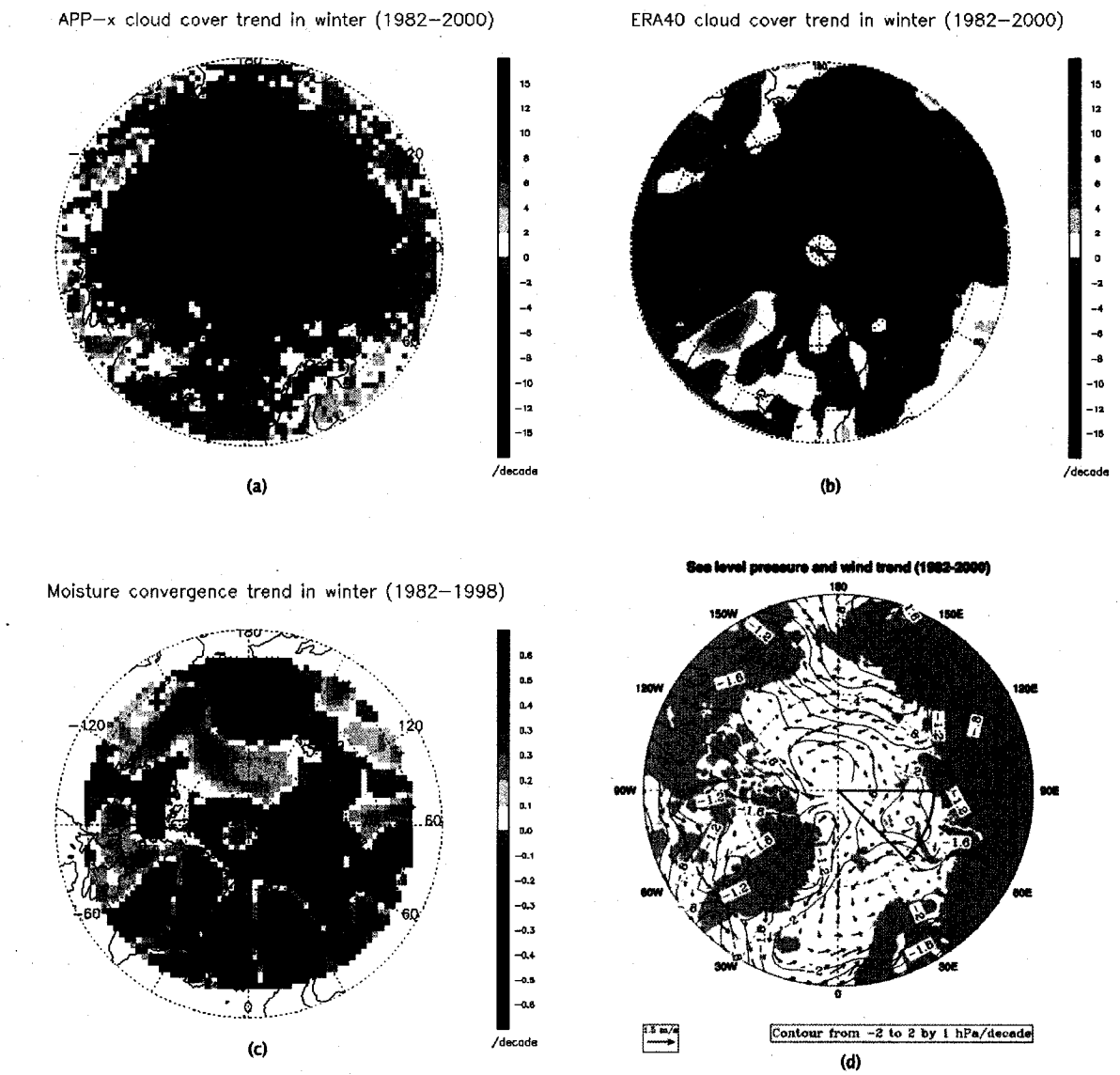


Fig 5.1. Decadal trends in (a) cloud clover from the APP-x (%/decade), (b) cloud cover from ERA40, (c) moisture convergence (cm/month) from TOVS Path-P, (d) sea level pressure (hPa) and wind (m/s) from ERA40, in the wintertime in the Arctic from 1982 to 2000. A trend with a confidence level larger than 95% based on the F-test is indicated with +.

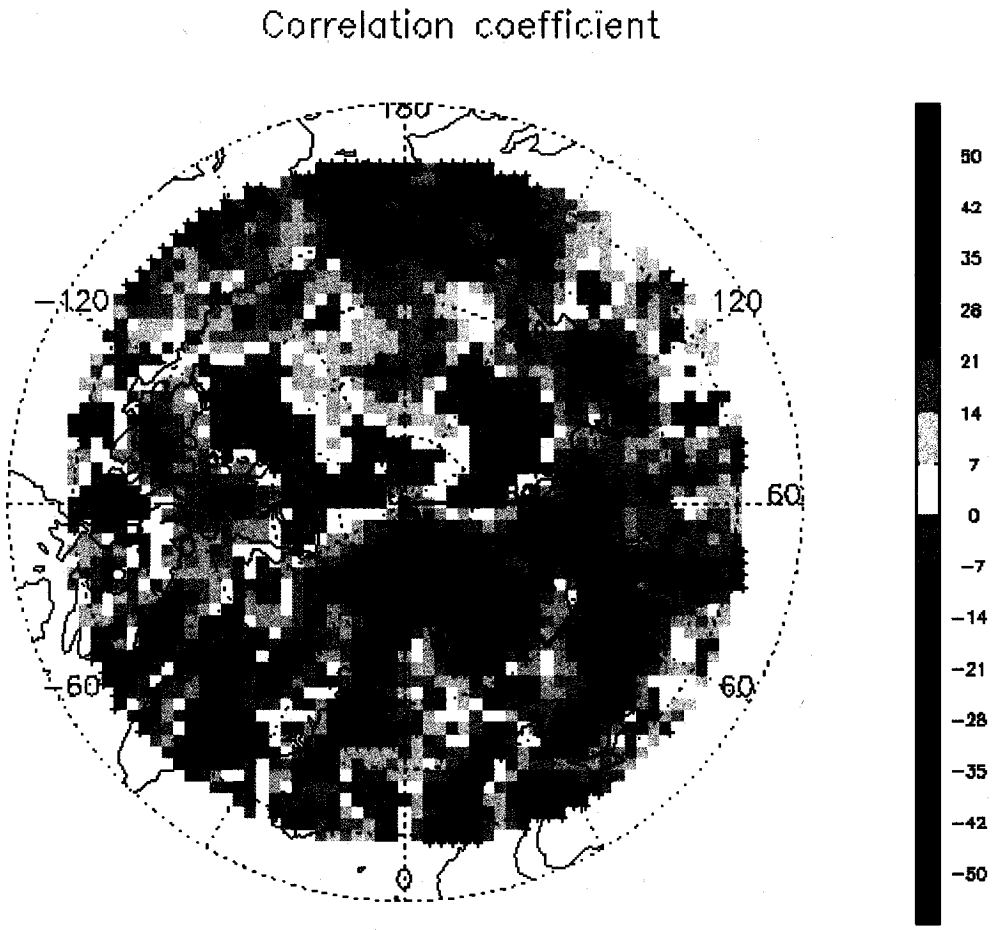


Fig. 5.2. Correlation (%) between the APP-x cloud cover monthly anomalies and the TOVS moisture convergence monthly anomalies in the cold season from 1982 to1998. A trend with confidence level larger than 95% based on student-t test is assigned with +.

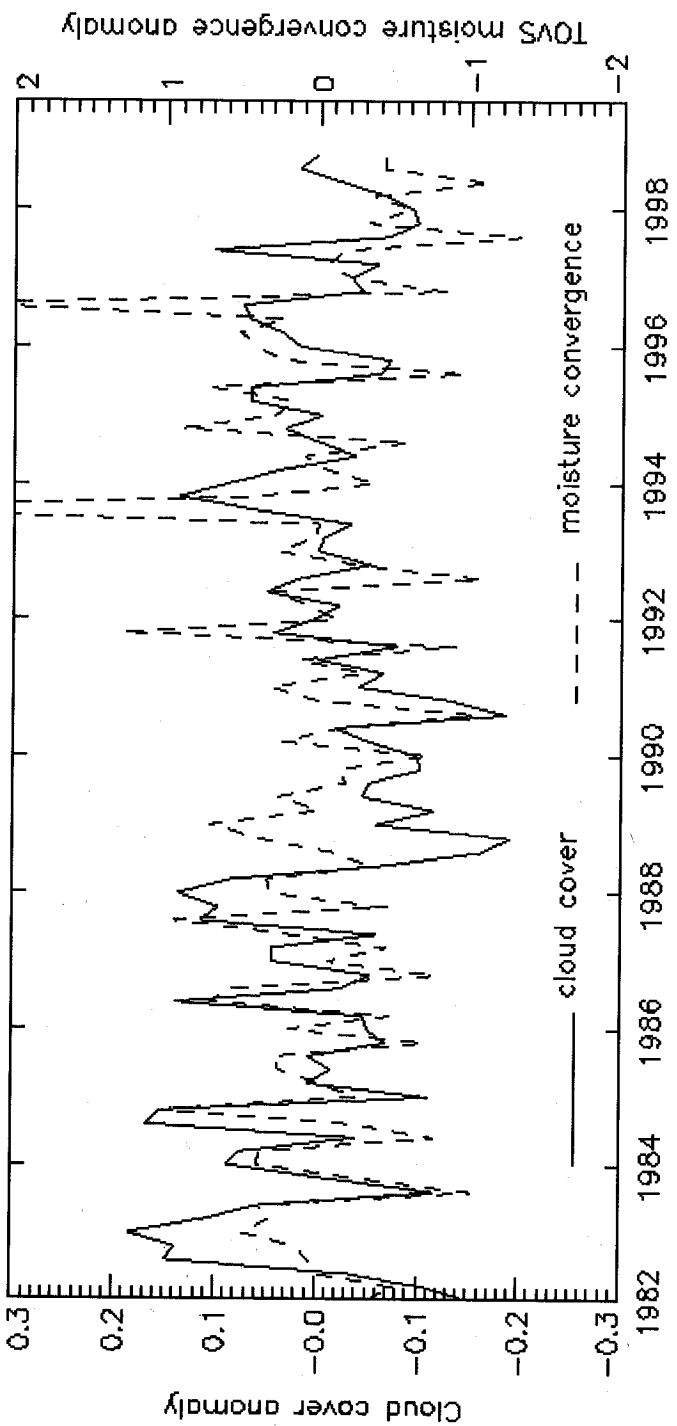


Fig. 5.3. Time series of APP-x cloud cover anomalies (range: [0,1]) and TOVS Path-P moisture convergence anomalies (cm/month) in the cold season from 1982 to 1998 averaged over the NBK region (75-90N; 45-90E).

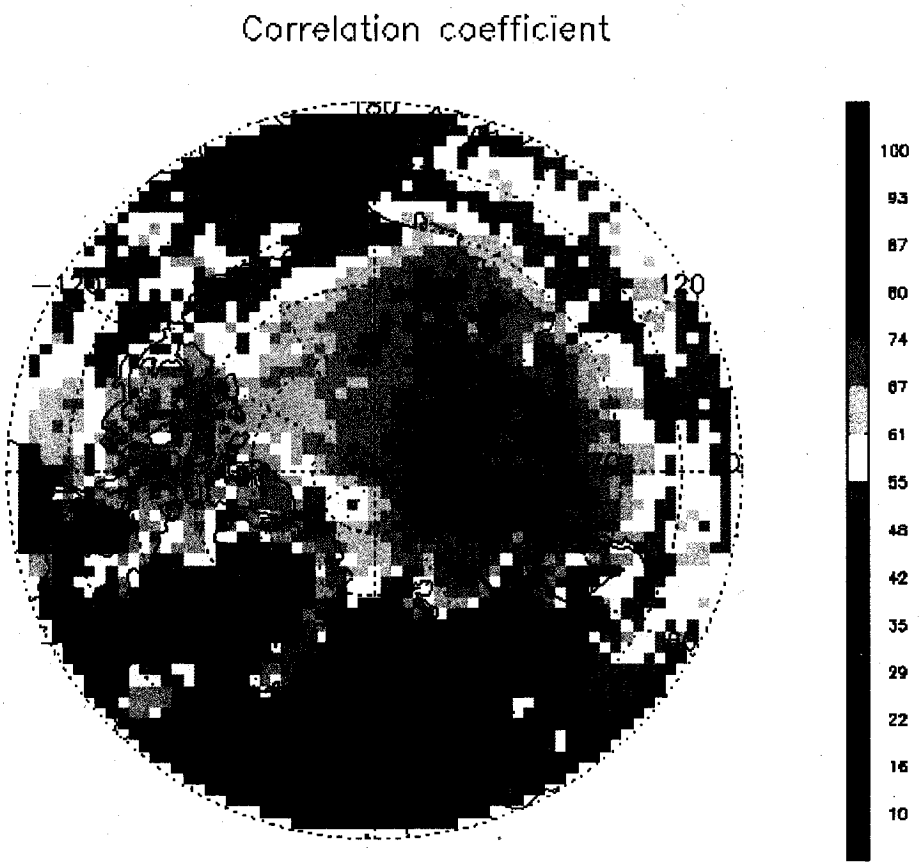


Fig. 5.4. Correlation between APP-x cloud cover monthly anomalies in each grid cell and those averaged over (75-90; 45-90) in the cold season from 1982 to 2000.

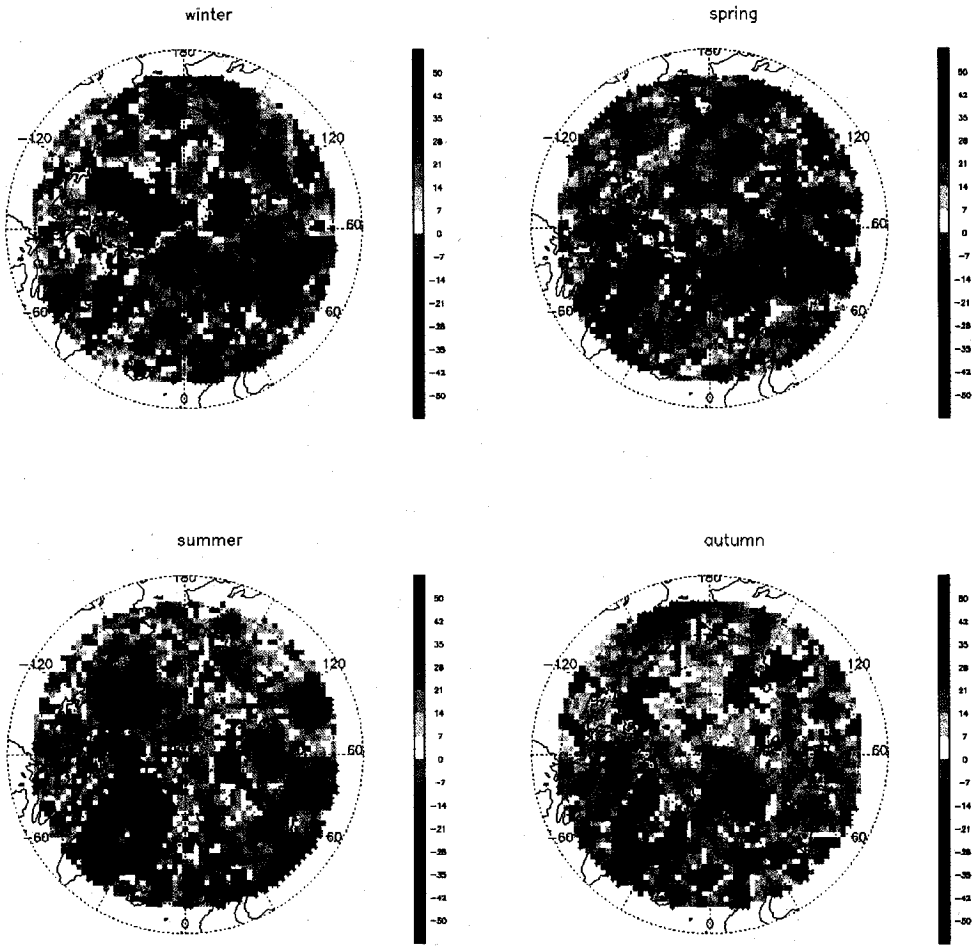


Fig. 5.5. Correlation coefficient between the APP-x cloud cover monthly anomalies and the TOVS Path-P moisture convergence monthly anomalies in winter, spring, summer, and autumn from 1982 t o1998. A trend with confidence level larger than 95% based on student-t test is assigned with +.

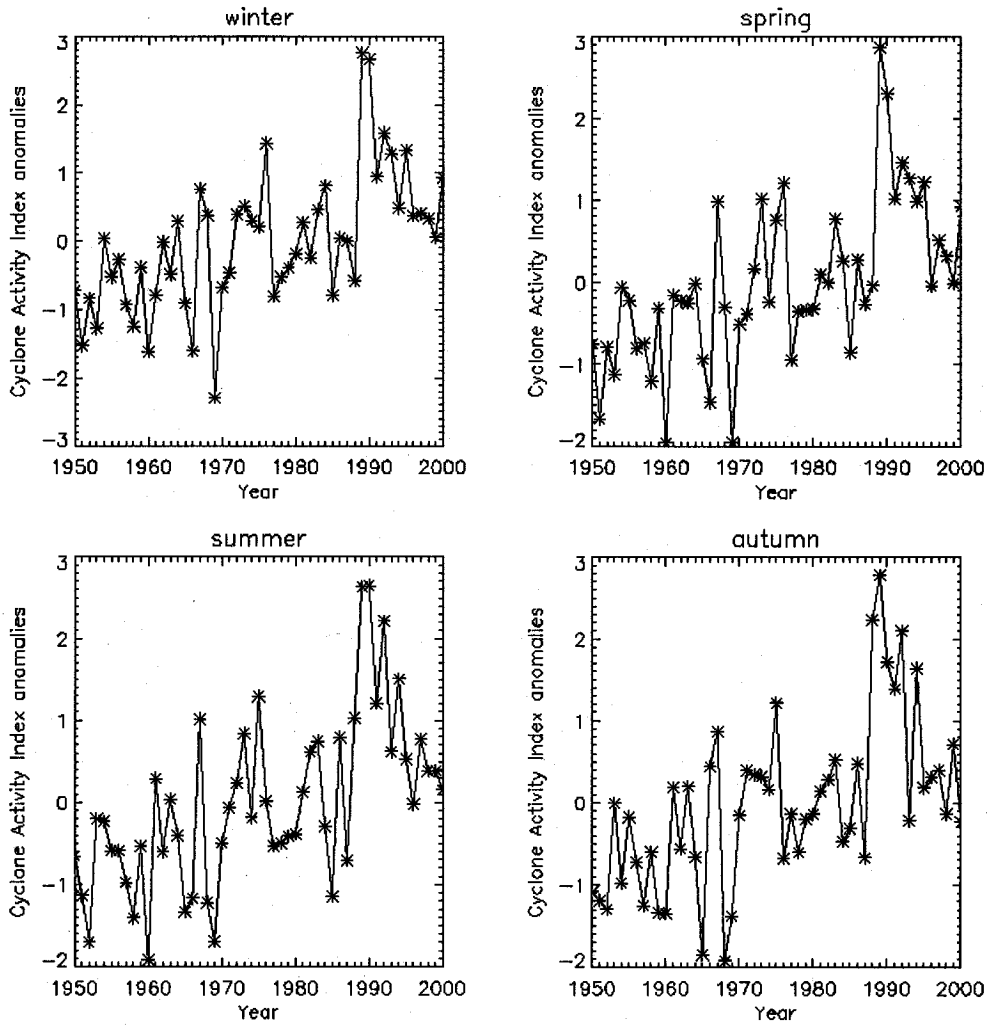


Fig. 5.6. Time series of Cyclone Activities Index anomalies in the Arctic in winter, spring, summer and autumn from 1950 to 2000.

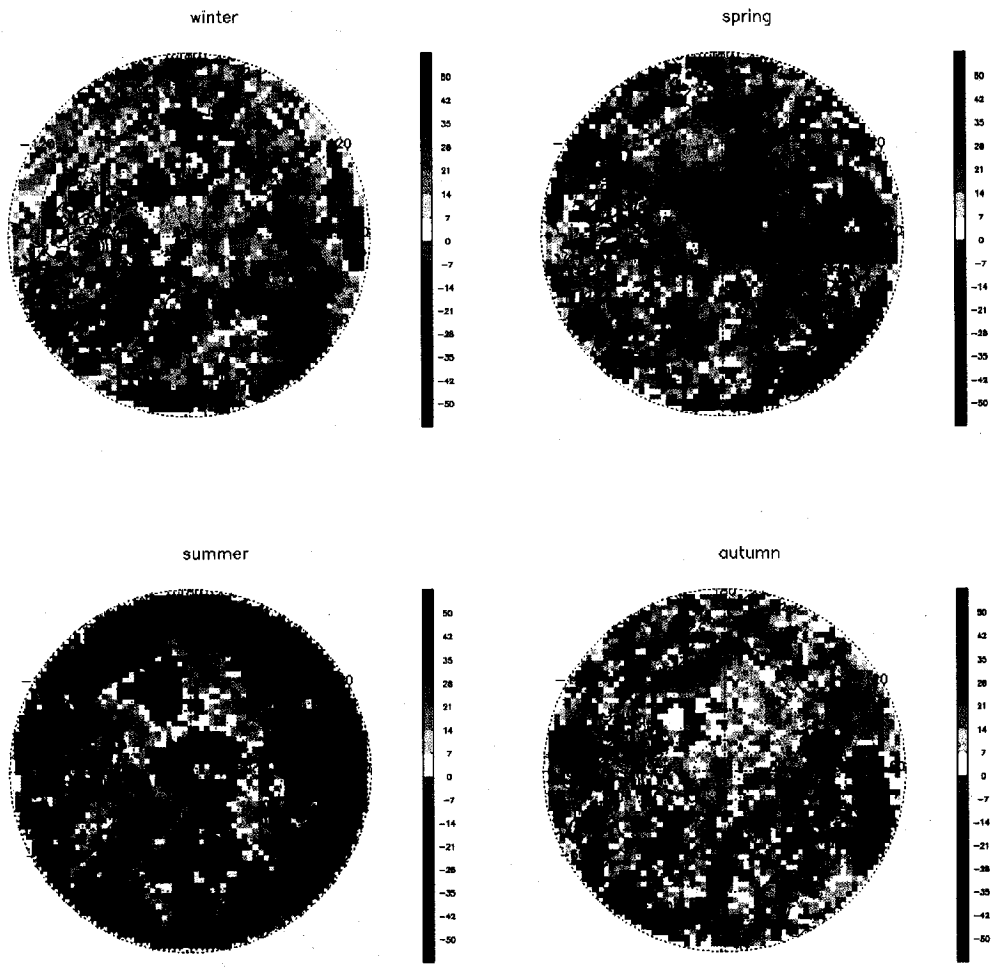


Fig. 5.7. Correlation coefficient between the APP-x cloud cover monthly anomalies and the ERA40 surface evaporation monthly anomalies in cold season from 1982 t o1998. A trend with confidence level larger than 95% based on student-t test is assigned with +.

Table 5.1. Correlation coefficients (CCs) of cloud cover anomalies among 5 regions over Arctic Ocean in winter in 1995. CCs with confidence level higher than 95% are underlined.

| CCs | Region 1 NBK (75-90°N) (45-90°E) | Region 2 Laptev (75-90°N) (90-135°E) | Region 3 E. Siberian (75-90°N) (135-180°E) | Region 4 Chukchi/Beaufort (75-90°N) (180-225°E) | Region 5 Canada Basin (75-90°N) (225-270°E) |
|---|---|---|---|---|---|
| 0_day lag | 1.00 | 0.48 | 0.15 | 0.17 | 0.23 |
| 1_day lag | 0.68 | 0.45 | 0.15 | 0.25 | 0.25 |
| 2_day lag | 0.45 | 0.39 | 0.25 | 0.29 | 0.14 |
| 3_day lag | 0.28 | 0.28 | 0.31 | 0.34 | 0.14 |
| 4_day lag | 0.17 | 0.16 | 0.29 | 0.36 | 0.22 |
| 5_day lag | 0.07 | -0.08 | 0.19 | 0.32 | 0.36 |
| 6_day lag | 0.04 | -0.13 | 0.16 | 0.27 | 0.30 |
| 7_day lag | 0.06 | -0.19 | 0.03 | 0.16 | 0.19 |

# 6 Conclusions and Future Plans

## 6.1 Summary and Conclusions

Significant changes in surface temperature, total cloud cover, lower tropospheric structure, heat and moisture convergence, and sea ice concentration in the Arctic in the past two decades are found based on satellite data and a reanalysis product. For different areas and seasons in the Arctic, these changes are different.

Significant cooling of all-sky surface temperature is found over the Arctic Ocean in winter from 1982-2000 based on the APP-x dataset, with the cooling trend around -2.5 K/decade over the central Arctic Ocean. A similar trend is also seen in the ERA40 reanalysis. This cooling winter all-sky surface temperature is consistent with the decreasing winter cloud cover over the Arctic Ocean, derived from both APP-x and ERA40, because clouds over the Arctic Ocean in winter warm the surface. In spring and summer, the all-sky surface temperature in the Arctic is generally warming. Surface temperature trends under cloud-free and cloudy conditions are spatially similar to the all-sky trends. However, the absolute magnitude of the trend under cloud-free conditions is larger than that under cloudy conditions, which demonstrates the negative feedback of clouds on the surface temperature.

Winter cloud cover decreased significantly over the Arctic Ocean from 1982-2000, with the maximum trend around –15%/decade. In spring and summer, the general trend in cloud cover increased. In autumn, there are no apparent trends over the Arctic.

Moisture convergence has positive trends over the Canada Basin and the eastern GIN Sea areas; negative trends over portions of the Nansen Basin, the Barents and Kara Seas; and around the Bering Strait in winter from 1982-1998. In spring, positive trends of moisture convergence are found over the Beaufort and Chukchi Seas, north central Russia, and part of North Canada, which corresponds to the positive trends in cloud cover over these regions. Heat convergence showed positive trends over portions of the Chukchi Sea, Alaska region, and northern Europe; and negative trends over regions surrounding the Nansen Basin, north central Russia and around the Bering Strait in winter from 1982-2000.

In winter, the sea ice concentration increased over most of the Arctic Ocean from 1982-2000, with the maximum trend around 3.0%/decade. Meanwhile, decreasing sea ice concentration trends are seen over Hudson and Baffin Bays, and around the sea ice edge in the Barents and Kara Seas. Sea ice concentration changes in spring shows similar patterns as those in winter. In summer and autumn, the sea ice concentration decreases over most of the Arctic Ocean, with a maximum negative trend of more than –5.0%/decade.

Clear-sky temperature inversion strength, one important parameter of the lower troposphere atmospheric structure, is derived from satellite data from 1980-1996 using a 2-channel statistical algorithm based on the different absorbing characteristics in the window channel and water vapor channel. In the cold season, the clear-sky temperature inversion is weak over the Greenland and Norwegian Seas, the Barents Sea, and northern Europe, which is attributable to turbulent mixing over open water and high cloud cover in

this region during the winter. Inversion strength increases eastward, followed by a decrease over Alaska. Stronger inversion can be seen over northern Russia, northern Canada, and the pack ice, with the largest values near several Russian river valleys due to strong radiative cooling under clear conditions. From 1980-1996, the clear-sky inversion strength in the cold season decreased over the East Siberian and Chukchi Seas, and increased over the north central Russia in winter, which reflects the atmospheric structure changes in the Arctic in winter.

There is strong coupling between changes in surface temperature and temperature inversion strength. Correlation coefficients between the monthly mean surface skin temperature anomalies and monthly mean 2-channel inversion strength anomalies from November to March over the period from 1980-1996 show negative correlation coefficients less than -0.6 over northern Europe, north central Russia, Alaska and part of northeastern Russia, which means the inversion strength trend over these regions is closely related to the surface skin temperature trend. However, correlation coefficients are near zero from the Canadian Archipelago across the central Arctic Ocean and through the East Siberian Sea into Siberia. Correlation coefficients between anomalies in the inversion strength and the AO index are negative over northern Europe, north central Russia and the East Siberian Sea, and positive over the Canadian Archipelago. Over the East Siberian Sea, the correlation coefficients between the AO and surface temperature are near zero or negative, but the correlation coefficients between the AO and inversion strength are significantly negative. It is possible that in these areas the trend in inversion

strength may be more a function of changes in heat advection into or out of the Arctic than changes in surface temperature.

The significant changes in surface temperature, total cloud cover, inversion strength, heat and moisture convergence, and sea ice concentration cannot be completely explained by the changes in the large-scale atmospheric circulation, Arctic Oscillation (AO) changes. Understanding the complicated feedback mechanisms behind these changes is very important for understanding Arctic climate changes over the past few decades, and for predicting and forecasting future climate changes.

The feedback mechanisms behind these significant changes, and the interactions between these changes in the Arctic, are complicated. For different areas, in different seasons in the Arctic, these feedback mechanisms and interactions are different.

Changes in cloud cover influence surface temperature changes observed from satellites. The influence of the cloud cover changes in the total surface temperature changes in four seasons in the Arctic is shown based on the seasonal means and trends in surface temperature and cloud cover. The surface temperature trend is partitioned into two parts: the first part (trend A) is the linear combination of the surface temperature trends under cloud-free and cloudy conditions; the second part (trend B) is caused by the trend in cloud cover and the surface temperature difference under cloudy and clear-sky conditions. Trend B is significant in winter and spring over the Arctic Ocean because of the significant cloud cover changes and cloudy/clear surface temperature differences. In winter, more than half of the decreasing surface temperature trend is from trend B over the central Arctic. In spring, trend A contributes more than trend B to the total trend over

land and over the Chukchi and Beaufort Seas. In the autumn and summer, trend A dominates, because cloud cover trends are small and/or the clear/cloudy sky temperature difference is small. The trend caused by a bias in the satellite retrieval of surface temperature is a part of trend B, and it accounts for 1/4, 1/4, 2/3, and 1/3 of trend B in winter, spring, summer and autumn respectively, given a retrieval bias difference of 2 K between cloudy and clear-sky conditions.

For different areas and seasons, the mechanisms behind the total cloud cover changes are different. Correlation coefficients between the monthly anomalies in the APP-x cloud cover and the TOVS Path-P moisture convergence are significant over region (75-90 °N, 45-90 °E), where decreasing cloud cover and moisture convergence are seen from 1982-1998. During the same time period, weaker cyclonic activity is also possible over this region, which would result in fewer clouds. As the most important source of cloud formation over the Arctic Ocean in winter, the decreasing moisture convergence might be the result of less cloud formation due to weaker cyclone activity. Correlation coefficient analysis also shows that cloud cover anomalies over this region are closely related to, and affect, the cloud cover anomalies over other regions in the Arctic Ocean to the east. It is reasonable to believe that less cloud cover over this special region leads to less cloud cover over other regions in the Arctic Ocean in the way that less cloud is advected into other regions. On the other hand, increasing cloud cover in spring and summer is closely related to increasing moisture convergence due to increasing cyclonic activity; and increasing surface evaporation due to decreasing sea ice concentration may also contribute to the increasing cloud cover.

## 6.2 Remaining Issues and Future Plans

This study shows the dramatic changes in the surface, atmosphere, and cloud cover in the Arctic over the past two decades, and investigates their connections to changes in large-scale circulation. An explanation of cloud cover changes in the Arctic in four seasons is proposed and tested. The influence of cloud cover changes in the total surface temperature changes is quantified. By doing so, this study improves our understanding of the complicated Arctic atmosphere-ocean system.

At the same time, this study raises more questions; indicates some new research directions and calls for more work to be done.

Different meteorological parameters vary simultaneously and interact with each other in the complicated Arctic climate system. It is very challenging to investigate the mechanisms behind the different changes among cloud, surface, and atmosphere. The statistical analysis based on long-term high temporal and spatial resolution data is shown by this study to be helpful. Another powerful tool is the simulation using regional and global models, which enable us to study the effect of an individual parameter in a complicated system, and to predict the future changes in theory. However, current theoretical models do not perform as well as we expect in polar regions; various feedback mechanisms in the Arctic are still not well understood in theory. More observations are needed to explore these feedbacks in order to improve the theoretical simulations.

Combinations of these two tools, statistical analysis based on real data and model simulations, will improve our understanding more in the future.

A hypothesis explaining the cloud cover changes in four seasons in the Arctic is proposed and tested based on observations in this study. Simulations using regional and even global climate models are needed to further test this hypothesis. More sophisticated statistical tools, and longer high quality observational data are also needed.

Changes in moisture convergence and surface evaporation might compete to affect cloud formation. Less sea ice concentration and less sea ice cover will lead to more open water, which leads to stronger surface evaporation. Does the stronger surface evaporation affect moisture convergence locally? If so, how? This issue requires further investigation.

Understanding the surface temperature trends in four seasons in the Arctic is extremely important for understanding the Arctic climate system, since surface temperature integrates changes in the surface energy budget and atmospheric circulation. The ability to predict and forecast the future changes in the surface temperature is critical to the future of humanity. In this work, though the influence of cloud cover on surface temperature changes is investigated, we are far from completely understanding the mechanisms behind the surface temperature trend under clear and cloudy conditions, which requires knowledge of the surface and atmospheric energy budgets. In the APP-x dataset, downward longwave and short-wave radiation at surface are available, while other parameters including latent heat flux, sensible heat flux, and parameters related to oceanic process are available from reanalysis datasets. These provide the opportunity to study the mechanisms of surface temperature changes.

## 7 References

Andreas, E. L., 1980: Estimation of Heat and Mass Fluxes Over Arctic Leads. Mon. Weather Rev., 108, 2057-2063.

Andreas, E. L., and B. Murphy, 1986: Bulk Transfer-Coefficients for Heat and Momentum Over Leads and Polynyas. J. Phys. Oceanogr., 16, 1875-1883.

Barrie, L. A., J. W. Bottenheim, R. C. Schnell, P. J. Crutzen, and R. A. Rasmussen, 1988: Ozone Destruction and Photochemical-Reactions at Polar Sunrise in the Lower Arctic Atmosphere. Nature, 334, 138-141.

Barry, R. G., and M. W. Miles, 1988: Lead patterns in Arctic sea ice from remote sensing data: characteristics, controls and atmospheric interactions. Extended Abstracts Volume, Second Conference on Polar Meteorology and Oceanography, American Meteorological Society. March 29-31, 1988, Madison, Wisconsin, U.S.A.

Beesley, J. A., and R. E. Moritz, 1999: Toward an explanation of the annual cycle of cloudiness over the Arctic ocean. J. Clim., 12, 395-415.

Bilello, M.A., 1966:Survery of Arctic and Subarctic temperature inversions, Tech. Rep. 161, Cold Regions Res and Eng. Lab..

Bradley, R. S., and F. T. Keimig, 1993: Recent Changes in the North-American Arctic Boundary-Layer in Winter. *Journal of Geophysical Research-Atmospheres,* **98**, 8851-8858.

Bradley, R. S., F. T. Keimig, and H. F. Diaz, 1992: Climatology of Surface-Based Inversions in the North-American Arctic. Journal of Geophysical Research-Atmospheres, 97, 15699-15712.

Bradley, R. S., F. T. Keimig, and H. F. Diaz, 1996: Recent changes in the North American Arctic boundary layer in winter - Reply. Journal of Geophysical Research-Atmospheres, 101, 7135-7136.

Bridgman, H. A., R. C. Schnell, J. D. Kahl, G. A. Herbert, and E. Joranger, 1989: A Major Haze Event Near Point Barrow, Alaska - Analysis of Probable Source Regions and Transport Pathways. Atmos. Environ., 23, 2537-2549.

Busch, N., U. Ebel, H. Kraus, and E. Schaller, 1982: The structure of the subpolar inversion-capped ABL. Arch. Met. Geophys. Bioklim., 31A, 1-18.

Cavalieri, D., C. Parkinson, P. Gloerson, and H.J. Zwally. 1996, updated 2005: Sea ice concentrations from Nimbus-7 SMMR and DMSP SSM/I passive microwave data, 1982 to 2001. Boulder, CO, USA: National Snow and Ice Data Center. Digital media.

Cavalieri, D. J., P. Gloersen, C. L. Parkinson, J. C. Comiso, and H. J. Zwally, 1997: Observed hemispheric asymmetry in global sea ice changes. Science, 278, 1104-1106.

Chapman, W. L., and J. E. Walsh, 1993: Recent Variations of Sea Ice and Air-Temperature in High-Latitudes. Bull. Am. Meteorol. Soc., 74, 33-47.

Chedin, A., N. A. Scott, C. Wahiche, and P. Moulinier, 1985: The improved initialization inversion method: A high resolution physical method for temperature retrievals from satellites of the TIROS-N series. J. Clim. Appl. Meteorol., 24., 128-143.

Chen, Y. H., J. A. Francis, and J. R. Miller, 2002: Surface temperature of the Arctic: Comparison of TOVS satellite retrievals with surface observations. J. Clim., 15, 3698-3708.

Comiso, J. C., 2003: Warming trends in the Arctic from clear sky satellite observations. J. Clim., 16, 3498-3510.

Comiso, J. C., 2001: Satellite-observed variability and trend in sea-ice extent, surface temperature, albedo and clouds in the Arctic. Annals of Glaciology, Vol 33, 33, 457-473.

Curry, J., 1983: On the Formation of Continental Polar Air. J. Atmos. Sci., 40, 2278-2292.

Curry, J. A., W. B. Rossow, D. Randall, and J. L. Schramm, 1996: Overview of Arctic cloud and radiation characteristics. J. Clim., 9, 1731-1764.

Curry, J. A., J. L. Schramm, and E. E. Ebert, 1993: Impact of Clouds on the Surface Radiation Balance of the Arctic-Ocean. Meteorology and Atmospheric Physics, 51, 197-217.

Dai, A. G., T. R. Karl, B. M. Sun, and K. E. Trenberth, 2006: Recent trends in cloudiness over the United States - A tale of monitoring inadequacies. Bull. Am. Meteorol. Soc., 87, 597-606.

Fowler, C., J. Maslanik, T. Haran, T. Scambos, J. Key, and W. Emery 2000: AVHRR Polar Pathfinder twice-daily 5 km EASE-grid composites. National Snow and Ice Data Center, Boulder, CO. [Available online at nsidc.org/data/docs/daac/nsidc0066_avhrr_5km.gd.html.].

Francis, J. A., 1994: Improvements to Tovs Retrievals Over Sea-Ice and Applications to Estimating Arctic Energy Fluxes. Journal of Geophysical Research-Atmospheres, 99, 10395-10408.

Groisman, P. Y., T. R. Karl, and R. W. Knight, 1994: Observed Impact of Snow Cover on the Heat-Balance and the Rise of Continental Spring Temperatures. Science, 263, 198-200.

Groves, D. G., and J. A. Francis, 2002a: Moisture budget of the Arctic atmosphere from TOVS satellite data. Journal of Geophysical Research-Atmospheres, 107, 4391.

Groves, D. G., and J. A. Francis, 2002b: Variability of the Arctic atmospheric moisture budget from TOVS satellite data. Journal of Geophysical Research-Atmospheres, 107, 4785.

Houghton J. T., and et al. IPCC Third Assessment Report, Climate Change 2001: The science of climate change, Inter-governmental Panel on Climate Change, J. T. Houghton et al., eds., Cambridge U. Press.

Herman, G., and R. Goody, 1976: Formation and Persistence of Summertime Arctic Stratus Clouds. J. Atmos. Sci., 33, 1537-1553.

Hibler, W. D., and K. Bryan, 1987: A Diagnostic Ice Ocean Model. J. Phys. Oceanogr., 17, 987-1015.

Intrieri, J. M., C. W. Fairall, M. D. Shupe, P. O. G. Persson, E. L. Andreas, P. S. Guest, and R. E. Moritz, 2002: An annual cycle of Arctic surface cloud forcing at SHEBA. Journal of Geophysical Research-Oceans, 107, 8039.

Jones, P. D., 1994: Hemispheric Surface Air-Temperature Variations - a Reanalysis and an Update to 1993. J. Clim., 7, 1794-1802.

Jones, P. D., T. J. Osborn, K. R. Briffa, C. K. Folland, E. B. Horton, L. V. Alexander, D. E. Parker, and N. A. Rayner, 2001: Adjusting for sampling density in grid box land and ocean surface temperature time series. Journal of Geophysical Research-Atmospheres, 106, 3371-3380.

Kahl, J. D., 1990: Characteristics of the Low-Level Temperature Inversion Along the Alaskan Arctic Coast. Int. J. Climatol., 10, 537-548.

Kahl, J. D., M. C. Serreze, and R. C. Schnell, 1992a: Tropospheric Low-Level Temperature Inversions in the Canadian Arctic. Atmosphere-Ocean, 30, 511-529.

Kahl, J. D., M. C. Serreze, S. Shiotani, S. M. Skony, and R. C. Schnell, 1992b: Insitu Meteorological Sounding Archives for Arctic Studies. Bull. Am. Meteorol. Soc., 73, 1824-1830.

Kahl, J. D., D. A. Martinez, 1996: Long-term variability in the low-level inversion layer over the Arctic Ocean. Int. J. Climatol., 16, 1297-1313.

Key, J.R. 2002: The cloud and surface parameter retrieval (CASPR) system for polar AVHRR, Cooperative Institute for Meteorological Satellite Studies, University of Wisconsin-Madison, 59 pp. [Available online at stratus.ssec.wisc.edu/caspr/documentation.html.].

Key, J., and R. G. Barry, 1989: Cloud Cover Analysis with Arctic Avhrr Data .1. Cloud Detection. Journal of Geophysical Research-Atmospheres, 94, 18521-18535.

Key, J., and M. Haefliger, 1992: Arctic Ice Surface-Temperature Retrieval from Avhrr Thermal Channels. Journal of Geophysical Research-Atmospheres, 97, 5885-5893.

Key, J. R., and A. C. K. Chan, 1999: Multidecadal global and regional trends in 1000 mb and 500 mb cyclone frequencies. Geophys. Res. Lett., 26, 2053-2056.

Key, J., and A. J. Schweiger, 1998: Tools for atmospheric radiative transfer: Streamer and FluxNet. Comput. Geosci., 24, 443-451.

Key, J. R., J. B. Collins, C. Fowler, and R. S. Stone, 1997: High-latitude surface temperature estimates from thermal satellite data. Remote Sens. Environ., 61, 302-309.

Key, J. R., and J. M. Intrieri, 2000: Cloud particle phase determination with the AVHRR. J. Appl. Meteorol., 39, 1797-1804.

Key, J. and A.M. Wong 1999: Estimating the cloudy sky surface temperature of sea ice with optical satellite data, IGARSS'99 Proceedings, Hamburg, Germany, 28 June - 2 July.

Key, J. R., X. J. Wang, J. C. Stoeve, and C. Fowler, 2001: Estimating the cloudy-sky albedo of sea ice and snow from space. Journal of Geophysical Research-Atmospheres, 106, 12489-12497.

Kidwell K. B., 1998: NOAA Polar Orbiter data user\u2019s guide (TIROS-N through NOAA-14). NOAA/NESDIS, Satellite Services Branch. [Available online at http://www2.ncdc.noaa.gov/docs/podug.].

King, M. D. and Coauthors, 2003: Cloud and aerosol properties, precipitable water, and profiles of temperature and water vapor from MODIS. IEEE Trans. Geosci. Remote Sens., 41, 442-458.

Liu, Y. H., and J. R. Key, 2003: Detection and analysis of clear-sky, low-level atmospheric temperature inversions with MODIS. J. Atmos. Ocean. Technol., 20, 1727-1737.

Mahesh, A., V. P. Walden, and S. G. Warren, 1997: Radiosonde temperature measurements in strong inversions: Correction for thermal lag based on an experiment at the South Pole. J. Atmos. Ocean. Technol., 14, 45-53.

Manabe, S., M. J. Spelman, and R. J. Stouffer, 1992: Transient Responses of a Coupled Ocean Atmosphere Model to Gradual Changes of Atmospheric Co2 .2. Seasonal Response. J. Clim., 5, 105-126.

Maslanik, J. A., M. C. Serreze, and R. G. Barry, 1996: Recent decreases in Arctic summer ice cover and linkages to atmospheric circulation anomalies. *Geophys. Res. Lett.*, **23**, 1677-1680.

Maslanik, J. A., J. Key, C. W. Fowler, T. Nguyen, and X. Wang, 2001: Spatial and temporal variability of satellite-derived cloud and surface characteristics during FIRE-ACE. Journal of Geophysical Research-Atmospheres, 106, 15233-15249.

Maykut, G. A., and P.E. Church, 1973: Radiation climate of Barrow, Alaska, 1962-66. J. Appl. Meteor., 12, 620-628.

Maxwell, J.B., 1982: The climated of the Canadian Arctic islands and adjacent waters, vol. 2, 589 pp., Atmospheric environment services, Downsview, Ontario, Canada.

McCabe, G. J., M. P. Clark, and M. C. Serreze, 2001: Trends in Northern Hemisphere surface cyclone frequency and intensity. J. Clim., 14, 2763-2768.

McPhee, M. G., T. P. Stanton, J. H. Morison, and D. G. Martinson, 1998: Freshening of the upper ocean in the Arctic: Is perennial sea ice disappearing? Geophys. Res. Lett., 25, 1729-1732.

Meier, W., J.A. Maslanik, J.R. Key, and C.W. Fowler 1997: Multiparameter AVHRR-derived products for Arctic climate studies, Earth Interactions, 1. [Available online at EarthInteractions.org.].

Overland, J. E., 1985: Atmospheric Boundary-Layer Structure and Drag Coefficients Over Sea Ice. Journal of Geophysical Research-Oceans, 90, 9029-9049.

Parkinson, C. L., D. J. Cavalieri, P. Gloersen, H. J. Zwally, and J. C. Comiso, 1999: Arctic sea ice extents, areas, and trends, 1978-1996. Journal of Geophysical Research-Oceans, 104, 20837-20856.

Qian, Y., D. P. Kaiser, L. R. Leung, and M. Xu, 2006: More frequent cloud-free sky and less surface solar radiation in China from 1955 to 2000. Geophys. Res. Lett., 33, L01812.

Randall, D. and Coauthors, , 1998: Status of and outlook for large-scale modeling of atmosphere-ice-ocean interactions in the Arctic. Bull. Am. Meteorol. Soc., 79, 197-219.

Rigor, I. G., R. L. Colony, and S. Martin, 2000: Variations in surface air temperature observations in the Arctic, 1979-97. J. Clim., 13, 896-914.

Schweiger, A. J., 2004: Changes in seasonal cloud cover over the Arctic seas from satellite and surface observations. Geophys. Res. Lett., 31, L12207.

Schweiger, A. J., and J. R. Key, 1994: Arctic-Ocean Radiative Fluxes and Cloud Forcing Estimated from the Isccp C2 Cloud Dataset, 1983-1990. J. Appl. Meteorol., 33, 948-963.

Schweiger, A., R. Lindsay, J. Francis, J. Key, J. Intrieri, and M. Shupe, 2002: Validation of TOVS Path-P data during SHEBA. J. Geophys. Res., 8041, doi:10.1029/2000JC000453.

Serreze, M. C., and R. G. Barry, 1988: Synoptic activity in the Arctic Basin, 1975-85. J. Clim., 1, 1276-1295.

Serreze, M. C., F. Carse, R. G. Barry, and J. C. Rogers, 1997: Icelandic low cyclone activity: Climatological features, linkages with the NAG, and relationships with recent changes in the Northern Hemisphere circulation. J. Clim., 10, 453-464.

Serreze, M. C., J. D. Kahl, and R. C. Schnell, 1992: Low-Level Temperature Inversions of the Eurasian Arctic and Comparisons with Soviet Drifting Station Data. J. Clim., 5, 615-629.

Serreze, M. C. and Coauthors, 2000: Observational evidence of recent change in the northern high-latitude environment. Clim. Change, 46, 159-207.

Serreze, M. C., F. Carse, R. G. Barry and J. C. Rogers, 1997: Icelandic low cyclone activity: Climatological features, linkages with the NAG, and relationships with recent changes in the Northern Hemisphere circulation. J.Clim., 10, 453-464.

Stone, R. S., and J. D. Kahl, 1991: Variations in Boundary-Layer Properties Associated with Clouds and Transient Weather Disturbances at the South-Pole during Winter. Journal of Geophysical Research-Atmospheres, 96, 5137-5144.

Stroeve, J. C., J. E. Box, C. Fowler, T. Haran, and J. Key, 2001: Intercomparison between in situ and AVHRR polar pathfinder-derived surface Albedo over Greenland. Remote Sens. Environ., 75, 360-374.

Stubenrauch, C. J., A. Chedin, R. Armante, and N. A. Scott, 1999: Clouds as seen by satellite sounders (3I) and imagers (ISCCP). Part II: A new approach for cloud parameter determination in the 3I algorithms. J. Clim., 12, 2214-2223.

Thompson, D. W. J., and J. M. Wallace, 2000: Annular modes in the extratropical circulation. Part I: Month-to-month variability. *J. Clim.,* **13**, 1000-1016.

Thompson, D. W. J., and J. M. Wallace, 1998: The Arctic Oscillation signature in the wintertime geopotential height and temperature fields. *Geophys. Res. Lett.,* **25**, 1297-1300.

Thompson, D. W. J., J. M. Wallace, and G. C. Hegerl, 2000: Annular modes in the extratropical circulation. Part II: Trends. *J. Clim.,* **13**, 1018-1036.

Uppala, S. M. and Coauthors, , 2005: The ERA-40 re-analysis. Q. J. R. Meteorol. Soc., 131, 2961-3012.

Vavrus, S., 2004: The impact of cloud feedbacks on Arctic climate under greenhouse forcing. *J. Clim.,* **17**, 603-615.

Vowinkel, E., and S. Orvig, 1970: The climate of the North Polar Basin. World Survey of Climatology, Vol. 14: Climates of the Polar Regions, S. Orvig, Ed., Elsevier, 129-226.

Walden, V. P., A. Mahesh, and S. G. Warren, 1996: Recent changes in the North American Arctic boundary layer in winter - Comment. Journal of Geophysical Research-Atmospheres, 101, 7127-7134.

Walsh, J. E., and W. L. Chapman, 1998: Arctic cloud-radiation-temperature associations in observational data and atmospheric reanalyses. J. Clim., 11, 3030-3045.

Walsh, J. E., W. L. Chapman, and T. L. Shy, 1996: Recent decrease of sea level pressure in the central Arctic. *J. Clim.,* **9**, 480-486.

Wang, X. J., and J. R. Key, 2005: Arctic surface, cloud, and radiation properties based on the AVHRR Polar Pathfinder dataset. Part I: Spatial and temporal characteristics. J. Clim., 18, 2558-2574.

Wang, X. J., and J. R. Key, 2005: Arctic surface, cloud, and radiation properties based on the AVHRR Polar Pathfinder dataset. Part II: Recent trends. J. Clim., 18, 2575-2593.

Wang, X. J., and J. R. Key, 2003: Recent trends in arctic surface, cloud, and radiation properties from space. Science, 299, 1725-1728.

Zhang, X. D., J. E. Walsh, J. Zhang, U. S. Bhatt, and M. Ikeda, 2004: Climatology and interannual variability of arctic cyclone activity: 1948-2002. J. Clim., 17, 2300-2317.